NATIONAL AERONAUTICS AND SPACE ADMINISTRATION

Technical Memorandum 33-621

Impinging Jet Separators for Liquid Metal Magnetohydrodynamic Power Cycles

David W. Bogdanoff

JET PROPULSION LABORATORY
CALIFORNIA INSTITUTE OF TECHNOLOGY
PASADENA, CALIFORNIA

December 1, 1973

NATIONAL AERONAUTICS AND SPACE ADMINISTRATION

Technical Memorandum 33-621

Impinging Jet Separators for Liquid Metal Magnetohydrodynamic Power Cycles

David W. Bogdanoff

JET PROPULSION LABORATORY
CALIFORNIA INSTITUTE OF TECHNOLOGY
PASADENA, CALIFORNIA

December 1, 1973

I

Prepared Under Contract No. NAS 7-100
National Aeronautics and Space Administration

PREFACE

The work described in this report was performed by the Propulsion Division of the Jet Propulsion Laboratory.

ACKNOWLEDGMENT

A substantial part of the financial support for the project was provided by the National Research Council. The author worked at the Jet Propulsion Laboratory for two years as a National Research Council Resident Research Associate. A great deal of support and technical advice was given to the author by David G. Elliott, and Lance G. Hays. Donald J. Cerini, Cecil Dilts, Charles Dame and Paul S. Zygielbaum assisted in the operation of the test apparatus.

CONTENTS

CONTENTS (contd)

CONTENTS (contd)

FIGURES

FIGURES (contd)

FIGURES (contd)

FIGURES (contd)

ABSTRACT

In many liquid metal MHD power cycles, it is necessary to separate the phases of a high-speed liquid-gas (or liquid-vapor) flow. The usual method is to impinge the jet at a glancing angle against a solid surface (which may be straight or curved). These surface separators achieve good separation of the two phases at a cost of a large velocity loss due to friction at the separator surface. This report deals with attempts to greatly reduce the friction loss by impinging two (or more) jets against each other. In the crude impinging-jet separators tested to date (April 15, 1972), friction losses were, in fact, found to be greatly reduced, but the separation of the two phases was found to be much poorer than that achievable with surface separators. The separation was sufficiently poor that Li-Cs power generation cycle efficiences estimated using surface separators were higher than those using the impinging-jet separators of the types tested to date. However, analyses are presented which show many lines of attack (mainly changes in separator geometry) which should yield much better separation (for impinging-jet separators). Now impinging-jet separators have been built, and others designed, to test these ideas. These (untested) separators are discussed at length in this report. The author concludes that a well-designed impinging-jet separator can likely yield cycle efficiencies greater than those achievable with surface separators. The report also presents some theoretical discussion of the impinging-jet separation process and suggestions for further investigation into this process which may lead to further improvements in impinging-jet separator design.

I. INTRODUCTION

The main concern of this paper is liquid-gas separators. Such separators are proposed for use in MHD power generator cycles either for use in space (Ref. 1) or for large ground-based power plants (Ref. 2). Simplified sketches of some proposed power cycles using liquid-gas separators are shown in Figs. 1 and 2. A few of the most important differences between the cycles sketched in Figs. 1 and 2 are reviewed below.

(1) In the cycle of Fig. 1 (cycle A), a condensible gas (Cs) is used to accelerate the liquid, whereas in the cycle of Fig. 2 (cycle B), a noncondensible gas is used. One reason for this is that the heat rejection temperature in cycle A is much higher than that of cycle B (because rejection must be by radiation to space, with reasonably sized radiators). The respective heat rejection temperatures are ~900 and ~300 K, respectively. Hence, if a noncondensible gas was used in cycle A at this high heat rejection temperature, the gas compression work would be prohibitively high.

(2) In cycle A the generator is downstream of the separator; in cycle B the generator is upstream of the separator.

(3) Cycle A can generate ac power, whereas cycle B is restricted to the generation of dc power. Items (2) and (3) are closely related and will be discussed further.

A. General Comparison of Surface Separators and Impinging-Jet Separators

The older type of separator accelerates the two-phase flow in a nozzle and then impinges the resulting two-phase flow on a solid flat (or gently curved) plate (surface separator). Good separation may be obtained by this means at a cost of considerable reduction in liquid velocity and kinetic energy. The newer type of separator, which is the main topic of this paper, uses the impingement of two (or more) two-phase jets against each other to produce concentration of the liquid (impinging-jet separator). Large reductions in liquid velocity loss may be obtained by this means, although the impinging jet separators built to date do not concentrate the liquid as well as surface separators. Theoretical and experimental work has revealed several promising means of improving the liquid concentration of the impinging-jet separator. There is also the possibility of having a short surface separator located downstream of the impinging-jet separator; this combination might also produce a substantial improvement over the all-surface separator system.

B. Velocity Losses Observed for a Particular Surface Separator

In Ref. 3, data on friction losses are given for two-dimensional surface separators. The experimental configuration is a 50-in.-long supersonic H_2O-N_2 nozzle followed by a curved separator surface on which the two-phase jet impinges at an angle which is initially about 10 deg. The separator portion of the test rig is shown in Fig. 3. The nozzle exit is at the right edge of the picture (the flow is from right to left), and the concentrated water jet leaves through the slot located near the middle of the left edge of the picture. Tests were also run without the separator in place to determine the jet velocity at the nozzle exit. The velocity loss occurring in the separator varied from 0.14 to 0.24 of the velocity at the nozzle exit, depending on the ratio of water flow to nitrogen flow (R_F). The R_F ranged from 20 to 60, with the lower-velocity losses occurring at the higher mass flow ratios. An approximate method of estimation of the velocity losses to be expected in a surface separator is given in Ref. 4 and explains the variation of the loss with R_F.

C. Discussion of the Effects of Surface Separator Losses on the Efficiencies of Cycles in Which the Generator Is Downstream of the Separator

Fractional velocity losses of 0.14 to 0.24 correspond to kinetic energy losses of 0.26 to 0.42 of that available at the nozzle exits. Obviously, this can produce a substantial reduction in MHD cycle efficiency compared to that of a similar cycle in which the separator produces fractional kinetic energy losses of 0.10 to 0.20 (which appear to be attainable with impinging-jet separators). The reduction in cycle efficiency caused by separator friction is even greater than is immediately apparent, since the whole of the jet kinetic energy at the generator inlet is not available for power generation (even assuming no losses of any kind in the generator, diffusers, etc.). This is because the liquid at the generator exit has to have sufficient kinetic energy to be returned (by means of a diffuser) to a high enough pressure to recirculate through the system. For example, for the system described in Table 1, Ref. 1, the generator inlet and outlet velocities are 114 and 65 m/s, respectively, meaning that only 67.5% of the kinetic energy entering the generator is available for electric power generation.

D. Possible Benefits of Replacing Surface Separators With Impinging-Jet Separators in Ground-Based and Space Power Plants

If the expectations for the performance of the impinging-jet separator are realized, higher cycle efficiency will be obtainable in MHD ground-based power plants using advanced impinging-jet separators. References 2 and 5 describe ground-based quasi-Ericsson cycles (typically employing argon and lithium as the working fluids) with the generator upstream of the separator (i.e., the cycle shown in Fig. 2). These cycles were calculated using a surface separator to yield efficiencies of the order of 30%. By the use of an advanced impinging-jet separator in these cycles, the efficiencies could likely be improved by about 10%, that is, from 30 to 33%. The cycles considered in Refs. 2 and 5 have gas-to-liquid volume ratios in the generator channel of 1.8 to 4.5, which according to Refs. 1, 6 and 7 produce electrical conductivities in the channel ranging from 0.035 to 0.15 of the value for the pure liquid. These low values of conductivity restrict the generators to dc operation, thereby requiring auxiliary equipment with attendant losses in efficiency to produce standard 60-cycle power. If the separator was placed upstream of the generator and advanced low-friction impinging-jet

separators were used, gas-to-liquid volume ratios of 0.5 could probably be achieved in the generator channel. Under these conditions, the two-phase mixture conductivity would be 0.5 times the value for the liquid, which is sufficiently high to allow ac power to be generated directly in the MHD channel. (A typical ac MHD generation system is described in Ref. 1). Owing to the much higher fluid velocities occurring in the system where the generator is downstream of the separator, frictional losses (other than in the separator) will be somewhat higher than for the dc systems described in Refs. 2 and 5. However, the overall system efficiency may well be increased particularly when considering the losses incurred in the equipment necessary to convert from dc to ac in the systems proposed in Refs. 2 and 5.

Another example of the advantages available from low-friction impinging-jet separators can be seen in the calculations of Ref. 8 for a space power system. The calculations for Li-Cs separator cycles in Fig. 8 of Ref. 8 (without separator friction) and in Fig. 11 of Ref. 8 (with separator friction calculated for a surface separator) are compared. The maximum efficiency is reduced from 13 to 7% by the separator friction. An advanced impinging-jet separator should be able to increase the cycle efficiency from 7 to 10%.

E. Dimensional Analysis of the Simulation of a Li-Cs Impinging-Jet Separator by a H_2O-N_2 Separator

1. Introduction and assumptions. The subject of the paper is mainly a discussion of separators designed to simulate the conditions of those in Fig. 1 (cycle A). Water and nitrogen were used to simulate the lithium-cesium flow in the proposed power generation cycle.

The dimensional analysis gone through in the selection of the conditions under which to run the water-nitrogen system to simulate the lithium-cesium flow in a typical cycle of the system of Fig. 1 is reviewed. The system considered is sketched in Fig. 4. The following simplifications have been made to keep the number of dimensionless variables reasonable.

(1) No step or expansion is assumed to take place in the region of points A (or anywhere else); hence W represents both the channel width and, divided by a cosine factor, the width of the nozzle exits.

(2) The height of the channel (perpendicular to the paper) H is assumed unimportant; i.e., the flow is assumed to be two-dimensional.

(3) All fluid properties are evaluated at station 1 (the nozzle exit) according to computer calculations made by the methods of Ref. 9.

(4) The droplet diameter D is taken as that calculated by the methods of Ref. 9 at station 1. (In fact, this D value is likely to be about the largest droplet which can exist at station 1; many smaller droplets will also exist.)

(5) The heat and mass transfer properties of the fluids are considered unimportant for the separation process. Thus C_{pg}, C_{pl}, K_g, K_l, and the various diffusion coefficients are not included in the important variables.

2. Important variables and fundamental 10 nondimensional groups. With the above simplifications, the important variables are taken as

$$\alpha,\ \beta,\ W,\ \rho_g,\ \rho_l\ \frac{m_g}{H},\ \frac{m_l}{H},\ D,\ \sigma_l,\ V_l,\ P_l,\ \mu_g,\ \mu_l$$

With 13 parameters and three dimensions, there are 10 nondimensional groups controlling the flow. One way to make the grouping is as follows.

$$\alpha,\ \beta,\ \frac{W}{D},\ \frac{\rho_g}{\rho_l},\ \frac{m_g}{m_l},\ \frac{\mu_g}{\mu_l},\ \frac{\sigma_l}{D\rho_g V_l^2},\ \frac{V_l^2 \rho_g}{P_l},\ \frac{\rho_g V_l W}{\mu_g},\ \frac{m_l}{\rho_l V_l HW} = \frac{1}{r_a + 1}$$

The first six groupings are obvious.

Group 7 is essentially the inverse of the droplet Weber number based on V_l (with the factor of 2 omitted). Group 8, in its present form, is the square of a kind of Mach number based on the liquid velocity and the isothermal speed of sound in the gas. This grouping will be replaced by one which gives more nearly the Mach number at the nozzle exit. The liquid velocity will still be used, but the speed of sound will be taken as that for a

liquid-gas mixture given in Ref. 10, p. 3. This sound speed is given by the following equation (in which the notation is changed to conform to that of this paper):

$$c = (1 + r_a) \left[\frac{P_1}{\rho_1 r_a \left(1 + r_a \frac{\rho_g}{\rho_\ell} \right)} \right]^{1/2} \qquad (1)$$

Group 8 will thus be replaced by $M = V_1/c$. We can fairly satisfactorily interpret M as the Mach number at the nozzle exit because:

(1) The gas never comprises more than 1/14 of the flow for the cases under study; hence V_1 is a fairly accurate representation of the mean jet velocity.

(2) Because of the fine dispersion, large specific heat, and large mass fraction of the liquid, sound waves are likely to propagate under conditions closer to being isothermal than adiabatic.

Group 9 is roughly the gas Reynolds number in the separator channel. The only point preventing group 9 from being exactly this number is that V_1 (the liquid velocity) is used. However, the mean velocity of the gas in the channel is normally within 10 or 20% of V_1.

Group 10 is simply the ratio of the flow volume taken up by the liquid to the total flow volume (r_a = ratio of gas flow volume to liquid flow volume).

From the preceding discussion, the 10 groups will be rewritten as:

$$\alpha,\ \beta,\ \frac{W}{D},\ \frac{\rho_g}{\rho_1},\ \frac{m_g}{m_1},\ \frac{\mu_g}{\mu_1},\ \frac{\sigma_1}{D\rho_g V_1^2},\ M,\ \frac{\rho_g V_1 W}{\mu_g},\ \frac{1}{r_a + 1}$$

Comparisons will be made between the values of these parameters calculated (using the methods of Ref. 9) for the lithium-cesium flow case most likely to be used in cycle A, and for three values of R_F covering the range of tests made with water and nitrogen.

3. Five additional nondimensional groups (obtainable from the original 10) and the reasons for their use. In addition to the 10 parameters

mentioned above, comparisons will be made for five additional parameters, all of which can be obtained by appropriate combinations of the original 10 parameters. These five additional parameters are used because they tend to be the dominant ones affecting particular aspects of the separation phenomena. These five parameters and a brief description of the reason for using them are given below.

Group 11: $\rho_l V_l D/\mu_l$. This grouping gives a rough idea of the ratio of the kinetic energy of two impacting drops of diameter D to the energy dissipated in liquid viscous dissipation during the collision. A more accurate idea might be obtained by replacing V_l in this parameter by the velocity of the approach of droplets to the channel centerline in Fig. 4, that is, $V_l \sin\alpha$. However, the author has chosen not to do this and will compare the values of $\rho_l V_l D_l/\mu_l$ and α separately.

Group 12: $\sigma_l/D\rho_l V_l^2$. This grouping is simply that of Group 8 with ρ_g replaced by ρ_l. It gives an estimate of the ratio of the surface tension energy of droplets of diameter D to their kinetic energy. For studying collision phenomena where the two jets meet (which is the prime use of Group 12), V_l^2 would be better replaced by $(V_l \sin\alpha)^2$. This is a change similar to that mentioned with respect to Group 11 above. Again, it was decided to examine Group 12 and α separately.

Group 13: $\rho_g V_l D/\mu_g$. This is the Reynolds number (based on V_l) of droplets of diameter D flowing through the gas. The importance of this group is in controlling the gaseous dissipation (and also the drag coefficient) of the droplets moving through the gas.

Group 14: $(W/D)(\rho_g/\rho_l)$. The path of droplets of diameter D leaving the nozzle exit is controlled largely by this parameter (ignoring collisions and assuming a constant drag coefficient). The larger this number is, the more difficult it is for the droplets to move sufficiently far laterally across the channel to coalesce into a zone of concentrated liquid in the region of the channel centerline.

Group 15: $(m_l/m_g)(W/D)(\rho_g/\rho_l)$. This group is group 14 divided by group 5. In the computer program of Ref. 9, D is the diameter of the largest droplet which can withstand the maximum aerodynamic drag forces in the nozzle. That is, the surface tension 'strength' $(2\sigma_l/D)$ of the droplet

surface is large enough to withstand these forces. (One of the defects of this computer program is that, downstream of the point of maximum drag force in the nozzle, all the droplets are assumed to have a diameter D.) In fact (see Ref. 11), there will be a wide spectrum of droplet sizes at the nozzle exit, the largest being roughly of the size D. Consider a case where group 14 is sufficiently small that droplets of diameter D leaving the nozzle at points A can fairly easily reach the zone of concentrated liquid near the channel centerline. In this case, however, droplets which have diameters much less than D will turn fairly rapidly to follow the gas flow, which, in turn, is deflected fairly abruptly at the nozzle exit to move parallel to the channel centerline. If no collisions occurred, many of these smaller droplets would fail to reach the zone of concentrated liquid near the channel centerline. Group 15 is important in determining the extent to which the smaller droplets which would not reach the concentrated liquid zone without the benefit of collisions are swept up by collisions with the larger droplets and carried towards the channel centerline. The larger group 15 is, the more efficient are the large droplets in sweeping up the smaller droplets.

4. Comparison of the values of the 15 groups for the Li-Cs and H_2O-N_2 cases. The comparison of the 15 nondimensional groups for the lithium-cesium case and three water-nitrogen cases is given in Table 1. Scanning the values of the parameters listed in Table 1 and concentrating on the H_2O-N_2 data for R_F = 19.1 and 37.5 and the Li-Cs data, it may be seen that most of the groups are simulated to within a factor of 2 or 2.5. Groups 1 and 2 may be perfectly simulated; groups 7, 8, 9, 10, 12, and 14 are simulated to within a factor of 1.7. Groups 4 and 13 are mismatched by a factor of 2, and Groups 3 and 15 are mismatched by factors of 2 to 3, depending on which R_F value is used. By reducing the size of W at R_F = 19.1 (say, by a factor of 1.5 to 2.0), the mismatch of Groups 3 and 15 could be greatly decreased without making the mismatch of Groups 9 and 14 significantly worse. Increasing the outlet pressure of the device to, say, 2 atmospheres absolute could remove the mismatch in Group 4 without making mismatches significantly worse elsewhere. Note that increasing ρ_g by this method changes the flow parameters throughout the nozzle (e.g., D would be changed); hence, one cannot just substitute the higher value of ρ_g in the parameters shown in Table 1.

The existing simulation is, however, felt to be reasonably satisfactory for R_F = 19.1 and 37.5, except for the large differences in Groups 6 and 11 (marked with an asterisk).

5. Detailed discussion of the effects of the large differences of two of the nondimensional groups (6 and 11) and their effect on the simulation process. Groups 6 and 11 differ by a factor of 10 to 12 between the Li-Cs and H_2O-N_2 cases. We concentrate on Group 11, since the fundamental set of 10 groups could have been chosen from the 15 groups of the table by dropping Groups 6, 12, 13, 14, and 15, and Group 11 has a direct physical significance, presented earlier. What the mismatch means is that the amount of viscous dissipation in the liquid in the course of a droplet collision relative to the kinetic energy of the droplets is 10-12 times smaller in the Li-Cs case. The author believes that this is one of the mechanisms which control the size (substantially smaller than that at the nozzle exit) to which the droplets are reduced in the central concentrated liquid zone of the separator by collisions. This substantial reduction in size can be inferred from the very large and small sizes, respectively, of Groups 11 and 12.

The "shock waves" sketched in Figs. 8 (Sec. II.C.1) and 11 (Sec. II.C.3) imply to some extent that the thickness of the "shock" is very small compared to, say, the channel width. However, Fig. 10 (Sec. II.C.3) shows that the liquid density increase takes place in a "shock zone" which is of the order of 0.2 in. thick. Figure 10 shows that the density increase is roughly linear between distances of 0.30 and 0.05 in. from the channel centerline. As droplets enter the zone of rapidly rising liquid density, the following processes are thought to take place. If there were no dissipative processes and no increase in the surface energy of the droplets, the droplet random kinetic energy per unit mass would rise very rapidly in the outer regions of the "shock zone." The rate of rise would rapidly decrease as the shock zone was penetrated more deeply and would be quite slow for the innermost regions of the shock zone. Assuming a linear variation of liquid density, one can readily calculate the value of the random kinetic energy per unit mass of the droplets under the assumptions stated above. At the innermost edge of the shock zone, the random kinetic energy per unit mass of the droplets would have risen to $(V_\ell^2 \sin^2\theta)/2$, where $V_\ell \sin\theta$ is the component

of the velocity of the liquid droplets perpendicular to the channel centerline at the outermost edge of the shock zone.

In a more realistic picture of the shock wave, the following additional processes take place:

First, as soon as the droplets have moved a sufficient distance into the shock zone that the kinetic energy per unit mass has risen to a small fraction of $(V_\ell^2 \sin^2\theta)/2$, the droplets will begin to rapidly decrease in size because of shattering in collisions (this is related to the small magnitude of Group 12). As discussed in the previous paragraph, random kinetic energy per unit mass rises very rapidly in the outermost regions of the shock zone; hence, the point at which the droplets begin to shatter is reached only a very small distance downstream of the outermost edge of the shock zone. As the droplets decrease in size, the surface energy per unit mass will increase (the surface energy per unit mass of a spherical droplet is $6\sigma_l/\rho_l D$). If there were no dissipative processes taking place (the increase in surface energy discussed above not being a dissipative process), using the rough criterion given in Ref. 12 for the separation of regions of coalescence and disruption of droplets, it can be estimated that at the downstream end of the shock zone there would be equal amounts of energy associated with the random kinetic energy and the surface energy of the droplets. Also, under these conditions, an estimate of the mean droplet diameter at the downstream end of the shock zone can be made.

Second, as the droplet random kinetic energy per unit mass rises rapidly and the droplet diameter decreases rapidly in the outermost regions of the shock zone, the rates of processes which tend to dissipate droplet random kinetic energy rapidly increase in magnitude. (Since the droplet diameter is large and the droplet random kinetic energy per unit mass is small outside the shock zone, these processes are relatively unimportant there.) These processes are:

(1) Dissipation due to liquid viscous forces during collisions. See discussion of Group 11.

(2) Dissipation due to aerodynamic drag forces on the droplets. The drag coefficient on an isolated sphere moving at velocity u through a gas can be roughly approximated by

$$C_D = 0.5 + \frac{24\mu_g}{\rho_g u D} \qquad (2)$$

for $\rho_g uD/\mu_g < 2 \times 10^5$ (Ref. 9, Fig. 2). The aerodynamic drag forces also reduce the droplets' directed kinetic energy per unit mass, since the droplets enter the shock zone with a substantial component of velocity perpendicular to the channel centerline, while the gas at this point is moving nearly parallel to the centerline. The former statement is supported experimentally by figures such as Fig. 9, Sec. II.C.1, while the latter is supported by pressure data such as that of Fig. 26, Sec. II.F.2, indicating that while the liquid is compressed by a factor of 4 to 6 (see Sec. II.D), the gas is compressed by a factor of 1.5 or less. Both numbers refer to the maximum density (or mass flux) observed on the separator channel centerline with respect to that at the nozzle exit. The process of (1) above cannot reduce the directed kinetic energy per unit mass of the droplets, since, by definition, if the kinetic energy is perfectly directed, there are no collisions.

The relative rates of dissipation of the random kinetic energy per unit mass of the droplets by processes (1) and (2) vary with respect to many parameters and, in the best picture of the shock zone that we can construct, at some places process (1) is more rapid, at others, process (2).

It should be noted that diffusional processes (including both those treating the droplets as "molecules" of a "gas" and ignoring the real gas and those allowing for eddies of the liquid gas mixture – this being more like turbulent mixing than classical diffusion) have not been considered here in anything like adequate detail. Processes (1) (the plural is used since the author is referring to diffusional transport of energy, mass, or momentum) are estimated to be unimportant in the shock zone, except perhaps for the diffusion of droplet random kinetic energy in the outermost part of the shock zone. Indications that processes (2) are of importance come from estimates of the spreading rate of the zone of concentrated liquid after nearly all of the liquid from the nozzle jets has entered this zone. The diffusion coefficient estimated for mass diffusion by process (1) is smaller than that

required to explain the observed spreading rate by a factor of 100 to 1000. Hence processes (2) must be of importance in this case and may also be important in explaining the structure of the shock zone. Much further work is required in this area of diffusional processes in two-phase flow.

The above paragraph on "diffusion" is more or less a digression from the main line of argument, pointing out a deficiency in the knowledge of the shock zone processes. Returning to the main line of argument, the following conditions of operation of an impinging-jet separator are considered:

Fluids = H_2O-N_2

$R_F = 37.5$

$\theta = 20°$

Separator configuration similar to that shown in Fig. 24, Sec. II.F.2

The droplet diameter at the downstream edge of the shock zone based on considerations of shattering of the droplets and increase of droplet surface energy until it equals the droplet random kinetic energy (with no dissipative processes) is 0.58×10^{-5} ft. A droplet diameter estimated from the measured thickness of the shock zone ($\simeq$0.2 in.) by calculating the distances required by droplets of various sizes to slow down to the component of the gas velocity perpendicular to the shock wave (or zone) is 2×10^{-5} ft. The ratio of these two diameters is $\simeq 3.4$. The author believes the droplet diameters to be determined roughly by the criterion given in Ref. 12, separating regimes of droplet coalescence and disruption. Other things being equal (i.e., ρ_ℓ , σ_ℓ), this criterion gives a droplet kinetic energy per unit mass proportional to 1/D. The author believes that at the downstream end of the shock zone the droplet diameter is determined mainly by the maximum droplet random kinetic energy per unit mass which has been reached somewhere in the shock zone in accordance with the criterion of Ref. 12. Hence, for this particular case, it appears that the maximum droplet kinetic energy per unit mass is about 3.4 times less than that which would occur if no dissipative processes took place.

The preceding arguments have all been in preparation for a final estimate as to how severe an effect on the simulation of Li-Cs flow by H_2O-N_2 flow is made by the large differences in groups 6 and 11. For this estimate

Group 6 is thrown out and the fundamental 10 groups are considered to be Groups 1 to 11, excluding Group 6. Since Group 11 is 10 times larger for the Li-Cs case than for the H_2O-N_2 case, it is concluded that the liquid viscous dissipation on droplet collisions will be considerably smaller relatively for the Li-Cs case. However, the dissipation rate due to aerodynamic forces on the droplets is, in some regions of the shock zone, equal to or greater than the dissipation rate caused by liquid viscous effects during droplet collisions, and the former is controlled by groups which are fairly well simulated between the Li-Cs and H_2O-N_2 systems. Further, even if no dissipation takes place in the H_2O-N_2 system, the maximum droplet kinetic energy per unit mass and the minimum droplet diameter would be different from those estimated from experimental data only by a factor of 3.4.

Finally, we believe that once the droplets have had their random velocities and diameters reduced to conditions where the droplet kinetic energy per unit mass is small enough with respect to the surface energy per unit mass so that the droplets rebound instead of coalesce or disrupt (see Ref. 12, especially Eq. 8, which is approximately correct even for equal sized droplets), very little further dissipation takes place due to liquid viscous action, even in the H_2O-N_2 case.

Taking the above three arguments together, we believe that the relative reduction of the liquid viscous dissipation by a factor of 10 for the Li-Cs case with respect to the H_2O-N_2 case may increase the maximum droplet kinetic energy to, say, half of the no-dissipation (Li-Cs) value (instead of 1/3.4 as estimated for the H_2O-N_2 case discussed), with a corresponding decrease of the maximum droplet diameter. We believe that because the difference in these ratios is relatively small, the H_2O-N_2 system probably gives a satisfactory simulation of the Li-Cs system despite the factor of 10 difference in Groups 6 and 11 between the two cases. However, the reduced liquid viscous dissipation undoubtedly has some effect on the processes in the shock zone, and it would be well to run tests using a liquid with μ_1 about 10 times lower than that of water to see if any significant changes occur in the flow pattern. Unfortunately, many liquids which might be considered for this type of test on the basis of their low viscosities (diethyl ether, hexane, some of the Freons, etc., which have viscosities of the

order of 0.23 to 0.41 times that of water) also have surface tension values which are considerably lower than that of water (0.11 to 0.33 times that of water). Hence, the improvement in simulation with respect to Group 11 would be accompanied by a worsening of simulation with respect to Group 8.

6. Conclusion from the discussion of the simulation of Li-Cs separator flow by H_2O-N_2 flow. Summing up the above discussion, we believe the simulation of Li-Cs flow by H_2O-N_2 flow to be reasonably accurate, despite the factor of 10 difference of Groups 6 and 11 for the two cases. However, it still would be desirable to check the effect of operating the simulating system at values for Groups 6 and 11 much closer to those for Li-Cs, if a suitable liquid can be found.

II. EXPERIMENTS USING KNIFE-EDGE BLOCKS

A. General Description of Apparatus

The apparatus used in the impinging nozzle experiment is shown in Fig. 5. Water and nitrogen, from a sump and a high-pressure supply, respectively, are metered using turbine-type flow meters and then fed to injectors at the upstream ends of the nozzles. The two-phase jets leave the nozzle exits and impinge on each other in the straight channel. The knife edges seen at the end of the straight channel collect the bulk of the water flow which has been concentrated towards the center of the channel, and the resulting jet is then deflected downward into the sump. The reaction of the jet on the test rig is measured using a strain gauge. The bulk of the gas flow (carrying, under some conditions, a substantial fraction of the water flow) is deflected outside the knife edge slot. Part of the water carried in this gas flow is caught in the secondary capture slots and fed to a weigh tank to allow the water mass flow to be determined. Most of the gas flow, still carrying considerable water, leaves the channel through the gas exhaust ports and is passed through a separator and discharged to the atmosphere. The water drain in the separator can be closed off to allow the separator water flow rate to be determined.

B. Parameters Varied

The following parameters were varied in the experiments:

(1) The angle between the centerline of a nozzle and the centerline of the complete apparatus. Angles tested were 5, 10, 15, 20, and 30 deg. As the nozzle angle was varied, the length of the straight channel was changed to allow the knife edges to be located in the neighborhood of the geometric impingement point, the location of the latter being defined as shown in Fig. 6.

(2) The gap between the knife edges. Several set of knife edge blocks were used to investigate gaps of 0.5, 0.75, 1.0, and 1.5 in.

(3) The distance of the knife edge tips downstream of the nozzle exits. This was varied in steps of 1 to 2 in. over 6 in. in the neighborhood of the geometric impingement point.

(4) The ratio of the water mass flow to the nitrogen mass flow. In the experiments to be described, the water and nitrogen mass flows were varied from 80 to 170 lbm/s and 2 to 6 lbm/s, respectively, giving four liquid/gas mass flow ratios (approximately 14.3, 25.0, 52.6 and 83.3).

C. Discussion of the Effect of Various Parameters on R_B, $R_{B,\,min}$, and Z_m

1. Discussion of the bypass ratio R_B as a function of knife-edge position. Figure 7 shows the fraction of water bypassing the primary capture slot R_B as a function of the distance of the knife edges from the nozzle exit x (defined in Fig. 6). Data is shown for four water-to-nitrogen flow ratios R_F at a nozzle angle θ of 20 deg and a knife edge gap G of 0.75 in. All of the R_B vs x curves (i.e., also those for other values of G and θ) are shaped similarly to those shown in Fig. 7: R_B decreases with increasing x to a minimum and then increases as the knife edges are moved farther downstream.

The effect of the divergence of the nozzle walls at the exit on the separator performance will now be discussed. An idealized case, in which aerodynamic forces on the droplets are neglected, is sketched in Fig. 8 (the figure shows one-half of the separator). Typical idealized trajectories

of droplets leaving the nozzle exit are shown as lines 1 to 5. In Section II.D, it is stated that according to a simple theory, the liquid flow on passing through the "shock wave" should be concentrated by a factor of 4. (This is roughly confirmed by experimental data.) However, because of the divergence at the nozzle exit, the liquid flux between points C and D is significantly less than that between points A and B. Hence, even after having been concentrated by a factor of 4 in passing through the "shock wave," the liquid in the outer regions of the "central zone" downstream of, say, point C may have a flux of only 2.5 times that at the nozzle exit. (In the idealized situation, at point x_Q, if there were no nozzle divergence, the flux of liquid would be 4 times that at the nozzle exit completely across the "central zone.") In Section III.B, the problem of the degradation of separator performance caused by nozzle divergence is discussed in more detail.

The minimum value of R_B is referred to as $R_{B,\ min}$. The ratio of the x value at which $R_{B,\ min}$ occurs to the distance from the nozzle exit to the geometrical impingement point (x_{GI}, defined in Fig. 6) is referred to as Z_m $\left[Z_m = x\ (R_{B,\ min})/x_{GI}\right]$. Except for data taken with G = 1.5 in., Z_m ranges from 0.65 to 0.85. For G = 1.5 in., Z_m ranges from 0.80 to 1.10.

Two reasons why Z_m is generally observed to be considerably less than 1.0 are now discussed. First, again referring to the idealized flow paths (1 to 5) sketched in Fig. 8, it can be seen that all of the flow has passed through the shock wave at x_Q. For the shock wave flux concentration ratio of 4 referred to above, x_Q would be about 0.8 (x_{GI}). The second effect of importance involves both the reduction of liquid flux of the flow due to nozzle divergence and the effect of aerodynamic forces on the droplet motion. The droplets initially tend to follow paths typified by lines 1 to 5, but the gas flow is fairly abruptly deflected at the nozzle exit to move parallel to the channel centerline. Hence, the actual droplet paths tend to be deflected towards the direction of the gas steam. Path 5' is a more realistic path for those droplets which, in the absence of aerodynamic forces, would have followed path 5. The combination of these two effects results in a great reduction as one moves downstream of the lateral momentum per unit area of the flow impinging on the "central zone" (compare conditions at $x \approx 4.5$ in., $y \approx 0.3$ in. with those at $x \approx 8.5$ in., $y \approx 0.55$ in. in Fig. 9). This causes rarefaction waves to be propagated into the "central zone" of concentrated

liquid. In addition, the concentrated liquid in the central zone tends to diffuse outwards into regions of lower liquid density. It is believed that, downstream of, typically, $x/x_{GI} \approx 0.7$, the effects of diffusion and of the rarefaction waves are sufficient to cause the liquid flux in the central zone to decrease with increasing x.

Profiles taken across the separator channel using mass flow probes have been used to construct graphs of the distribution of the water flow in the channel. Figure 9 is typical of these graphs. The numbers labelling the contours are the fraction of the water mass flow outside the contour in question. The R_B values taken off such graphs at the points where the knife edges are located in knife-edge tests usually agree fairly well (within 10%) with the values obtained from the latter tests. The fact that R_B is a minimum in the region $x/x_{GI} = 0.6\text{-}0.7$ (for $R_B = 0.15$ to 0.4) is clearly shown in Fig. 9.

2. Discussion of R_B and Z_m as functions of R_F. As the relative water flow ratio R_F is increased, a generally improving separator performance (decreasing R_B values) is shown (Fig. 7). This same dependence was observed for all nozzle angles and knife edge gaps tested, except that under some conditions, the $R_F \approx 83.3$ data showed slightly higher bypass ratios than the $R_F \approx 52.6$ data. A tentative explanation for this dependence is as follows: At the higher R_F values, the velocities and accelerations of the gas flow in the nozzles are lower and hence the absolute velocity differences between the water droplets and the gas tend to be less. Since the surface tension forces at larger droplet diameters are sufficient to withstand the lower aerodynamic forces, higher R_F values would be expected to produce larger water droplets. The flow separator functions by deflecting the gas flow outwards just beyond the nozzle exits, while the water droplets from the two nozzles continue on their converging paths and coalesce in the center of the channel. Thus, at higher R_F values, the larger water droplets should be less affected by the deflecting gas stream, giving better separator performance (see also the discussion of Group 14 in Section I.E.3.) One limitation of the above discussion is that droplet collisions are obviously very important in the real flow (typical mean free path ≈ 0.02 in.).

There is a slight tendency for Z_m to be larger at higher R_F values, other things being equal; this can be seen in Fig. 7. On the average, the

difference in Z_m between data taken at $R_F \approx 83.3$ and $R_F \approx 14.1$ is ~ 0.06. This effect is also probably explainable as being due to the larger droplet size which occurs at higher R_F values, as discussed above. The larger droplets can travel farther downstream in the separator channel before being deflected by the gas to move at a given angle to the channel walls, and thus, at larger R_F values, the region where the lateral momentum flux of the jet impinging on the "central zone" is no longer sufficient to prevent diffusion outwards of the 'central zone' liquid is moved further downstream (see Sec. II.C.1.).

3. Discussion of R_B as a function of G (or R_A). Data taken with a mass flow probe in the knife edge channel is shown in Fig. 10, where R_A is the ratio of the area of the separator channel out to the indicated y value to that of the nozzle exits and is another way of expressing the gap G, had knife edges been used. In the latter case, G would correspond to 2y. x/x_{GI} for the data shown is near the optimum value (Z_m) for G values of 0.5 to 0.75 in. Figure 9 shows that the probe mass flow rate decreases nearly linearly from y = 0.1 to y = 0.3 in. and is nearly constant for 0.8 in. < y < 1.75 in. The flow in the latter region probably consists of small droplets which rapidly turn to follow the gas flow.

The effect of G on Z_m can easily be obtained from examination of the contours of Fig. 9. Figure 9, together with data taken with knife edges, indicates that the smaller the R_B value of the contour or the larger the gap, the farther downstream the optimum concentration of flow occurs. This effect can be explained as follows (refer to Fig. 11 and the following nomenclature):

ρ_A, ρ_B, etc.	concentration of liquid at points A, B, etc.
ρ_{AS}, ρ_{BS}, etc.	concentration of liquid at points just across shock from points A, B, etc.
P_{AS}, P_{BS}, etc.	pressures (considering droplets as hard spheres) just across shock from points A, B, etc.

The ideal case (no aerodynamic forces on droplets, no nozzle divergence, droplets behave like solid spheres) is shown in Fig. 11b. In this case the water fluxes at points A, B, C, etc., are the same, and therefore the water

concentrations and pressures just across the shock from these points are the same. Hence, streamlines 1, 2, 3, etc., after having passed through the shock, are parallel to each other and to the channel centerline. In the more realistic case sketched in Fig. 11a, owing to nozzle divergence and aerodynamic forces on the droplets, the concentrations ρ_A, ρ_B, etc., become less as one moves downstream. Hence, the concentrations and pressures ρ_{AS}, ρ_{BS}, etc., and P_{AS}, P_{BS}, etc., also become less as one moves downstream. This causes rarefactions to be propagated inward from the shock front. A streamline such as streamline 3' after having passed through the "shock" will tend to be deflected away from the channel centerline by these rarefactions. In addition (see Section II.C.1.), the concentrated liquid in the central zone tends to diffuse outward into regions of lower liquid concentration. (This effect would occur even if no rarefactions were propagated inward towards the channel centerline.) Hence, a streamline will have a point of minimum y (as indicated by the tick marks in Fig. 11a). From the geometry of the situation, it can readily be seen that the farther away from the centerline the streamline is, the farther downstream the point of minimum y will be. Comparing Figs. 9 and 11a shows that the theoretical and experimental systems of streamlines (or lines of constant R_B) do not correspond exactly but do show the same tendency for the variation of the point of minimum y of the streamline. Part of the difference between Figs. 9 and 11a may be due to the non-negligible thickness of the shock wave (mean free path upstream of shock is approximately 0.02 in.).

4. Discussion of $R_{B,\,min}$ as a function of θ. Figure 12 shows the variation of $\overline{R_{B,\,min}}$ with θ for four values of R_F at G = 1.0 in. (The data was obtained using knife-edges.) Considering the size of the error bar, and also data not shown in Fig. 12, the differences in shapes of the curves for the different R_F values are probably attributable to scatter in the data. The author believes the "true" curves for all R_F values to be similar in shape to those shown in Fig. 12 for R_F = 14.3 and 52.6. The value of θ at which the minimum value $R_{B,\,min}$ occurs is believed to be in the neighborhood of 18 to 20 deg for all R_F values. The range of values 15 to 22 deg shown in Fig. 12 is also believed to be due to scatter in the data. The shape of the curves shown in Fig. 12 is believed to be due to several phenomena, some

of which tend to increase $R_{B,\ min}$ at small values of θ and others which tend to increase $R_{B,\ min}$ at large values of θ. At some intermediate value of θ (from Fig. 12, at θ = 18-20 deg), the optimum occurs, because the various phenomena behave roughly as sketched in Fig. 13. First, phenomena which tend to increase $R_{B,\ min}$ at decreasing θ are discussed (Type B phenomena).

(1) Nozzle divergence effect (see Fig. 8 and Section II.C.1). In Section II.C.1 the nozzle divergence effect, which in the absence of aerodynamic forces would bring about an easily calculable reduction in liquid flux at point F (Fig. 8) compared to that at the nozzle exit was presented. Since the nozzle has a fixed divergence angle of 5.4 deg, it is apparent that this effect is more severe at smaller θ values. As an example, neglecting aerodynamic forces, the liquid flux at point F in Fig. 8 would be ~0.55 (~0.85) of that of the nozzle exit for a nozzle angle θ of 10 deg (30 deg). The author believes that this phenomenon is the most important of the type B phenomena and can produce large increases in $R_{B,\ min}$ for $\theta < 15$ deg.

(2) Reynolds number effect. The assumption is made (which should be roughly valid in the separator channel at distances greater than 2-5 in. downstream from the nozzle exit, depending on R_F) that there is no difference between the axial velocities of the gas and the liquid. Hence, the aerodynamic force tending to make the droplets move parallel to the gas stream depends on the lateral velocity difference, which is nearly proportional to θ (other parameters, such as R_F, being the same). At smaller θ values the smaller lateral velocity difference means that the Reynolds number of the droplet is smaller, and hence the droplet drag coefficient is larger. This increased droplet drag coefficient at smaller θ values can easily be shown to tend to increase the $R_{B,\ min}$ values as θ is decreased.

Effects which tend to increase $R_{B,\ min}$ for increasing θ (at large values of θ) are now discussed (Type A phenomena).

(3) Effect at large angles which occurs when gas moves parallel to centerline at a speed u and droplets move at an angle θ to centerline at a speed u. The geometry is sketched below with velocity vectors (Fig. 14). Let a liquid droplet start out at point A moving with $u_l = u_g = u$. It can readily be shown that other things being constant (gas density, etc.), the distance the droplet is deflected laterally Δy, after having travelled a time in which, in the absence of aerodynamic forces, the droplet would have traversed a lateral distance y, is proportional to $1/\left[\cos(\theta/2)\right]$, ($\Delta y \ll y$). Hence in the large angle regime, where $\cos(\theta/2) \not\approx 1$, the lateral deflection per unit lateral distance which would have been traversed in the absence of aerodynamic forces tends to increase with increasing θ, which tends to make $R_{B,\,min}$ likewise increase. This is true even when Δy is not $\ll y$, although, for this case, Δy is not exactly proportional to $1/\left[\cos(\theta/2)\right]$.

(4) Further breakup of droplets at the upstream end of the separator channel at large θ values due to large magnitude of the vector velocity difference between the gas and the liquid velocities. In the computer analysis of two-phase nozzle flow (Ref. 9) the droplet size at any point in the nozzle is determined by the criterion: Weber number (We) ≤ 6, where We is given by the following equation:

$$We = \frac{\rho_g (u_g - u_l)^2}{2} \cdot \frac{D}{\sigma_\ell} = \frac{q_s D}{\sigma_\ell} \qquad (3)$$

The dynamic pressure term in the Weber number is $q_s = \left[\rho_g (u_g - u_l)^2\right]/2$. In the nozzle computer program, it is found that q_s rises as one moves downstream, reaching a maximum near the throat, and then decreases somewhat downstream of the throat.

The droplet diameter therefore is computed to decrease as one moves downstream to a point near the throat, and thereafter to remain constant. Downstream of the point of maximum

q_s [q_s(max)], We < 6. For large (> ~ 25 deg) values of θ, the dynamic pressure at the upstream end of the separator channel $\left[\left\{q_c = \rho_g \left|\overrightarrow{u_{gc}} - \overrightarrow{u_{lc}}\right|^2/2\right\}\right.$, see Fig. 14 in paragraph (3) above$\left.\right]$ approaches the maximum value of q_s in the nozzle. A specific example is that for $R_F = 14.9$, $\theta = 30$ deg, $q_{s\,(max)} \approx 69$ lbf/ft^2, and q_c (assuming that $\left|\overrightarrow{u_{gc}}\right| = \left|\overrightarrow{u_{lc}}\right|$, which is conservative) ≈ 57 lbf/ft^2. Allowing for the fact that, by various means, it is estimated that $\left|\overrightarrow{u_{gc}}\right| \approx 1.1$ to $1.3 \times \left|\overrightarrow{u_{lc}}\right|$, it is found that for the case $R_F = 14.9$, $\theta = 30$ deg, $q_c > q_{s\,(max)}$. From these estimates, it appears possible that at large values of θ (θ > ~25 deg), further breakup of the droplets may occur in the upstream end of the separator channel due to the high local values of q_c. Referring to the discussion of Section II.C.2, $R_{B,\,min}$ values would therefore be expected to increase with θ at large values of θ (θ > ~25 deg).

(5) Increased breakup of droplets in the upstream end of the separator channel due to higher velocity differences between large and small droplets at larger θ values. In the upstream end of the separator channel, the larger θ is, the larger is the (mainly lateral) velocity difference between the large droplets which approximately continue on in the direction they had at the nozzle exit, and the gas stream, which rapidly turns to move parallel to the channel walls. Hence, the smaller droplets, which turn fairly rapidly to follow the gas stream, will have higher velocities relative to the large droplets at larger θ values. Collisions between the large and small droplets due to their different responses to the aerodynamic forces become more violent at larger θ values. This should produce a greater decrease in the mean droplet size in the upstream end of the separator channel at larger θ values. By the same argument referenced at the end of paragraph (4) above, this would also cause the value of $R_{B,\,min}$ to increase with increasing θ.

To recapitulate, the interaction between phenomena 1 and 2 and phenomena 3, 4 and 5 is believed to produce effects on $R_{B,\,min}$ of the nature

sketched in Fig. 13, thus roughly (though not quantitatively) explaining the nature of the experimentally observed data of Fig. 12.

Examination of the data on Z_m as a function of θ indicates, for some G values, a tendency for Z_m to increase somewhat with increasing θ. The author can offer no satisfactory explanation for this increase and why it does not occur at other G values.

D. Discussion of the Observed Constancy of the Ratio of the Maximum Water Flux in the Channel to That at the Nozzle Exit

It has been observed that for probe data taken with $\theta = 10$ deg, at $R_F = 83.3$, 52.6, 25.0, and 14.3, and with $\theta = 15$ deg, at $R_F = 52.6$, the ratio of the maximum water flux in the center of the channel to that at the nozzle exit is in a narrow range: from 4.6 to 5.7. The apparent constancy of this ratio is in rough agreement with a simple theory which treats the water droplets at the nozzle exit as a monatomic gas travelling at $M = \infty$. This theory predicts a water flux ratio of 4 regardless of θ or R_F.

E. Discussion of the Ratios of the Mean Velocity of the Jet at the Nozzle Exit (Using Nozzles Only, Without Separator) to the Isentropic Velocity Calculated for the Same Conditions

Figure 15 shows the calculated and measured values of the ratio of the mean jet velocity at the nozzle exit to the calculated ideal (isentropic) velocity for the same conditions. The calculations were done by the techniques outlined in Ref. 9. The isentropic velocities were calculated using Eq. (VI-6), p. 166, Ref. 10. In the calculation of real nozzle performance, a fixed pressure profile was used for all values of R_F. Because of this, the calculated nozzle area ratios (exit area/throat area) are different for each value of R_F. Figure 16 shows the variation of the calculated area ratios with R_F and also the area ratio of the nozzle used in the experiments. According to Fig. 16 the experimental nozzle should be underexpanded for $R_F > 34$. Figure 17 shows experimental pressure profiles in the nozzle for various R_F values and also the theoretical profile used in the calculations mentioned above. From Fig. 17, the experimental profiles move past the theoretical profile at about $R_F = 20$; however, close examination of the portion of the $R_F = 26.31$ profile for 0 < (distance from nozzle exit) < 4 in. indicates signs of underexpansion. Whether one says that the change from underexpansion to overexpansion as determined from Fig. 17 takes place

at $R_F \approx 20$ or $R_F \approx 30$, the author believes this to be in reasonable agreement with the changeover value of $R_F = 34$ obtained from Fig. 16. This is because of many difficulties of the calculation of nozzle performance, two of which will be mentioned here. First, the drag coefficient for droplets was taken in the analysis of Ref. 9 as that of solid spheres; experimental work has indicated that the drag coefficient of liquid droplets may differ by as much as a factor of 4 from those of solid spheres (see discussion of this in Ref. 9, p. 8-10). Secondly, the handling of the two-phase boundary layer in Ref. 9 is subject to much question.

The experimental and theoretical values in Fig. 15 for $P_{\text{NOZZLE INLET}}$ (P_{NI}) = 150 psia are now compared. The maximum difference in $V_{jet}/V_{isentropic}$ is 0.02. It is noted that the theoretical curve shows a minimum at $R_F = 25$. The experimental curve does not show this, but there is a considerable reduction in slope as one moves from $R_F \approx 80$ to $R_F \approx 15$. However, the experimental data for $P_{NI} = 110$ psia, which covers a much wider range of R_F values, does show a minimum in $V_{jet}/V_{isentropic}$, albeit not of the gently rounded shape of that of the theoretical curve.

The two effects believed to be responsible for the shapes of the curves of Fig. 15 are as follows:

(1) As R_F is decreased, the droplet size becomes smaller. This is because the gas (and liquid) velocities are higher (since the gas is less heavily loaded with liquid), and hence, the aerodynamic pressures on the droplets (which move at a lower velocity than the gas) are higher. Hence, the droplets break up to a smaller size, which enables the surface tension "strength" of the droplets ($\approx 2\sigma_l/D$) to withstand the aerodynamic forces. It can readily be shown that the smaller the droplet size, the closer the droplet velocity will be to the gas velocity (on a fractional basis). One of the main reasons that the mean jet velocity is lower than the isentropic value is that the droplets leave the nozzle with a substantially lower velocity than the gas. Hence, with respect to this effect, higher values of $V_{jet}/V_{isentropic}$ would be expected at lower R_F values. This effect is apparent in Fig. 15 in the theoretical curve for $P_{NI} = 150$ psia for $R_F < 25$ and in the experimental curve for $P_{NI} = 110$ psia for

$R_F < 11$. It is not apparent in the experimental curve for P_{NI} = 150 psia, although the slope of this curve decreases as one moves from $R_F \approx 80$ to $R_F \approx 20$.

(2) To understand the second effect, we begin by repeating that an important reason that the jet velocity is less than the isentropic velocity is that the droplets leave the nozzle at considerably lower speed than the gas. When R_F is small (so that the fractional volume of the flow occupied by the liquid is small), the process in the nozzle (somewhat simplified) could be described as follows: the pressure gradient force accelerates the gas, and the gas accelerates the liquid through the liquid-gas drag force. However, when R_F is large, the liquid occupies (on the average, over the length of the nozzle) a substantial portion of the volume of the flow. Hence, the pressure gradient can do a significant fraction of its acceleration of the liquid by acting directly on the liquid (irrespective of liquid-gas drag forces). Thus, at large R_F values, $V_{jet}/V_{isentropic}$ tends to increase with increasing R_F because an increasing fraction of the pressure gradient forces act directly on the liquid, thus reducing the importance of the liquid-drag force. In the extreme case of a nozzle operating completely filled with liquid, the liquid-gas drag force has vanished, and $V_{jet}/V_{isentropic}$ would be much closer to unity than any of the values shown in Fig. 15, being limited only by friction effects. For small R_F values ($R_F < 10$-25) the fraction of the volume of the flow occupied by the liquid is believed by the author to be so small that this effect is overshadowed by the droplet size effect (Effect 1).

These two effects are believed to qualitatively explain the nature of the curves shown in Fig. 15. Effect 1 is predominant for low R_F values; Effect 2 predominates at higher R_F values.

The difference between the theoretical and experimental curves of Fig. 15 for P_{NI} = 150 psia cannot be explained here, but may be connected with the difference between the area ratios (see Fig. 16) and pressure profiles (see Fig. 17) of the nozzles furnishing data points at corresponding

values in Fig. 15. Also, the difficulties and possible errors which may occur in the theoretical analysis may contribute to this disagreement.

F. Discussion of the Effect of Various Parameters on V_{jet}

1. Effect of θ on V_{jet}. Figure 18 shows curves of V_{jet} versus nozzle angle for $R_F = 25.0$ and for the four different knife-edge gaps. The data shown was taken at the value of x where R_B was a minimum. The peculiar shapes of some of the curves are believed by the author to be due to the fact that the velocity data has not been normalized. For a presentation of the type of Fig. 18, the velocity should be presented in the form of V_{jet} divided by the isentropic velocity calculated for the nozzle for the conditions of that particular run (normalization). Variations in R_F from the nominal value, variation in P_{NI}, water temperature, etc., can cause considerable ($\sim\pm 10$ ft/s) variations in the calculated isentropic velocity for the nozzle. Hence, only the general trend of the curves of Fig. 18 can be taken as truly indicative of the variation of V_{jet} with θ. Simple momentum calculations predict that V_{jet} should fall off as cos θ, other things being equal. The solid line in Fig. 18 is that of 340 cos θ ft/s. Ignoring the peculiar shapes of some of the experimental curves between $\theta = 15$ and 20 deg, it can be seen that V_{jet} falls off more rapidly at $\theta = 30$ deg than predicted by the cos θ calculation. The author has no explanation for this fact, but believes that a substantial fraction of the variation of V_{jet} with θ seen in Fig. 18 is due to the cos θ effect.

2. Discussion of the variation of the jet velocity with separator configuration (knife-edge gap and axial position) and R_F.

a. Introduction, normalization of data, form of data and causes of error. This section, ideally, should be a discussion of $V_j/V_i = f(x, G, R_F)$. However, as time was not available for the calculation of all the V_i values required for normalization, unnormalized V_j values are used. For a given nominal R_F value, variations of the true R_F, P_{NI} and the water temperature can produce variations of V_i of the order of $\sim 0.75\%$. Thus, scatter of this order is to be expected in comparisons of unnormalized V_j data. For different R_F values, both V_j and V_i values differ considerably. A rough normalization allowing for the variations of R_F was done by multiplying the V_j value for the separator data by the following ratio obtained from nozzle-only runs:

$$\frac{V_j(\text{nozzle only, } R_F = 14.9)}{V_j(\text{nozzle only, } R_F = R_{F1})}$$

where R_{F1} is an R_F value for the nozzle-only run, which is very close to that for the separator run data being normalized for R_F difference; V_j data normalized for R_F differences is denoted by V_{jn}. The difference between the R_F value for the separator run under consideration and for the nozzle-only run giving the V_j value in the denominator of the above expression introduces some additional slight scatter to the data. The above normalization procedure accounting for variations in R_F means that, for example, for V_j values of ≈ 230 ft/s at $R_F \approx 86$, V_{jn} will be ≈ 420 ft/s (i.e., similar to the true V_j values for runs at $R_F \approx 15$).

Great difficulty is introduced into the interpretation of the data, because P_{NE} cannot be independently controlled and has a strong effect on V_{jn}. The data available are of the following form:

$$V_{jn} = f(x, G, R_F) \tag{4}$$

$$P_{NE} = g(x, G, R_F) \tag{5}$$

Consider now, the effect on V_{jn} of varying x at constant G and R_F. From the existing data, it cannot, in general, be determined whether the observed changes in V_{jn} are due directly to the change in x, and would occur even if P_{NE} were kept constant, or to the changes in P_{NE} (caused by the changes in x), and would occur if these changes in P_{NE} were made at constant x. Effects of both types may, of course, be occurring as x is varied. What is needed to separate the effects of the four variables is data of the form:

$$V_{jn} = h(x, G, R_F, P_{NE}) \tag{5a}$$

which is not available. Further investigations of knife-edge separator performance should have a means of varying P_{NE} independently of x, G, and R_F. This could easily be accomplished by the addition of sliding doors in the gas escape ducts.

Figure 19 shows the form in which data is presently available. The surfaces shown in this figure are such as might be obtained from Eqs. (4) and (5) above by setting $V_{jn} = V_{jn1}$, V_{jn2}, etc., and $P_{NE} = P_{NE1}$, P_{NE2}, etc. As noted in Fig. 19, the surfaces shown therein bear no resemblence to the true V_{jn} = const. and P_{NE} = const. surfaces, but are illustrative surfaces to keep the sketch simple. The true form of the V_{jn} = const. and P_{NE} = const. surfaces can be estimated from Fig. 20, which shows sections of the three-dimensional space of Fig. 19 parallel to the x-G plane.

Typical such sections are sketched, in part, in Fig. 19, and labelled with their R_F values.

b. Variation of V_{jn} with P_{NE}. Extensive analysis has been made of the sections shown in Fig. 20 and also of sections of the three-dimensional space of Fig. 19 taken parallel to the R_F-G and x-R_F planes. Also, similar analyses (by taking sections parallel to two coordinate axes) have been made by replacing the R_F axis by a P_{NE} axis. (In this case, in the three-dimensional space corresponding to that of Fig. 19, the surfaces are those of constant V_{jn} and constant R_F.) The picture obtained from these analyses is extremely complicated. One strong effect is apparent — the variation of V_{jn} with P_{NE}. There is also some evidence for a small variation of V_{jn} with x under certain conditions.

The former effect is now discussed in detail. Figure 21 shows the variation of V_j with P_{NE} at $R_F \approx 14.9$ and for a range of values of G and x. The various data points for any given G value were taken at different x values. Figure 22 shows similar data for $R_F \approx 86.3$. In Fig. 22, the true V_j values, not normalized to V_{jn}, are given. In Fig. 23, the mean curves including those shown in Figs. 19 and 20 are given for four R_F values, the V_j values now being normalized to V_{jn}. Typical experimental geometry for these tests is shown in Fig. 24.

Effect due to nozzle operating at higher than design exit pressure. Part of the reason for the reduction of V_j with increasing P_{NE} is simply the fact that the two-phase nozzle is operating at higher than design exit pressure. One might expect that in the final expansion of the jet to atmospheric pressure (see Fig. 24) this loss would be recovered. This probably does not occur because of the concentration of the liquid which takes place in the separator channel, at roughly the nozzle exit pressure (Fig. 24). After the

fluid enters the knife-edge gap and eventually reaches atmospheric pressure, even in the idealized case where slips between the phases and gas entrainment are ignored, the jet would not be expected to recover the velocity loss, because it now typically carries about four times as much water per unit mass of gas as at the nozzle exit, and thus the pressure gradients would be strong enough to allow recovery of only about 1/4 of the velocity lost.

Comparison of observed reductions in V_{jn} with increasing P_{NE} with those estimated for effects occurring in the nozzle. The fractional velocity losses (per psi change in P_{NE}) observed to occur with increasing P_{NE} (on the steepest regions of the curves of Figs. 21, 22 and 23) are of the order of 0.045 psi^{-1}. Fractional velocity losses per psi change in P_{NE} estimated from the nozzle computer program output data obtained by the techniques of Ref. 9 at various distances upstream from the nozzle exit are ~0.0115 psi^{-1}. The corresponding figures estimated by extrapolation from nozzle-only runs at varying nozzle inlet pressures are ~0.0074 psi^{-1}. This procedure, which does contain several possible causes for error, is as follows. If data at P_{NE} = 20 was to be simulated, the nozzle would be operated at a nozzle inlet pressure of 150 × 14.2/20 = 106.5 psia, where 150 psia is the standard nozzle inlet pressure and 14.2 psia is the atmospheric pressure at the laboratory.

Possible explanations for the differences between the measured variation of V_{jn} with P_{NE} and the estimated variation due to effects occurring in the nozzle (made in the preceding section). First, static pressure profiles taken along the last 6 in. of the nozzles and along the channel centerline (including both the separator channel and the region between the knife-edge blocks) are reviewed with a view to searching for regions of adverse pressure gradient where severe losses of liquid velocity might occur, for reasons which will be discussed subsequently.

For many combinations of x, G, and R_F tested, no adverse pressure gradients were observed in the nozzle for P_{NE} values up to 5.5 psig. The nozzle pressure taps had not been made at the time of the tests yielding the P_{NE} values > 5.5 psig shown in Figs. 20, 21 and 22 were made. While there is no way to be certain that adverse pressure gradients in the nozzle do contribute to the unexpectedly rapid fall-off of V_{jn} with increasing P_{NE} (Fig. 23) for P_{NE} >5.5 psig, most (~80%) of the data under discussion is

for $P_{NE} < 5.5$ psig, and from Fig. 23, the highest values of $d(V_{jn})/d(P_{NE})$ occur for $P_{NE} < 5.5$ psig. Thus, it appears likely that adverse pressure gradients in the nozzle are not important as a cause of unexpectedly high values of $d(V_{jn})/d(P_{NE})$ shown in Figs. 21, 22 and 23.

Pressure taps along the bottom surface of the channel (at the centerline) have indicated no adverse pressure gradients in the region of the knife-edge tips (say, from 1 in. upstream to 4 in. downstream of the tips) over a wide range of x, G, R_F and P_{NE} values (some of this data has been taken at P_{NE} values as high as 8 psig).

Along the centerline of the separator channel, from a distance of 0 to ~4 in. downstream of the nozzle exit, there is observed, in general, a region of pressure greater than P_{NE} (e.g., see Fig. 25). (Note: this profile differs somewhat from that shown in Fig. 24 because of different scales for the ordinates and abscissae and different values of x, G, and R_F.) The 'hump' observed between x = 0 and x = 4 in. is due to the lateral momentum carried by the impinging jets.

The following rough calculation shows that the height of the "hump" is of the right order of magnitude.

Thrust of nozzles only ≈ 1200 lbf

Area of nozzle exits ≈ 18 $in.^2$

Thrust of nozzles per unit exit area ≈ 1200/18 = 66.7 $lbf/in.^2$

Expected impact pressure (inelastic collisions) of this jet on an imaginary plate along the channel centerline ≈ 66.7 x $(\sin 15 \text{ deg})^2$ ≈ 4.5 psi

The 4.5 psi compares well with the height of the 'hump' observed in Fig. 25. This height is ~4.8 psi if taken from the curve through the points marked with circles and ~5.5 psi if taken from the points marked with squares (somewhat off the centerline of the channel) to the peak of the hump. At $R_F \approx 15$, the corresponding numbers are typically ~1.8 psi and ~3.0 psi. The explanation for the behavior of curve D (Fig. 25) downstream of the peak and why the maximum observed pressure on the separator channel centerline is not as much above P_{NE} at lower R_F values is as follows. The gas at the channel centerline is compressed by passing through oblique

shock waves (see Fig. 8, Section II.C.1 and Fig. 11, Section II.C.3); this creates a strong lateral pressure gradient. For example, compare wall and centerline pressures at x = 2 in., Fig. 25. The gas is believed to flow laterally through the water droplets away from the channel centerline (driven by this pressure gradient), hence, the falloff of centerline pressure noted downstream of x = 2 in. in Fig. 25. Further, the lower R_F is, the smaller is the volume fraction of the flow occupied by the liquid and the easier it is for the gas to escape from the high-pressure region formed along the channel centerline. This is believed to account qualitatively for the smaller differences between the peak "hump" pressures and P_{NE} values observed at lower R_F values.

While the adverse pressure gradient existing upstream of the maximum of the "hump" may produce some abnormally high frictional velocity losses, it is not believed to be the cause of the decrease of V_{jn} with increasing P_{NE} shown in Fig. 23 for the following reason. The shape and size of the "humps" are almost independent of x, G and P_{NE}, although they do depend on R_F. For example, the height of the "hump" (taken as the pressure difference between points on the channel centerline located 0.25 in. downstream of the nozzle exit and at the pressure maximum) varies only from 4.4 to 5.0 psi for a wide range of x, G, and P_{NE} for $R_F \approx 86$. Hence, the adverse pressure gradient effects associated with the "hump" are believed to be nearly invariant as one moves along any one of the curves of Fig. 23 and thus should not contribute to the observed decrease of V_{jn} with increasing P_{NE}.

The location where the effect of adverse pressure gradients are believed to be likely to contribute significantly to the unexpectedly high values of $d(V_{jn})/d(P_{NE})$ seen in Fig. 23, is downstream of the minimum pressure point between the knife-edge blocks (see Fig. 24). The arguments relating to this effect are discussed in some detail below.

(1) From the pressure profile shown in Fig. 24, it is apparent that the flow traverses an unfavorable pressure gradient from the point of lowest pressure to the exit at atmospheric pressure. The minimum pressure occurring between the knife edges varies roughly linearly with P_{NE} (from $\approx$ -1.7 psig at $P_{NE} \approx 0.7$ psig to -4.6 psig at $P_{NE} \approx 5.2$ psig; data is only available over this

pressure range). The subatmospheric pressures are probably caused by the entrainment of air, which is known to occur, and is sketched in Fig. 24.

It is known (Ref. 13) that diffusers operating with gas-liquid flows at the volume ratios herein considered (gas-to-liquid volume ratios = 3 to 18) are extremely inefficient. Applying the momentum equation to an inefficiently operating diffuser indicates that the overalll average wall friction in the diffuser channel must be abnormally high (compared to, say, that in a pipe, or over a flat plate at zero pressure gradient with similar flow volume ratios, velocities, fluid densities, etc.). The friction calculation used in the nozzle computer calculation (see Sec. II. E) is that of Ref. 10, p. 181-184, which is supported by two-phase flow data in a constant-area channel. This method of calculation essentially assumes that the fraction of the friction area wetted with the liquid is $1/(1+r_a)$. Under adverse pressure gradient conditions, this fraction may be much greater than $1/(1+r_a)$. Two other phenomena which may contribute to the unexpectedly high values of $d(V_{jn})/d(P_{NE})$ in Fig. 23 are discussed briefly below.

(2) Entrainment of air by the jet, which is known to occur, and is sketched in Fig. 24, may produce a "negative thrust augmentor effect." This phenomenon may contribute to the observed reduction of V_{jn} with increasing P_{NE} but cannot explain the observed magnitude of the change, because the calculated integrated pressure force on the surfaces A is too small to do so by a factor of 5 to 10.

(3) The higher P_{NE}, the higher is the pressure in the separator channel (see Fig. 24). By continuity, the average velocity of the gas in the channel must be lower at higher P_{NE} values; this may contribute somewhat to the unexplained magnitude of the reduction of the jet velocity. This contribution is believed to be of little importance, since the gas flow is, at most ~1/15 of the liquid flow.

Most likely explanation for the unexpected magnitude of reduction of V_{jn} with increasing P_{NE} and tests proposed to check this explanation. From the discussions of the previous section, the author believes that the friction along the top and bottom surfaces of the channel (between the knife-edge blocks) in the region of adverse pressure gradient is very large compared to that which would occur at zero pressure gradient and is the main cause of the unexplained magnitude of the reduction of V_{jn} with increasing P_{NE}. This possibility could be tested by constructing a separator of the form sketched in Fig. 26, which is nearly identical to the separator sketched in Fig. 24, up to the knife-edge tips. The separators used in the knife-edge experiments done to date have knife-edge blocks (sketched with dotted lines in Fig. 26) which force the jet to move through a long diverging channel before reaching atmospheric pressure at line C. This configuration is believed to be responsible (through air entrainment, see Fig. 24) for the subatmospheric pressures and adverse pressure gradients such as those shown in Fig. 24. The separator sketched in Fig. 26 quickly turns the gas 90 deg, and while there is a short region of divergence of the channel of the concentrated jet downstream of the knife-edge tips, the shortness of this region combined with the fact that the jet is exposed to atmospheric pressure on the top and bottom at line B, should eliminate or greatly reduce the magnitude of subatmospheric pressures. If the sharp turn of the gas flow is found to increase P_{NE} inordinately, expansion of the gas escape channel downstream of lines A would likely reduce this effect.

c. Recommendations and predictions for separators operating in power cycles. No completely satisfactory explanation for the large magnitude of the decrease of V_{jn} with increasing P_{NE} has been found. The explanation proposed is believed to be the most likely explanation; but much further work is needed to confirm or disprove this. If that explanation was correct, the severe velocity loss problem discussed above would probably not occur in a power cycle system for the following reasons.

(1) Two-phase flow in an adverse pressure gradient would not occur until the r_a values had been reduced to 1 to 1.5, regimes where diffuser efficiencies are higher (0.65 - 0.75, see Ref. 13). In a power cycle design, the impinging-jet separator would

possibly be followed by a short surface separator to bring the r_a values into these regimes.

(2) If the separator gas discharge pressure were to be, say, 14.2 psia, the separator channel and gas escape passages would be designed to keep P_{NE} as close to 14.2 psia as possible. This would allow the greatest possible expansion of the liquid-gas flow in the nozzle to be achieved. If the lowest possible pressure of P_{NE} attainable is, say, 16.2 psia, the nozzle length and contour would be optimized for this value of P_{NE} (see methods discussed in Ref. 9).

Let us suppose that the explanations for the large magnitude of decrease of V_{jn} with increasing P_{NE} presented in paragraphs (1) and (2) above are incorrect, and the velocity loss does not occur in the space between the knife-edge blocks, but either (1) in the nozzle, or (2) in the separator channel. If this is so, the author can present no explanations, but the velocity losses should be minimized by the following procedures. First, the gas discharge channels should be designed so that P_{NE} is as close as possible to the separator discharge pressure; and second the nozzle should be optimized for this P_{NE}. Both of these steps would increase the jet velocity at the nozzle exit, and should eliminate the possibility of shocks in the nozzle, although pressure measurements (see Section II.F.2) give no evidence of shocks in the nozzle up to P_{NE} values of 5.5 psig. If the loss occurs in the separator channel, we can give no reason why the above steps should decrease the loss other than the experimental data of Figs. 21, 22, and 23.

G. Detailed Comparison of Surface and Impinging-Jet Separator Velocity Losses (Including the Effect of Liquid Flow Bypassing the Main Capture Slot)

1. Introduction of the "total velocity loss" factor for a separator y, allowing (with certain assumptions) for the effect of flow bypassing the main capture slot. A new parameter, y, is introduced, defined as

$$y = 1 - (1 - z)(1 - R_B) \tag{6}$$

The parameter y is the fractional reduction from the nozzles-only velocities which would occur in the separator if the liquid flow in the main jet leaving between the knife edges was mixed with the flow having bypassed the knife edges, the equipment for the collection of the latter (secondary capture slots, etc.) having been assumed to reduce its velocity to zero at the pressure of the main jet. The parameter y is an indication of the velocity loss at which a given separator can deliver the total liquid flow to the generator, assuming the above-mentioned type of handling of the bypass flow.

2. Presentation of y and z values for surface and impinging-jet separators. Figures 27 and 28 show the variation of y and z with R_A for $\theta = 10$ deg at $R_F \simeq 14.9$ and 86.0, respectively, with the data taken for that x-position which yields the minimum value of y. In addition, surface-separator data (y_s and z_s) taken at nearly identical nozzle exit conditions is shown. This data is from the separator discussed in Section I.C and shown in Fig. 3. In Fig. 3, the primary capture slot is located near the center of the left edge of the picture (the nozzle exit is located at the right edge of the picture). By following the sharply curved separator surface downstream from the primary capture slot, one will come to the secondary capture slot, which is quite narrow and located in the top left part of the picture. In fact, a series of y_s and z_s points could be shown; these could be obtained by varying the primary capture slot width (and hence, R_A), see Sec. I.C. and Fig. 3. But the single set of points shown is believed to be taken near the operating point of the surface separator which would yield the highest cycle efficiency (η: see Sec. II.H).

3. Discussion of optimization of y and z for a surface separator; from this follows an explanation of the optimized y and z values presented in Figs. 27 and 28, Section II.G.2. For a given nozzle exit condition, there is an optimum length L for the surface separator, measured along the curved surface from the nozzle exit to the primary capture slot. If L is too short, the mean angle of impingement of the jet on the surface (ϕ) becomes large and $\cos\phi$ losses become severe. For example, if ϕ averages 30 deg, there is a $\cos\phi$ velocity loss of $1 - \cos\phi = 0.134$. On the other hand, if L is too long, the $\cos\phi$ losses may be reduced to negligible values, but the friction loss becomes very great. A simplified theory for a flat plate surface separator which, however, presents the basic optimization well is

given. The loss due to impact at an angle ϕ varies as $1 - \cos\phi$, and the friction loss is given by $a/\sin\phi$. The numerical value of a is determined primarily by the skin friction coefficient and r_a at the nozzle exit. The skin friction coefficient for a given nozzle exit size and given liquid properties varies only a relatively small amount over the range of R_F investigated; in these cases, the friction losses are determined primarily by r_a, which can be related to R_F as follows:

$$R_F = \frac{\rho_\ell u_\ell}{\rho_g u_g} \frac{1}{r_a} \tag{7}$$

In Eq. (7), all quantities are evaluated at the nozzle exit. For a given liquid-gas combination, at a fixed P_{NE}, ρ_ℓ / ρ_g is a constant, and over a wide range of R_F values u_ℓ / u_g varies only $\simeq \pm 6\%$. Hence, r_a is roughly proportional to $1/R_F$. The nature of the two types of surface separator losses is sketched in Fig. 29, which presents the friction and cos ϕ losses for a flat plate surface separator for two different values of a, 0.0417 and 0.00555. The appearance of an optimum ϕ value and its qualitative behavior with the variation of a are shown. For the simplified model of Fig. 29, L (the separator length) is given by $W/\sin\phi$, where W is the width of the nozzle exit.

The point of the discussion of the optimization of L (or ϕ) of a surface separation is that the same arguments apply, with slight modification, to the curved surface separator yielding the y_s and z_s data of Figs. 27 and 28. Using this slightly modified version of the theory yielding the curves presented in Fig. 29, values of y_s and z_s for an optimized curved surface separator were estimated for the nozzle exit conditions of Figs. 27 and 28. The resulting estimates are shown in these figures as the y_{so} and z_{so} points. It is noted that on the basis of ratios of y_s to y_{so} and z_s to z_{so}, the surface separator used appears to be fairly close to the optimum length for $R_F \simeq 14.9$ operation and considerably farther from the optimum for operation at $R_F \simeq 85.0$. The z_{so} value for $R_F \simeq 86.0$ (Fig. 28) lies between the two optimum values shown in Fig. 29, and the z_{so} value for $R_F \simeq 14.9$ (Fig. 27) lies somewhat above the higher of the two.

4. Discussion of the closeness of simulation of a Li-Cs system achieved by the separators yielding the data of Figs. 27 and 28. It is noted

here that from the considerations of dimensional analysis presented in Secs. I.F.4 and I.F.5, the best simulation of the proposed Li-Cs power cycle is obtained with H_2O-N_2 flow at $R_F \simeq 28$. On the basis of the ratio of this value to those of Figs. 27 and 28, the desired conditions are somewhat closer to those of Fig. 27 (factor of ~2 difference in R_F values) than to those of Fig. 28 (factor of ~3 difference); hence, slightly more attention will be paid to the data of Fig. 27.

5. Detailed discussion of the y and z data presented in Figs. 27 and 28. First, an important digression is made. It is noted that from the definition of z (see nomenclature), the z and z_s (and y and y_s) values shown in Figs. 27 and 28 should not strictly be compared. Such a comparison involves the tacit assumption that for nozzle-only operation the mean jet velocities at the nozzle exits of the two nozzles used in the impinging-jet separator tests (see Fig. 51, Sec. VI) are the same as those of the single nozzle used in the surface separator tests (see Ref. 9, Fig. 16), for the same nozzle inlet conditions. This is not strictly true, but the difference in nozzle exit velocities in nozzle-only operation varies from ~0.5% at $R_F \simeq$ 86.0 to ~3.5% at $R_F \simeq 14.9$. Figures 27 and 28 should have been corrected for this difference, but this was not done because of lack of time. However, the differences are small enough so that the following discussion, which disregards said differences, is still valid. Similar considerations can be shown to have made the calculated cycle efficiencies presented in Sections II.H, IV.A, and IV.B, 0.3-0.4% too high, but the discussions therein remain valid.

Returning to the main discussion, it is noted that the y values for the surface separator (especially y_{so}) are superior (i.e., smaller) than extrapolated values from the impinging-jet separator by a substantial amount. This is because of the very much greater values of R_B for the impinging-jet separator. For example, from Fig. 27 at $R_A = 7.51$, considering y, z, y_s, and z_s values, R_B for the surface separator is ~0.025, whereas for the impinging-jet separator, R_B would be ~0.40. It must be pointed out that the data of Fig. 27 and 28 is for the very first series of impinging-jet separators made, and improved designs which have been tested have shown considerably better performance. These impinging-jet separators are discussed in later sections. Further, even the impinging-jet separators of

Figs. 27 and 28 can give a substantially better showing relative to the surface separator, in terms of cycle efficiency, if it is assumed that the flow bypassing the main capture slot can be returned to the nozzle inlet by means of a further (surface) separation process followed by a diffusion process (see Secs. II.H, IV.A and B). This is a distinct possibility.

Note that the z values for the impinging-jet separator, particularly those at $R_F \simeq 14.9$, $R_A \simeq 3$, are much lower than z_s or z_{so} for the surface separator. The higher values of z at $R_A \simeq 5$-6 for the impinging-jet separator are probably due mainly to the higher values of P_{NE} which occur under these conditions (see Section II.F.2.b) and could be reduced to the values at $R_A \simeq 3$ by proper design of the gas escape passages (see Section II.F.2 and Fig. 24). Assuming, then, that the values of z shown in Figs. 27 and 28 for the impinging-jet separator at $R_A \simeq 3$ can be achieved at higher R_A values (for advanced impinging-jet separators), the ratio of these values to the values of z_{so} shown are ~0.24 and ~0.28 for $R_F \simeq 14.9$ and $R_F \simeq 86.0$, respectively. This shows the great potential of the impinging-jet separator for reducing friction losses.

6. Discussion of (1) the weak point of the impinging-jet separator, relatively high R_B values and (2) differences in the separation mechanisms of impinging-jet and surface separators which are believed to be responsible for the large differences in R_B values between the impinging-jet and surface separators. We now turn to discussion of the weak point of the impinging-jet separators which yielded the data of Figs. 27 and 28: their relatively very high values of R_B. Figure 30a presents a sketch of the surface separator of Fig. 3, and Fig. 30b presents a sketch of the arrangement of the impinging-jet separator furnishing the data of Figs. 27 and 28. In Fig. 30b, the knife-edge blocks are not shown and the nozzles are shown set θ=15 deg instead of 10 deg, but this is irrelevant to the present discussion. The first point to be discussed is a comparison of the separation action taking place in the separators of Figs. 30a and b. The specifications of the main separator surface in Fig. 30a are, proceeding downstream:

(1) The first 12 in. of the surface is flat and tilted at 10 deg to the flow direction at the nozzle exit.

(2) The next 17 in. of the surface has a radius of curvature of ~94 in.

(3) The last 5 in. of the surface (just upstream of the capture slot) has a radius of curvature of 11 in.

In two ways, the author believes that centrifugal force is important in allowing the surface separator to achieve much lower R_B values than the impinging-jet separator shown in Fig. 30b.

a. First centrifugal force effect. The concentrated liquid at, say, point A in Fig. 30a is moving along a curved surface and thus feels centrifugal force, which tends to separate the liquid from the gas, causing the former to become very concentrated near the surface. This force acts on the zone of concentrated liquid throughout its flow over the curved part of the separator surface. At a roughly corresponding point, A, in the impinging-jet separator, the liquid flux is concentrated by having passed through a "shock wave" (see Sections II.C.1, II.C.3, and II.D) but is not acted upon by centrifugal forces; rather, by rarefaction waves and diffusive tendencies (see Secs. II. C. 1 and II. C. 3) which tend to reduce the liquid flux. The maximum local ratio of liquid flux divided by that at the nozzle exit achievable in the early impinging-jet separators discussed in this section is 4.6 to 5.7, which compares well with a very simple theory (see Sec. II.D); the surface separator can greatly exceed these values. By narrowing the primary capture slot from the position giving the data of Figs. 27 and 28 and accepting a larger R_B value, the surface separator can easily achieve a mean liquid flux at the capture slot of over 10 times that at the nozzle exit.

b. Second centrifugal force effect. A second advantage of the surface separator sketched in Fig. 30a over the impinging-jet separator of Fig. 30b is due to the curvature of the separator channel (downstream of the first 12 in. of the separator). Consider a droplet at point B in Fig. 30a which is small enough so that the influences of aerodynamic forces on its motion are substantial (i.e., it has been deflected substantially from its initial direction of motion at the nozzle exit). It can readily be shown (one easy way is to replace the centrifugal term v^2/r by an equal "gravitational" force and to straighten out the channel) that such droplets will continue to move ("fall") towards surface A as long as the channel is curved. If the droplets are sufficiently small, they may not reach surface A in time to enter the primary capture slot, but the "falling" tendency is always there and aids in the overall collection of liquid by the primary capture slot. Contrast

the above to the case of a "small" droplet in a similar position B in the impinging-jet separator (Fig. 30b). If this droplet is not swept up by larger droplets (see Sec. I.E.3, discussion of Group 15), its asymptotic tendency is not to move towards the channel centerline, but rather to move parallel to the channel wall along path 1 and hence never to be collected in the zone of concentrated liquid. If one converts the separator of Fig. 30a to that of Fig. 30b, by straightening out the walls and adding a "gravity" force equal to v^2/r the motion of individual droplets relative to the channel walls (or centerline) in the former case can be illustrated in the latter separator. This leads to asymptotic paths of the droplets of the nature of path 1', which continue to move towards the concentrated zone of liquid (due to the "gravity" force). It should be noted that the sweeping up of smaller droplets by larger droplets (see Sec. I.E.3, discussion of Group 15) moving towards the zone of concentrated liquid occurs in both the surface and impinging-jet separators.

c. Noncentrifugal force effect present in surface separator and absent in impinging-jet separator. A third reason for the much greater concentration of liquid flux achievable in the surface separator of Fig. 30a compared to that achievable in the separator of Fig. 30b, not having to do with centrifugal force, is presented below. This effect was discovered by comparison of water flux profiles taken using mass flow probes in the separator of Fig. 30b with and without the presence of a metal plate along the channel centerline. The data taken with the plate in place showed the water flux in the central zone of the separator channel to be considerably more concentrated than under corresponding conditions without the plate in place. (A large reduction in jet velocity was noted with the plate in place, due to increased friction, but this is not the point under discussion at present.)

A specific example is the comparison of the mass flow probe profiles for $R_F \simeq 54.8$, $\theta = 10$ deg, taken at a distance of 7.2 in. from the nozzle exit. The maximum volume flux through the probe with a plate extending 5.12 in. downstream from the nozzle exit was 29.0 cm^3/s compared to 21.8 cm^3/s with no plate present, a ratio of 1.33. Further, the width of the profiles at mass flux values half those of the respective profile maxima was 0.34 in. with the plate compared to 0.485 in. without the plate.

A very simplified explanation for the effect of the plate is presented here. It ignores the details of the shock wave zone completely, but is felt

to contain the essential mechanism for the effect. This is that the wall reduces the lateral component of kinetic energy of droplets which hit it and rebound from it. In fact, there is probably a surface layer of water moving along the wall, but this would have the same effect on droplets rebounding from it. Reference 14 indicates that, for water droplets impacting nearly normally on a water surface and rebounding essentially intact, 95% of the droplet kinetic energy is lost during the impact. For the cases presented in Fig. 7, Ref. 14, the largest value of drop kinetic energy divided by drop surface energy was 2.8. For many cases of interest in the present problem, this number is undoubtedly much higher (as high as 100 to 1000) and the droplet would not rebound intact, but essentially blast a crater in the liquid film and "rebound" a series of secondary droplets. In this case, the author believes that the combined kinetic energy of the rebounding drops is substantially less than the energy of the impacting drop due to viscous dissipation. In most cases, regardless of the ratio of kinetic to surface energy of the impacting drop, we believe that a plate or a dense mass of liquid flowing along a plate makes the rebound kinetic energy of the droplets considerably less than that of the impacting droplet. Using this assumption, a very simplified picture of the shock zone with and without a center plate is drawn up. This is shown in Figs. 31a and 31b. The droplets (only the paths of droplets all traveling in a single plane are shown) leave the nozzle with exactly the same vector velocity and are equally spaced at the nozzle exit. All droplets are of the same size and all collisions are perfectly centered. All collisions are perfectly elastic except those with the center plate. The droplets remain in one plane. It can be shown that results of a similar nature (with respect to the effect of the center plate) are obtained with a complete range of droplet velocities within the shock as long as the droplets are considered as elastic spheres. For case (a) Fig. 31, either with no center plate or with a plate which gives perfectly elastic collisions, the density ratio across the shock is 2. This follows since the number of degrees of freedom of the droplets (normally ≈ 3, ignoring vibration, etc.) has been reduced to 1. One degree of freedom is lost since the droplets cannot move perpendicular to the paper (in this model). Loss of the second degree of freedom follows from the fact that in the assumed model the component of the velocity of the droplets parallel to the centerline cannot change and is always $= v \cos \theta$. The only degree of freedom remaining involves motion of the droplets in the

plane of the paper and perpendicular to the channel centerline. Hence, for the shock without dissipation (Fig. 31a), the Mach number of the flow upstream of the shock being infinity,

$$\frac{\rho_2}{\rho_1} = n + 1 = 2 \tag{8}$$

where n is the number of degrees of freedom. The case shown in Fig. 31b, where the perpendicular component of the rebound velocity from the plate is assumed to be half the impact velocity ($v_{r\perp} = 0.5v_{i\perp}$), is readily shown to yield (ρ_2/ρ_1)= 3. The results of the model of Fig. 31 (ρ_2/ρ_1 being higher with the plate and the width of the shock zone narrower) are believed to be quite relevant to the flow in surface separators as compared to impinging-jet separators, despite the great simplifications employed in constructing the model.

7. Some possible modifications of impinging-jet separators to make them more competitive with surface separators. Two possible modifications of impinging-jet separators which may make them yield cycle efficiencies comparable or superior to those of surface separators are as follows:

(1) The impinging-jet separator could be followed by a short surface separator to reduce R_B to values comparable to those obtainable with an all-surface separator (see discussion relevant to Figs. 27 and 28). However, the friction loss would be greatly reduced (due to the shortness of the friction surface) compared to that of the all-surface separator.

(2) If an auxiliary surface separator was mounted on either side of the primary capture slot of an impinging-jet separator, with $R_B \simeq 0.20$, and these separators were capable of returning the liquid to the nozzle inlet, a substantial gain in cycle efficiency could be obtained. The auxiliary separators are bound to have quite high friction losses since the mean ratio of liquid-to-gas flow through them is considerably lower than the average for the total flow. However, it may be possible to obtain sufficient pressure recovery to return the flow to the nozzle inlet.

H. Comparison of the Calculated Efficiencies of Li-Cs Cycles Using a Surface Separator or Impinging-Jet Separators Similar to Those Discussed in Detail Earlier in This Report

1. Introduction. In this section an estimate is made of the efficiency obtainable in a Li-Cs power cycle using an impinging-jet separator of the type whose performance was discussed in detail in Section II.G.

2. Description of the Li-Cs cycle calculations. In order to do this, use is made of calculations made for the efficiencies of a particular range of Li-Cs cycles as a function of z, R_A, and R_B of the separator (Ref. 15). The cycles studied were characterized by the following:

Fluids: Li-Cs.

Cycle is as sketched in Fig. 1.

Four nozzles (impingement is in two planes) are used.

Liquid mass flow at nozzle inlet = 351 lbm/s.

$R_F = 14.$

$T_{NI} = 1800°F.$

After the flow enters the diffuser upstream of the generator (see Fig. 1), the Cs vapor is assumed not to dissolve in the Li liquid. Account is taken of losses due to the presence of Cs vapor in the Li liquid downstream of the diffuser which is upstream of the generator such as:

(1) Poorer diffuser efficiency (see Ref. 13).

(2) Lower conductivity of fluid mixture in generator (see Refs. 1, 6 and 7).

3. Discussion of the accuracy of combining the Li-Cs cycle calculations with z, R_B and R_A data from H_2O-N_2 impinging-jet separators to estimate the performance of a Li-Cs cycle with an impinging-jet separator. The cycles studied have four nozzles with impingement in two planes; this is grossly dissimilar to the experimental geometry of the two-nozzle H_2O-N_2 separators discussed to date. At first sight, any efficiency estimation combining data from these two dissimilar geometries would appear to have little or no value. However, the Li-Cs cycle calculations do not, in fact, account in any important way for the (unknown) separator performance of a four-nozzle impinging-jet separator system; rather, assumed values of z,

R_A and R_B for the separator are employed. The flow reaching the capture slot is assumed to have the same aspect ratio as the overall aspect ratio at the nozzle exits. The only way in which the cycle program accounts for the difference between, say, a four-nozzle system and a two-nozzle (single-impingement) system with the same nozzle exit conditions area and overall (including all nozzles) aspect ratio is as follows. For the same overall aspect ratio at the nozzle exit, the four-nozzle and two-nozzle systems are assumed (the true performance of the four-nozzle system being unknown) to produce different aspect ratios at the primary capture slot. These differing aspect ratios produce slight changes in the performance of the diffusers and the generator. However, for the change from four-nozzle to two-nozzle operation, the effect of these changes on cycle efficiency is very small. Hence, the calculated efficiencies are taken to be applicable to a Li-Cs power cycle employing a two-nozzle impinging-jet separator similar to the H_2O-N_2 separators discussed in detail in earlier parts of this paper.

The problem arises now of dimensional similarity between the Li-Cs two-nozzle separators which would be used in the systems for which the efficiency was calculated (systems B) and the H_2O-N_2 separators for which z, R_B and R_A data is available. Fortunately, the nozzle exit conditions for "systems B" would be nearly identical to those of the Li-Cs nozzle separator system for which nondimensional separator parameters have been compared with those of the experimental H_2O-N_2 nozzle-separator systems in Section I. E. The only difference is that the mass flows in "systems B" are about twice those of the Li-Cs nozzle-separator system considered in Table 1, Sec. I.E. For geometric similarity of the nozzle exits, W for "systems B" must be $\sqrt{2}$ larger than the value used in Table 1 for the Li-Cs case. Further, it can be shown that, other parameters being the same, for geometrically similar nozzle cross-sections, the nozzle length should be nearly proportional to the square root of the mass flow, for the proper optimization of friction and slip losses (see Fig. 11, Ref. 9). By analysis of the ratio of aerodynamic drag stresses and the surface tension strength of a droplet, it can be shown that, other things being equal, D (the maximum droplet size expected at the nozzle exit) is proportional to (nozzle length)$^{1/2}$. Hence, D for "systems B" would be $\sqrt[4]{2}$ times the value used in the Li-Cs data of Table 1, Sec. I. E. All other variables for the Li-Cs

case in this table would be almost identical to those for "systems B." Examining this table, and considering the first 10 groups to be the fundamental groups, it can be seen that for "systems B" Group 3 (W/D) will be increased by a factor of $\sqrt[4]{2} = 1.19$, and Group 8 will be decreased by the same factor compared to the values given for the Li-Cs case of the table. All other groups (from 1 to 10) for "systems B" would be nearly identical (within, typically, 5%) to those given for the Li-Cs case of Table 1. In Section I. E, it is shown that the Li-Cs case of Table 1 is reasonably well (although not exactly) simulated by the experimental H_2O-N_2 nozzle separator systems. From the above arguments, the author believes that one can obtain rough estimates of the variation of efficiency of "systems B," with R_A, the primary capture slot being located at the x position which minimizes R_B (and using a two-nozzle impinging-jet separator), by inserting the appropriate R_B and z values from the H_2O-N_2 tests of the separators discussed at length earlier in the paper.

4. Estimation of Li-Cs cycle efficiencies using impinging-jet separators similar to those discussed at length earlier in this report. In Sec. I. E, it is shown that the best matching of the Li-Cs nondimensional groups given in Table 1 for an impinging-jet separator, by the corresponding H_2O-N_2 data, occurs for R_F (H_2O-N_2) = 19.1 and 37.5. Experimental values for z, R_B and R_A from an H_2O-N_2 separator operating at $R_F \simeq 26.3$, θ = 10 deg, and with the knife edges located at the point giving the minimum R_B, are inserted into the above-mentioned calculations for the efficiency of a Li-Cs cycle, yielding the data of Fig. 32. The abscissa is R_A, corresponding to different values of the G of the H_2O-N_2 tests. The lower line is calculated assuming that the liquid flow bypassing the main capture slot is separated from the gas (by surface separators, etc.) with complete loss of its kinetic energy and is mixed with the jet from the primary capture slot with an attendant substantial loss of kinetic energy (momentum is assumed to be conserved). The mixing is assumed to occur before the jet enters the (upstream diffuser)-(generator)-(downstream diffuser) chain of apparatus. The higher line is calculated assuming that the flow bypassing the primary capture slot can be separated from the gas (presumably by surface separators) and passed through a diffuser achieving sufficient pressure recovery to be reinjected at the nozzle inlet (see discussion in Sec. II.G.7).

It is noted that the negative efficiencies shown in Fig. 32 are not imaginary but represent cases where power must be fed into the generator (making it act like a pump) in order that the cycle can be closed.

a. Case where the liquid bypassing the primary capture slot is returned, with a total loss of kinetic energy, to the main jet. When the liquid bypassing the primary capture slot is assumed to be returned to the upstream diffuser inlet with total loss of kinetic energy, the efficiency of the system cannot even be made positive, the maximum value being -0.033. Both the upper and lower curves have maxima near the $R_A = 6$ point; further increases in R_A result in such large increases in R_B that the efficiency is lowered. This can be shown by extension of the knife edge H_2O-N_2 separator data (yielding the 3 points per curve shown in Fig. 32) by probe profile data such as that shown in Fig. 9. In the low-R_A sections of the curve, the total velocity loss $y = 1 - (1 - z)(1 - R_B)$ is not too large (0.20 to 0.25), but since R_A is relatively small, r_a in the diffusers and generator will be relatively large, making the performances of these components very poor (see Sec. II.H.2). On the other hand, at the higher R_A end of the curve, r_a is reduced sufficiently in the diffusers and generators to allow reasonable performance of said components from the point of view of diffuser efficiency and conductivity in the generator. However, the velocity of the jet at the entrance to the upstream diffuser has been so greatly reduced by mixing with the (assumed) zero velocity bypass liquid flow (which is 0.3 to 0.35 of the total nozzle liquid flow for these values of R_A) that the (mixed) jet kinetic energy per unit mass is insufficient to generate power and to be diffused back to a pressure sufficiently high to allow circulation through the system. Under the assumption of total loss of the kinetic energy of the liquid bypassing the primary capture slot, then, the H_2O-N_2 separator studied experimentally (with no modifications) obviously offers totally unsatisfactory performance in Li-Cs power cycle.

b. Case where the liquid bypassing the primary capture slot can be returned to the nozzle inlet (without pumping). Turning to the upper curve of Fig. 32, if it is assumed that the flow bypassing the primary capture slot can, by (presumably) surface separation and diffusion be returned to the nozzle inlet, efficiencies up to .038 can be obtained. This is a

remarkably high performance, in view of the very poor performance calculated for the system using the assumption of the previous section.

c. Recommendation for future experimental investigation of the pressure recovery obtainable from the flow bypassing the main capture slot. Based on the great difference between the upper and lower curves in Fig. 32, the author believes that in future experimental work a high priority should be assigned to the experimental investigation of the pressure recovery obtainable from the flow bypassing the primary capture slot of an impinging-jet separator. Even if only enough pressure is recovered to inject the bypass liquid into the nozzle at, say, a pressure halfway between that at the inlet and outlet, a substantial gain in performance could be obtained over the case represented by the lower curve in Fig. 32.

5. Comparison of the calculated performances of Li-Cs cycles with surface separators or impinging-jet separators of the type discussed in detail here. An examination of the data of Ref. 16, Fig. 16 shows that for a Li-Cs surface separator cycle with maximum cycle temperature of 1800°F, the efficiency is calculated to be 0.075. The liquid mass flow in the cycles considered in Ref. 16 is of the order of several hundred lbm/s (see p. 23, Ref. 16), similar to that in "systems B." The maximum cycle temperature in "systems B" is $\simeq$ 1800°F. Hence, the results of the surface-separator cycle efficiency calculations of Ref. 16 and the impinging-jet cycle efficiency calculations made in Sec. II.H.1-4 should be comparable. Even with the liquid bypassing the capture slot in the impinging-jet cycle being returned to the nozzle inlet, the efficiency is still only about half that calculated for a comparable surface-separator system. It should be noted that at $R_A = 5.85$, upper curve, Fig. 32, for which η was calculated as 0.038, $R_B = 0.35$. Hence, based on the fluid entering the primary capture slot only, the cycle efficiency could be calculated as $0.038/(1 - 0.35) = 0.058$. However, in fact, 35% of the liquid just circulates around from the nozzle to secondary separators, to diffusers, and back to the nozzle inlet. This recycling liquid, however, requires just as much energy per unit mass to be accelerated in the nozzle by the Cs vapor as that entering the primary capture slot. Hence, the amount of Cs flowing in the cycle and the heat required from the source are about $1 + 0.35/(1 - 0.35) = 1.538$ times that which would be required if there were no bypass liquid, but the same

amount of liquid entered the primary capture slot. This, then, reduces the overall cycle efficiency from 0.058 to 0.058/1.538 = 0.038.

Summing up, incorporating the impinging-jet separators discussed up to this point in a Li-Cs system, even assuming that the liquid flow bypassing the primary capture slot could be returned (without pumping) to the nozzle inlet, would yield efficiencies apparently about half those of a comparable surface separator system. If the liquid flow bypassing the primary capture slot in these impinging-jet systems must be returned to the main jet with a total loss of kinetic energy, a positive power output cannot even be achieved with the impinging-jet system. However, the above conclusions only apply if one uses the particular impinging-jet separator geometry which has been the main topic of discussion in the paper up to this point in a Li-Cs cycle.

6. Modifications of the impinging-jet separator which could lead to performances higher than those used in the discussion and comparisons of Section II.H.1-5. Several modifications of the impinging-jet separator geometry have been made which have yielded considerably higher calculated Li-Cs cycle efficiencies (see Secs. IV.A and B). Further, other separator designs have been identified (see Secs. IV.D, V.A, and V.B) which could yield further improvements, possibly up to the point where the calculated efficiency for an impinging-jet Li-Cs system exceeds that of a comparable surface separator system. The author believes the latter to be a definite possibility. One configuration is that in which four nozzles are used (impingement taking place in two planes instead of one); this is the configuration assumed in the Li-Cs cycle efficiency calculations used extensively in this section (Sec. II.H). This configuration is believed by the author to have the potential for the achievement of substantially increased values of R_A with relatively little increase in z or R_B. This is because any element of the liquid flow will pass through two successive shock zones instead of one, the latter being the case for the two-nozzle impinging-jet separator. If this improvement of R_A is realized, cycle efficiencies considerably higher than 0.038 would be expected if the four-nozzle separator system were to be incorporated into a Li-Cs cycle.

I. Tendency, in the Impinging-Jet Separators Studied in Section II.A-G, for the Minima of P_{NE}, R_B and z to Occur at the Same x-Position (for Given Values of θ, R_F and G).

Data was obtained only for $\theta = 10$ and 15 deg. At each θ value, four values of G and four values of R_F were tested (see Sec. II.B). For each value of θ, G and R_F, measurements were taken at about four different x-positions spaced at intervals of 1 to 2 in. in the neighborhood of the geometric impingement point (x_{GI}, see Fig. 6, Sec. II.B). For each value of θ, then, there were 16 opportunities (4 R_F values $\times$ 4 G values) to determine the x-positions of the minima of P_{NE}, R_B and z. For $\theta = 15$ deg, seven of the 16 sets of data showed the minima occurring at the same x-position. Seven more of the 16 sets of data had two of the three variables (P_{NE}, R_B and z) with minima at the same x-position, with the minima of the third variable quite close to this position. The x-positions for the minima of the three variables do not agree as well for $\theta = 10$ deg, but a significant tendency for them to occur at the same x-position is still present. It is pointed out that only one set of measurements was taken at any set of values of θ, R_F, G and x; also, the data indicate that considerable scatter is present.

A very tentative theory for this phenomenon is advanced by the author and follows. It is well established (see Figs. 7 and 9, Sec. II.C.1) that R_B has a definite minimum at a certain x-position (for given values of θ, G, and R_F). As one moves the x-position of the knife-edge tips away from this minimum in either direction, the proportion of water in the bypass flow increases, thus more heavily loading with liquid the gas which escapes to either side of the main capture slot. Since R_F values range from ~14 to ~85, even a relatively small increase in R_B (say, 0.04) significantly increases the total mass flow (liquid plus gas) which bypasses the main capture slot. The author believes that this increase in total mass flow may increase the pressure drop through the "gas" escape system (see Fig. 5, Sec. II.A and Fig. 24, Sec. II.F.2.b) and, hence, P_{NE}. This increase in P_{NE} would then account for the increase in z (see Sec. II.F.2.b, where the variation of V_{jet} with P_{NE} is discussed in detail). This tentative theory qualitatively fits all of the available data for $\theta = 10$ and 15 deg fairly well, except for the data for $\theta = 10$ deg and G = 0.5 in. In this case, the minimum values of R_B and z definitely occur at an x-position where P_{NE} is significantly higher than its minimum value. Hence, the theory presented does

not describe the variation of $P_{NE'}$, R_B and z with x-position for this case, and some other phenomena must be looked for. However, the author does feel that the theory presented above may contribute somewhat to the understanding of the variation of $P_{NE'}$, R_B and z with x-position.

Additional data points taken with $\theta = 10$ and 15 deg, as well as at $\theta = 20$ and 30 deg would help to confirm (or disprove) the hypothesis that, under many conditions, there is a definite tendency for the minima of $P_{NE'}$, R_B and z to occur at the same or nearly the same x-position (for a given set of values of R_F, G and θ). Such investigations would also probably shed light on whatever phenomena are responsible for the differing x-positions of the minima of $P_{NE'}$, R_B and z observed for the case with $\theta = 10$ deg, G = 0.5 in. Such differences may also occur for other values of θ, G and R_F not investigated.

III. SOME THEORETICAL CONSIDERATIONS

A. Two Aerodynamic Effects Important in the Outer "Boundary Zones" of the Nozzle Jets in the Separator Channel

1. Estimation of the maximum distance which a droplet of a given size can move in the direction perpendicular to the separator channel centerline. The problem of the movement of droplets laterally across the separator channel towards the centerline is referred to briefly in various contexts in the following sections:

I.E.3
II.C.1
II.C.2
II.C.4, paragraph (2)
II.G.6.b

In Section I.E.3, it is stated that for the restricted case of C_D = constant, and considering only the largest droplets to be expected at the nozzle exit, the effectiveness of these (largest) droplets in crossing the separator channel to enter the zone of concentrated liquid near the channel center is controlled to a large extent by the magnitude of "Group 14" ($W\rho_g/D\rho_\ell$).

In this section, the problem will be considered in more detail; the variation of C_D will (approximately) be accounted for, etc. The assumptions made are as follows:

(1) The droplet starts its motion in the separator channel with the velocity it had at the nozzle exit – this is almost more by definition than by assumption.

(2) The gas turns instantly at the nozzle exit to move parallel to the channel walls. In reality, the gas cannot turn instantly, but the relatively small pressure differences between the centerline and wall of the separator channel (see, for example, Fig. 25, Sec. II.F.2.b) indicate that the gas does turn very rapidly (perhaps within 0.5 in. from the nozzle exit) to move essentially parallel to the channel walls. Further, calculations made from measurements of the lateral pressure gradients across the channel 2 in. downstream from the nozzle exit indicate that such pressure gradients could turn the gas to move parallel to the channel centerline in a small fraction of an inch, despite the effect of the droplets tending to drag the gas towards the channel centerline.

(3) The components of the gas and liquid velocity parallel to the channel centerline are assumed equal. Calculations by the method of Ref. 9 indicate that the gas should be moving at, typically, 1.4 times the liquid velocity at the nozzle exit. However, (1) the area of the separator channel is about 1.2 times that of the nozzle exits, and (2) the pressures in the separator channel are typically of the order of 2 psig, whereas the nozzle exit pressure assumed in the above-mentioned reference is 0 psig (14.2 psia). Based on these two facts, the author believes assumption (3) to approximate the true conditions.

(4) The drag force will be taken as that for a single sphere moving through an infinite medium. The validity of this assumption depends on r_a; outside of the zone of concentrated liquid near the channel centerline r_a values are greater than 7 and usually greater than 15. The discussions of Ref. 17, p. 42-113 and

Ref. 18, show the drag force to be within a factor of 2 of the isolated sphere value for r_a greater than 7.

(5) C_D for the droplets is approximated as $0.5 + 24\mu_g/\rho_g uD$; this in itself is an approximation of the value for spheres. However, a more accurate representation of the value of C_D for spheres was believed not to be worthwhile, since the C_D values for droplets were found by various authors to differ from those for spheres by factors up to ~4; also, there was considerable disagreement among C_D values measured for droplets by different experimenters (see Ref. 9, Fig. 2).

With these assumptions, the lateral distance a droplet could move across the gas stream for a given reduction in lateral velocity could readily be calculated to be

$$y\left(\frac{v}{v_0} = \eta\right) = \frac{8}{3}\frac{\rho_\ell}{\rho_g} D \ln \frac{1 + \frac{\rho_g D v_0}{48\mu_g}}{1 + \eta \frac{\rho_g D v_0}{48\mu_g}} \tag{9}$$

where v_0 is the original component of the liquid velocity perpendicular to the channel centerline and v is the same component after the droplet has moved a distance perpendicular to the channel centerline equal to y.

The above equation will be recast in the form of a rough criterion for good separator performance to illustrate the use of the nondimensional parameters presented in Sec. I.E. It is assumed that one criterion for satisfactory operation of the separator is that the largest-diameter droplets expected to occur at the nozzle exit starting from the outermost edge of the nozzle can reach the channel centerline with $v \approx 1/\sqrt{2}\, v_0$. The "correct" value of v/v_0 required at the channel centerline is not known, but the author believes $1/\sqrt{2}$ to be a reasonable estimate. Possibly, a more serious failing of the above criterion is the consideration of only droplets of the largest diameter expected at the nozzle exit, while, in fact, a wide range of droplet sizes is believed to exist at the nozzle exit (see Ref. 11). However, corrections for these failings of our one simple criterion for the "satisfactory operation of the separator" would involve, at least approximately, only the

insertion of certain numerical factors into the criterion; the basic form of the latter would be unaltered. Our simple criterion is, then, that

$$y\left(\frac{v}{v_0} = \frac{1}{\sqrt{2}}\right) = \frac{W}{\sqrt{2}}, \tag{10}$$

where W is the channel width (see Fig. 4, Sec. I.E.1).

We replace v_0 by $V_\ell \sin\alpha$ so that the variables of the recast form of Eq. (11) are the same as those used in Sec. I.E. (Refer to said section with respect to the replacement of v_0 by $V_\ell \sin\alpha$.) Substituting Eq. (10) in Eq. (9), setting $\eta = 1/\sqrt{2}$, and replacing v_0 by $V_\ell \sin\alpha$ yields the following as one (crude) criterion for satisfactory separator performance

$$1 \leq \frac{16}{3}\frac{\rho_\ell}{\rho_g}\frac{D}{W}\ln\left(\frac{1 + \frac{\rho_g D V_\ell}{48\mu_g}\sin\alpha}{1 + \frac{\rho_g D V_\ell}{68.0\mu_g}\sin\alpha}\right) \tag{11}$$

Referring to nondimensional Groups 1, 2, etc., presented in Sec. I.E as G_1, G_2, etc., Eq. (11) can be rewritten as

$$1 \leq \frac{16}{3}\frac{1}{G_{14}}\ln\left(\frac{1 + \frac{G_{13}}{48}\sin G_1}{1 + \frac{G_{13}}{68.0}\sin G_1}\right) \tag{12}$$

As long as only the largest droplets expected at the nozzle exit are considered (as in Eq. 12 and in the discussion of Group 14 in Sec. I.E) and the value for v/v_0 is kept constant (in this case at a value of $1/\sqrt{2}$), the criterion is largely controlled by the $\rho_g W/\rho_\ell D$ group. The $\rho_g D V_1/\mu_g$ ($= G_{13}$) varies only slightly over a wide range of R_f values for the same liquid-gas combination; further, as can be seen in Table 1, Sec. I.E., the change in this group is only by a factor of ~2 in changing from H_2O-N_2 to Li-Cs. G_1 could be changed from 5 to 30 deg or even over a broader range; however, it is known that the optimum impinging-jet separator performance occurs for $\alpha(= G_1) = 10$ - 15 deg, and hence for high-performance separators the

changes in G_1 would be relatively small. Since both $\rho_g DV_1/\mu_g$ and G_1 occur in the logarithm, it follows, as stated previously, that the criterion is determined mainly by the $\rho_g W/\rho_\ell D$ group.

However, returning to Eq. (9), if η is changed or droplets of sizes considerably smaller than the maximum size expected to exist at the nozzle exit are considered, then the terms within the logarithm may become so close to unity that changes in their values affect the value of y almost as strongly as changes in the term outside the logarithm. This can best be illustrated by considering the two limiting cases. If $\rho_g Dv_0/48\mu_g \gg 1$, Eq. (9) simplifies to

$$y\left(\frac{v}{v_0} = \eta\right) = \frac{8}{3}\frac{\rho_\ell}{\rho_g} D \ln\frac{1}{\eta}, \tag{13}$$

and the dependence on $\rho_g Dv_0/\mu_g$ has disappeared. Eq. (13) is the correct simplification if η is appreciable compared to unity, say, greater than 0.5 (which likely includes most cases of interest for good separator design). However, as η becomes smaller and smaller, Eq. (13) becomes less accurate, and for the limiting values $\eta = 0$, the proper simplification is

$$y\left(\frac{v}{v_0} = 0\right) = \frac{8}{3}\frac{\rho_\ell}{\rho_g} D \ln\left(\frac{\rho_g Dv_0}{48\mu_g}\right), \tag{14}$$

where a dependence on $\rho_g Dv_0/\mu_g$ is retained, though only in the logarithm. On the other hand, if $\rho_g Dv_0/48\mu_g \ll 1$, Eq. (9) simplifies to

$$y\left(\frac{v}{v_0} = \eta\right) = \frac{8}{3}\frac{\rho_\ell}{\rho_g} D \frac{\rho_g Dv_0}{48\mu_g}(1-\eta), \tag{15}$$

and the dependence on $\rho_g Dv_0/\mu_g$ is just as strong as those on $\rho_\ell/\mu_g D$.

For a particular nozzle exit condition, calculated by the methods of Ref. 9, for H_2O-N_2, $R_F = 37.5$, and $\alpha = 15$ deg, calculations of y from Eq. (9) were made for various droplet diameters and for $\eta = 0$ and $\eta = 1/\sqrt{2}$. For this calculation, the fluids entered the nozzle at 520°R and the pressure in the separator channel was taken to be the nozzle exit pressure of the

calculations, 14.2 psia. For this case, v_0 was taken as the calculated liquid velocity multiplied by sin 15 deg, the value being $v_0 = 78.5$ ft/s. The results of these calculations are shown in Table 2.

Two points of importance should be noted from Table 2. First, the lateral distance at which the droplets have lost half their kinetic energy is much less than the distance to which they would ultimately travel (by factors ranging from 7 for the 0.01-in.-diameter droplet to ~3.3 for the 0.0001-in.-diameter droplet). This is extremely important in impinging-jet separator design. The large value of y for v/v_0 close to zero is only achieved after a (relatively) very long period of time, thus requiring a separator channel of length so great that the friction losses would be very severe. Perhaps more important is the fact that large reductions in v before impact of the jet on the central zone of concentrated liquid reduce the momentum per unit area perpendicular to the channel centerline with which the jet finally impacts the central zone of concentrated liquid. As stated in Secs. II.C.1 and 3, this lower momentum per unit area is believed by the author to be likely to both propagate rarefactions into the zone of concentrated liquid and to be less able to withstand the tendency of this central zone to diffuse outwards.

Thus, for the case of Table 2, considering the 0.01-in.-diameter droplets only, the author would not consider a separator channel halfwidth of, say, 25 in. likely to give good results, even though y ($v/v_0 = 0$) = 52.9 in. Rather, the author believes that a halfwidth of 7 or less inches would be required in order for good results to be obtained (with respect to this criterion only).

Second, if the designer is using a program of the type described in Ref. 9 to design the nozzle(s) for a separator, the program output gives only the largest size of droplet to be expected at the nozzle exit. For the cases presented in Ref. 11, 50% of the liquid mass flow at the nozzle exit was found to consist of droplets of sizes less than 0.42 times that of the maximum droplet size found. This wide spectrum of droplet sizes together with the very rapid falloff of both y values of Table 2 with decreasing D means that, using Eq. (9) to select a suitable separator channel halfwidth, the latter would probably have to be considerably narrower than that based on a D value taken from a program of the type described in Ref. 9. However, the factor by which the separator channel halfwidth would have to be reduced

would depend on the droplet size distribution for the particular nozzle under consideration (which may not be the same as those for the cases discussed in Ref. 11).

From the above discussion, particularly the many assumptions made in deriving Eq. (9), it is apparent that one should not blindly use said equation for separator channel design. However, the author believes that careful use of this equation could be helpful in both the design of impinging-jet separators and the understanding of phenomena observed in such separators.

2. Estimation of the amount of liquid which escapes from the nozzle jets at their outer boundary zones due to the tendency of the smaller droplets to turn and move parallel to the channel centerline. This topic is mentioned briefly in Secs. I. E. 3 (in the discussion of Group 15) and II. G. 6. b; here, it is discussed in more detail. An estimate is made of the mean free path for a small droplet escaping from the outer boundary zone of the nozzle jets. The liquid which escapes from the outer boundary of the nozzle jets as small droplets then moves nearly parallel to the channel centerline, and most of this liquid cannot be captured in the primary capture slot of a pure impinging-jet separator (for any reasonable slot width). Assuming the shape of the droplet distribution curves given in Ref. 11 to apply at the exits of the nozzles used in impinging-jet separators, a rough estimate of the mean free path for a small droplet escaping from the outer boundary zone can be made. It is assumed that half of the liquid mass flow is made up of "large" droplets of diameter calculated by the methods of Ref. 9. From the droplet distribution curves of Ref. 11, and from the fact that the resulting value calculated for the "small" droplet mean free path (λ) depends on the "large" droplet diameter only to the first power, this assumption appears reasonable as a first approximation. On this basis the mean free path can readily be calculated as

$$\lambda = \frac{4D\,(r_a + 1)}{3} \tag{16}$$

If consideration is to be taken that the mass fraction of liquid flow considered to be contained in "large" droplets is not 0.5 but f_ℓ, Eq. (16) can be modified as follows.

$$\lambda = \frac{2D\,(r_a + 1)}{3f_\ell} \tag{17}$$

An important ratio is that of λ to the separator channel halfwidth $W/2$, given by

$$\frac{2\lambda}{W} = \frac{4}{3}\frac{D}{W}\,\frac{(r_a + 1)}{f_\ell}\,, \tag{18}$$

using Eq. (17) for λ.

If the following assumptions are made, an estimate of the fraction of the total liquid mass flow escaping from the outer boundary zone of the nozzle jets through the above discussed mechanism can be obtained.

(1) The fraction of the total liquid flow escaping must be small, say, less than 0.2.

(2) The "small" droplets which encounter "large" droplets as they are "trying to escape" are assumed to be swept up by the "large" droplets and carried along with the latter. This is a great simplification of what probably occurs in fact; errors caused by this assumption will be discussed subsequently.

Under these assumptions, an estimate of the fraction of the liquid mass flow which escapes from the outer boundary zone of the nozzle jet (F_L) is given by

$$F_L = (1 - f_\ell)\,\frac{2\lambda}{W} = \frac{4D}{3W}\,(r_a + 1)\,\frac{(1 - f_\ell)}{f_\ell}. \tag{19}$$

If it is assumed that $(1 - f_\ell)/f_\ell \approx 1$ (which assumption will be discussed subsequently), Eq. (19) can be simplified to

$$F_L \simeq \frac{4}{3}\frac{D}{W}\,(r_a + 1) \tag{20}$$

with the further (reasonably accurate) approximations that, at the nozzle exit, $u_\ell \approx u_g$, and $r_a + 1 \approx r_a$, Eq. (20) can be cast in a form showing F_L

determined by Group 15 (G_{15}), Sec. I.E. With these further approximations, Eq. (20) becomes

$$F_L \approx \frac{4}{3}\frac{D}{W}\frac{\rho_\ell}{\rho_g}\frac{m_g}{m_\ell} = \frac{4}{3}\frac{1}{G_{15}}, \tag{21}$$

showing the importance of Group 15 in controlling the fraction of liquid lost. A simpler recasting of Eq. (20) in terms of the nondimensional groups of Sec. I.E., obviating the need for Group 15, is:

$$F_L \approx \frac{4}{3}\frac{1}{G_3 G_{10}} \tag{22}$$

This expression for F_L eliminates the need for the approximations that, at the nozzle exit, $u_\ell \approx u_g$, and $r_a + 1 \approx r_a$.

Considering the many assumptions made, the agreement between values predicted by Eq. (22), taking D as the maximum expected value of the droplet diameter at the nozzle exit, and experimentally measured values is remarkable. From Fig. 10, Sec. II.C.3 (data taken at $\theta = 10$ deg), the probe mass flow appears to level out fairly well for $y > 0.75$ in. Hence, experimental R_B data taken with $G = 1.5$ in. $= 2 \times 0.75$ in., $\theta = 10$ deg, and with the knife edges located at the x-position which gave minimum R_B, was compared with F_L values calculated from Eq. (22). It is noted that θ does not occur in Eqs. (16)-(22). The experimental values of R_B ranged from ~0.07 to ~0.10, depending on R_F. The calculated values of F_L ranged from ~0.03 to ~0.06 for the same range of R_F. This agreement is felt to be very satisfactory, considering the crudeness of the theory, and lends considerable support to the latter.

Several important factors that may cause Eqs. (16)-(22) to be inaccurate are now discussed. First, the division of the liquid flow into "large" and "small" droplets is a very coarse way of handling the wide spectrum of droplet sizes expected at the nozzle exit (assuming that a spectrum of sizes similar in shape to those presented in Ref. 11 applies to the nozzles of the impinging-jet separator). Making this assumption, the division of droplets

into "large" and "small" groups could be done on the basis of their estimated trajectories (calculated using Eq. (9), Sec. III.A.1).

This division would seem very difficult to make at first sight; however, the very rapid decrease of the y values of Table 2 (Sec. III.A.1) with decreasing D would indicate that a reasonable estimate of the critical value of D (D_c, separating the "large" and "small" droplet regions) is possible. To estimate D_c, the halfwidth of the separator channel (W/2) must be known, since the estimation of D_c essentially involves the comparison of y values calculated in the same way as those presented in Table 2, Sec. III.A.1, with W/2.

Once D_c is estimated, one can calculate f_ℓ readily, and further, by proper averaging, a value for D in Eqs. (16)-(20) more suitable than that obtained from the methods of Ref. 9 can be obtained. If the spectra of droplet sizes at the nozzle exits of the nozzles used in the impinging-jet separators differ substantially in shape from those presented in Ref. 11, the above calculations cannot be made, until droplet size spectra at the separator nozzle exits are available. In this case, only crude estimates can be made for f_ℓ and the best value of D to use in Eqs. (16)-(20).

Secondly, it was assumed that any "small" droplet colliding with a "large" droplet will be picked up and carried away by the latter. This is equivalent to assuming that all such collisions will be "collisions with coalescence" (as they are referred to in Ref. 12). The same reference makes it clear that "collisions with coalescence" take place only over a rather restricted range of the ratio of the kinetic energy of the droplets (in their center of mass system) to the surface energy of the droplets. At relatively high velocities, the droplets are liable to disrupt instead of coalesce. The author suggests that a "small" droplet may well have to undergo several collisions with "large" droplets before the energy conditions are right for coalescence. It should be pointed out that the above statement is somewhat of a simplification, since if a "small" droplet collides with a "large" droplet at a relatively high center-of-mass kinetic energy the "small" droplet will not retain its identity; rather several (or many) small droplets would be ejected from the large droplet. This process may be partly responsible for the fact that the measured values of R_B tended to be about twice the calculated rates for F_L. Further, the "proper" D value for the estimation of F_L

in Eqs. (16)-(20) may well be of the order of half the value used (taken from calculations of the type presented in Ref. 9). This appears quite possible if the droplet size spectra at the nozzle exits in the separators are of the same shape as those presented in Ref. 11. If so, the disagreement between recalculated values of F_L (based on this smaller droplet diameter) and the measured value of R_B for the cases discussed above would be by a factor of ~4, and may lend weight to the proposal of the author that considerable disruption occurs on the impact of "small" and "large" droplets before some of the former coalesce with the "large" droplets. The greater the frequency of disruption relative to that of coalescence, the more R_B would be expected to diverge from the value of F_L calculated from the simple theory given above.

A great deal of investigation is required into (1) the spectrum of droplet sizes at the impinging-jet separator nozzle exit and (2) the question of the relative frequencies of "coalescence" and "disruption" collisions in the outer edge of the nozzle jet. The latter problem is rendered exceedingly complicated by the wide spectrum of droplet sizes expected at the nozzle exit.

Despite the uncertainties and approximations the author believes that Eqs. (19) to (22) can be of use both in the design of impinging-jet separators and in the interpretation of phenomena observed in these devices.

B. Nozzle Divergence

The problem of the reduction of impinging-jet separator performance due to divergence of the nozzles at the exit (see Fig. 8, Sec. II.C.1) has been mentioned briefly in Sections II.C.1; II.C.3 and II.C.4, paragraph 1; here the problem will be discussed in more detail.

The model used is as follows (see also Fig. 33):

(1) The nozzles have a shape (for an appreciable distance upstream from the nozzle exit) which is made up of 2 parallel walls and 2 walls each diverging from the nozzle centerline at an angle γ (see Fig. 33). For the nozzles used in the impinging-jet separators discussed extensively in Sec. II, the last 6.4 in. of 25-in.-long nozzles conform to this shape.

(2) The nozzle angle is θ (as used previously in this report).

(3) The nozzle walls are assumed to be of zero thickness.

(4) The nozzle exit is a rectangle with the dimension between the diverging walls being A_1 and that between the parallel walls, B_1.

(5) The flow at the nozzle exit is assumed to be uniform except as one moves across the exit parallel to the parallel nozzle walls; the angle of direction of the flow changes as if the flow originated from the point where the flat part of the diverging nozzle walls extended would meet (point A, Fig. 33). Considerably upstream of the nozzle exit, the diverging nozzle walls start curving, eventually becoming parallel at the throat. However, assumption (5) should be quite accurate if, first, the flat portion of the diverging nozzle walls extends a substantial distance upstream from the nozzle exit (as in the case quoted in paragraph (1) where the flat-diverging-wall portion of the nozzle makes up $6.4/25 \simeq 0.26$ of the total length of the nozzle). Secondly, if the divergence angle becomes too great, the curved portion of the diverging walls may have so great a curvature that the liquid droplets cannot follow the surface and the gas. In this case, assumption (5) would fail; for the cases used as examples, the divergence is believed to be sufficiently small that the assumption holds to a good approximation.

(6) Aerodynamic forces are totally neglected in the separator channel. This is, as much data in Section II and the discussions of Section III.A show, very far from the truth; however, the intent of Section III.B is to isolate and study the nozzle divergence effect separately. Hence, this assumption.

(7) The fact that the component of jet velocity perpendicular to the channel centerline is slightly less at points D_2 (Fig. 33b) than at point D_1 will be neglected. The factor between the velocity component used in the following calculations (that evaluated at point D_1) and the true mean value calculated along the line D_2-D_1-D_2 (Fig. 33b) can be shown to be given by $\sin\gamma/\gamma \simeq 1 - \gamma^2/6$. For the largest value of γ considered, 5.1 deg, this factor is 0.9987. Hence, the author believes this assumption to be well justified for the following calculations. The following formulae are for the ratios of the various quantities referred to

at points B (the farthest point downstream at which the jet strikes the centerline) to those at points C (center of the nozzle exit). The thickness of the central zone of concentrated liquid is ignored. If there were no nozzle divergence, all the following ratios would be unity: R_ρ, R_m and R_v (respectively, the ratios of liquid densities, liquid momentum fluxes per unit area perpendicular to the channel centerline, and components of the liquid velocities perpendicular to the channel centerline). Subscript 1 refers to the configuration of Fig. 33a and subscript 2 to that of Fig. 33b.

$$R_{\rho 1} = \frac{\sin(\theta - \gamma)}{\sin(\theta + \gamma)} \tag{23}$$

$$R_{v1} = \frac{\tan(\theta - \gamma)}{\tan\theta} \tag{24}$$

$$R_{m1} = R_{\rho 1}(R_{v1})^2 \tag{25}$$

$$R_{\rho 2} = \frac{1}{1 + 2A_R \frac{\sin\gamma}{\tan\theta}} \tag{26}$$

with

$$A_R = B_1/A_1 \tag{27}$$

$$R_{v2} = 1 \tag{28}$$

$$R_{m2} = R_{\rho 2} \tag{29}$$

Clearly, if two cases are compared and if all 3 R's are greater for, say, the first case, then, ignoring all other factors, this case should provide the better separator performance. However, since the theory for the "shock wave" or "shock zone" near the channel centerline through which the liquid density rises rapidly is very poorly understood, the author cannot say which

of the three R values are the most important. If one is comparing two cases where some of the R values are greater for one case and some for the other (say, by comparable factors), the choice becomes very difficult (if based on the R values only).

The six R values (both R_1 and R_2 values) will be calculated and compared for three cases; two cases involve the nozzles used in the impinging-jet separator experiments described in Sec. II; for these nozzles B_1 = 5.56 in., A_1 = 1.586 in. and Υ = 2.72 deg. Hence, A_R = 5.56/1.586 = 3.51. Two different values of θ are considered, 10 and 15 deg; these will be referred to as cases 1 and 2 respectively. For the third case, nozzles having a square exit with an exit area equal to that of the above-mentioned nozzles are considered. Also, the rate of change of area with length just upstream of the nozzle exit is made the same as that for the nozzles of cases 1 and 2. This assumption leads to a Υ value of 5.10 deg; A_R, is, of course, unity. The R values will be calculated for these nozzles for θ = 15 deg. This last case will be referred to as case 3. The calculated R values are presented in Table 3.

Case 3 is studied first. For this case, all of the R_{x2} values are larger than the corresponding R_{x1} values (x = ρ, v or m). Hence, based on the criterion of the R values only, the configuration of Fig. 33b should provide superior separator performance. For both cases 1 and 2, the $R_{\rho 1}$ values are substantially higher than the $R_{\rho 2}$ values, the R_{m1} values are quite close to the R_{m2} values, and the R_{v1} values are substantially lower than the R_{v2} values. Hence, based on the criterion of R values only, a choice between the configurations of Figs. 33a and 33b for these cases would be difficult to make. In cases 1 and 2, the width and length of the separator channel would be quite different for the configurations of Figs. 33a and 33b and it is likely that criteria considering the aerodynamic effects on the droplets (see Sec. III.A) and friction losses in the separator channel would be more important than the R values in choosing between the two configurations.

The separators as drawn in Fig. 33 have a constant channel area downstream of the nozzle exit. This criterion explains why one pair of channel walls is curved in Fig. 33b. This would be the correct design if the gas and liquid velocities were equal at the nozzle exit. It should be

noted that for nozzles with large A_R values (say, of the order of 4 or more), in the configuration of Fig. 33b, depending upon the values of θ and γ, it may well not be possible to keep the channel area constant, since the shape of the curved channel walls necessary to do so would interfere with the nozzle jets, probably causing large friction losses in the separator. In such cases, it would be necessary to accept an initial increase in the channel area, followed by a subsequent decrease to, say, the value at the nozzle exit. The latter is attainable, since as the edge of the jet moves towards the centerline (see Fig. 33b), eventually a point is reached where the channel wall can be made narrow enough to return the channel area to the nozzle exit value. If the increase in channel area necessitated by the values of A_R, θ, and γ chosen is large enough (say, by a factor of 2), large losses are likely to be incurred in the separator, since the gas will likely be expanded to a pressure below the desired discharge pressure and then recompressed, which would be a very inefficient process at the r_a values typical at the nozzle exit (often 10 or more; see diffuser efficiencies in Ref. 13).

The calculations of Ref. 9 indicate that, if the nozzle exit pressure is, in fact, at its nominal value (14.2 psia for the nozzles used in the H_2O-N_2 impinging-jet separator tests discussed in Sec. II), the gas velocity will likely be ~1.4 times the liquid velocity at the nozzle exit. To reduce the gas velocity to a value near the liquid velocity, various modifications of the separator designs sketched in Fig. 33 can be employed. First, either one or both sets of walls of the separator channel could be stepped back in order to provide the necessary increase in area. Second, the nozzles could be extended to provide the required area change, with no stepping back taking placé at the nozzle-separator channel transition. It should be noted that the tendency for the gas velocity to exceed the liquid velocity at the nozzle exit would partially relieve the problem referred to above, in which for high A_R nozzles, in the configuration of Fig. 33b, it may be necessary to have an increase in separator channel area to avoid high friction losses.

The knife-edge separator which was discussed at length in Section II had a separator channel area equal to ~1.2 times that of the nozzle exits, thus presumably reducing the average velocity difference between the gas and the liquid in the separator channel.

Many arguments have been advanced (see Sec. IV.C.1, 2 and 4) indicating that it is desirable to equalize the gas and liquid velocities at the nozzle exits, or at least early in the separator channel.

A single test was run in a configuration similar to that shown in Fig. 34. It should be pointed out that Fig. 34 is deliberately drawn with $A_R = 1$, so that it may readily be compared with the sketches of Figs. 33a and 33b; however, the test was run with the nozzles with $A_R = B_1/A_1 = 3.51$ referred to earlier in this section. It can readily be shown that with this configuration, all three R values are equal to unity, thus making it superior to either of the configurations shown in Fig. 33 on the basis of R values alone.

A possible severe disadvantage of this configuration is that the diverging flow at the nozzle exit (see right-hand sketch of Fig. 34) may impinge on channel walls E, with the latter acting as flat-plate surface separators. If this occurred to any substantial degree, particularly since $B_1 = 3.51\ A_1$, very severe friction losses would be expected in the separator. The single experiment done on this configuration showed a thrust of ~1230 lbf (at $\theta \approx 15$ deg), whereas comparable experiments in the configuration of Fig. 33a showed thrusts of 1240-1250 lbf. This would seem to indicate that no great friction loss was taking place on surface E, Fig. 34, However, an accurate comparison of the friction loss for the two different configurations cannot be done, as the isentropic nozzle exit velocity, which must be used as a normalizing factor in calculations yielding values for the friction losses, depends upon R_F, P_{NI} and the water temperature for the particular test, and these were not taken for the test in the configuration of Fig. 34. Further, since only a single test was made in this configuration, the chance that the thrust measurement was erroneous must be regarded as not negligible. Possibly the correct thrust value is much lower. It is noted that for the geometry of Fig. 34, if γ was quite large, say 15-20 deg, one would definitely expect surfaces E to act as flat surface separators, with a fairly well compacted layer of liquid flowing over their surfaces and $\tau_w \propto \rho_\ell v_{\ell b}^2$, where $v_{\ell b}$ is the liquid velocity outside the boundary layer and in most cases can be approximated by the liquid velocity at the nozzle exit. However, if γ is zero, experiments (Ref. 10, p. 181-183) have shown that $\tau_w \propto \rho_\ell v_{\ell b}^2/(r_a + 1)$.

As γ becomes smaller and smaller, eventually the wall shear stress must shift over to the lower value. The value of γ for the above-mentioned test was 2.72 deg, possibly small enough for this shift to have occurred. Rough estimates of the reduction in thrust due to frictional velocity losses in the separator channel under the two assumptions given above are 45 and 275 lbf (typical nozzle-only thrust $\simeq$ 1250 lbf). If the measured value of thrust for the single test case in the configuration of Fig. 34 is accepted as correct, the frictional losses in the separator must be of the order of the lower figure (45 lbf) and hence surfaces E (Fig. 34) do not act as surface separators. In fact, when the cos θ losses of the single test in the configuration of Fig. 34 are compared with those of the nozzle-only tests, it appears that the friction along surfaces E (Fig. 34) may be even less than those calculated by the methods of Ref. 10, p. 181-183 (for $\gamma = 0$). The statement of the last sentence depends, of course, on the accuracy of the 1230-lbf thrust measurement (taken in the configuration of Fig. 34) and the assumption that the R_F, P_{NI} and water temperature values of this test were not sufficiently different from those of the tests taken with nozzles only to make the statement incorrect.

The mass flow probe profiles taken in the configuration of Fig. 34 were slightly superior (i.e., the water flow was slightly more concentrated towards the channel centerline) than "equivalent" data taken in the configuration of Fig. 33a. Data in the configuration of Fig. 33a was taken at various x-positions, and the data used in the comparison was taken at the position which yielded the optimum liquid mass flux profile. However, only a single profile was taken in the configuration of Fig. 34; hence, unless by chance that profile was the optimum one, it is likely that an x-position can be found for the configuration of Fig. 34 for which the liquid mass flux profile is superior to the best obtainable in the configuration of Fig. 33a (operated under "equivalent" conditions).

If the performance of the separator configuration of Fig. 34 appears to be close to that of the separator configuration of Fig. 33a (in terms of z and R_B for a given R_A), the performances should be further compared by the methods of Sec. II.H; i.e., inserting the estimated performances of Li-Cs separators of the two types into Li-Cs power cycles, to see which yields the greater cycle efficiency.

IV. CHANGES IN SEPARATOR CONFIGURATION FROM THOSE DISCUSSED AT LENGTH IN SECTION II

A. Use of a Short Center Plate in the Separator Channel

For these tests the separator geometry of Fig. 24, Sec. II.F.2.b (with knife edges, etc.) was not used; rather the impinging jets from the nozzles (which were operated with the long edges of the nozzle exits adjacent, as in Fig. 24) simply discharged into a rectangular channel. The channel had the following dimensions:

Height = 6.06 in. (outside dimension of flat walls of nozzles)

Width = 3.60 in.

Length = 27.4 in.

"Separator performance" was determined from mass flow probe profiles taken across the channel midway between the top and bottom walls and the thrust of the device (taken with the probe withdrawn from the flow).

The center plate promotes concentration of the liquid (at a cost of a considerable loss in mean liquid velocity due to plate friction). It is, of course, acting as a flat surface separator (see Sec. II.G.6.c). Figure 35 shows mass flow probe profiles taken 9.2 in. downstream from the nozzle exit with θ = 10 deg, R_F = 54.8 and (1) a center plate extending 8.12 in. downstream from the nozzle exit and (2) with no plate. The nature of the concentration of the liquid flow by the plate is clearly shown. The asymmetry in the solid-lined (with plate) profile is not believed to be significant. It may be due to the fact that probe data points were not taken symmetrically about the centerline, and the plate thickness and probe hole diameter are 0.035 in. and 0.040 in. respectively, both significant distances on the abscissa of Fig. 35. There probably is a dip in the liquid mass flux directly behind the plate, since the profile was taken only 1.08 in. downstream from the end of the plate.

It is noted that the maximum probe water flow rate with the plate in place is 26.5 gm/s. The value estimated for pure water flowing at $V_1 \cos \theta$ is 63.5 gm/s. However, the discussion of Ref. 10, p. 56, indicates that at $r_a \sim 0.77$, the flow changes from a droplet flow regime to a bubble flow regime, and refers to a case where thousands of gs were applied to a flow

with $r_a \sim 0.7$ without effective separation of the gas from the liquid. Hence, it appears likely that along the flat plate a minimum value of r_a to be expected is ~0.77. With this value of r_a and with the water flowing at $V_1 \cos \theta$, the expected probe mass flow rate would be $63.5/(1+0.77) = 35.9$ gm/s. Thus the maximum measured liquid probe mass flow near the plate (Fig. 35) appears to approach fairly closely the maximum possible under the limiting conditions of $r_a = 0.77$ (26.5/35.9 = 0.74).

Figure 36 shows R_B as a function of R_A for the same conditions as those of Fig. 35, except that data for plate lengths of 0, 2.12, 5.12 and 8.12 in. is shown. Such data was obtained essentially by integrating mass flow probe profiles such as those shown in Fig. 35 (outwards from the channel centerline). Both Figs. 35 and 36 show that the plate length has little effect on the flow farther than ~0.7 in. from channel centerline (corresponding to $R_A \simeq 2.1$). Flow in this region is probably controlled largely by the aerodynamic and nozzle divergence effects mentioned in Section III. It is noted from Fig. 36 that for $R_A > 5$ a substantial reduction in R_B is obtained if one changes from the case with no plate to that with a plate 5.12 in. long. The R_B data for a 8.12-in.-long plate is inferior to that for a 5.12-in.-long plate. This cannot be explained by the author.

The question arises as to whether a short plate (2 to 5 in. long) could establish a zone of concentrated liquid which would continue to aid concentration of the liquid flow substantially downstream of the end of the plate. (See Sec. II.G.6.c , especially with respect to the impact of droplets on a sheet of liquid.) If the concentration of the liquid flow produced by this short plate was equal or superior to that produced by longer plates (8 - 11 in. long), the advantage of better concentration of the liquid flow could be achieved with a substantial reduction in plate friction losses. To check this hypothesis, values of R_A, R_B and z calculated for plates of various lengths (and with data taken at different x-positions) were used to estimate cycle efficiencies by the methods of II.H. The results of these calculations, for the x-positions which yielded the highest efficiencies, are shown in Fig. 37. The higher curves are for the case where the liquid flow bypassing the main capture slot can be separated and diffused so that it can be returned to the nozzle inlet. The lower curves are for the case where the liquid bypass flow must be returned (with a total loss of its kinetic energy) to the main

nozzle jet. These cases are discussed at length in Sec. II.H. It must be pointed out that the R_F value at which the data shown in Figs. 35 - 37 was obtained is about twice the value necessary for the best simulation of Li-Cs systems (see Secs. II.H.3 and I.E.4 and 5). The R_B versus R_A curves are known to be slightly better (i.e., with more liquid concentrated towards the centerline) for $R_F \simeq 54.8$ than for $R_F \simeq 26.3$ (about the optimum value for simulation of a Li-Cs system); see, for example, Fig. 7, Sec. II.C.1 and Fig. 12, Sec. II.C.4. The experiments were run at $R_F \simeq 54.8$. Rough estimates of the efficiency changes from those shown in Fig. 37 to those calculated using separator data for $R_F \simeq 26.3$ are as follows. All curves in Fig. 37 would be lowered by 0.005 to 0.01, but the author can see no reason why the shape of the curves should change.

Note the large increase in efficiency (for the lower curves) in going from the case of no plate to that of a plate 5 to 6 in. long. For still larger plates the efficiency decreases because of the increased plate friction and the (unexplained) decrease in effectiveness in concentrating the liquid flow (compare the curves of Figs. 36 for plate lengths of 5.12 and 8.12 in.). If the liquid bypass flow can be returned to the nozzle inlet without pumping (upper curves in Fig. 38), the increases in efficiency obtainable in going from no plate to a plate length of 5 to 6 in. are much smaller, but for the $x = 11.2$ in. curve, in any case, they are still significant.

The separator geometry with which all the data of this section was obtained is sketched (in part) in Fig. 38b. It may be possible to establish a central zone of concentrated liquid using a curved surface separator 2 - 3 in. long which would be as effective in concentrating the liquid downstream of the end of the surface separator (or plate) as the flat center plates 5 - 6 in. long, which yield the maximum calculated Li-Cs cycle efficiencies (see Fig. 37). It is hoped that this would be the case on the basis of the arguments of Sections II.G.6.a and b. If the shorter (2 to 3-in.-long) curved surface separator was as effective in concentrating the liquid flow well downstream of its trailing edge as the 5.12-in.-long flat center plate, calculated cycle efficiencies would show a considerable increase because of the lower friction loss on the (shorter) separator surface.

B. The Louvre Separator

The apparatus is shown in Figs. 39 and 40. The same nozzles were used as in the impinging-jet separator experiments described up to this point. From the outermost edge of the nozzle exits louvre panels extended downstream. The downstream ends of the louvre panels formed the "capture slot." The louvre angles are shown in Fig. 39. Owing to the great stress on the thin louvres, it was found necessary to braze a number of 0.25-in.-diameter stainless steel tubes between every pair of louvres; these are visible in Fig. 40. The position of the downstream ends of the louvre plates could be varied to change the "capture slot" width (which determines R_A). The fraction of the liquid bypassing the "capture slot" (R_B) was determined by passing the gas containing the bypass liquid through a gravity separator (shown in Fig. 5, Sec. II.A).

The performance of the louvre separator (R_B, R_A and z) for any given set of conditions was determined as follows. The determinations of R_B and R_A were described in the previous paragraph; z can readily be determined with the aid of thrust measurements. Measurements were taken at the R_F values of ~14.9, ~ 26.3, ~ 54.8 and ~ 86.3 at several different values of "capture slot" width, and for θ = 10 and 15 deg. The distance from the nozzle exit to the captive slot is 10.3 in.

Louvre separator and knife-edge separator R_B and z values are compared (for θ = 10 deg and $R_F \simeq 26.3$) in Figs. 41a and 41b. The distance from the nozzle exits to the knife-edge tips for the knife-edge data was that which yielded the minimum values of R_B, and probably yielded values of z fairly close to the minima (see discussion of Sec. II.I). The distance from the nozzle exits to the "capture slot" for the louvre data was fixed at 10.3 in. The latter value was selected as a rough mean of the optimum values observed for knife-edge operation (the optimum x-position for knife-edge operation shifts from about 9 in. for R_A = 5.85 and 3.87 to about 11 in. for R_A = 2.92 and 1.94.) From Fig. 41, it can be seen that, at the same value of R_A, the louvre separator has substantially lower R_B values than the knife-edge separator and substantially higher z values. These differences can be explained qualitatively as follows. The louvre slots force the gas to turn through ~150 deg to escape from the main flow; the gas can turn readily, but a substantial fraction of the liquid tending to follow this gas (which

would be lost to capture by the capture slot if the louvres were not present) cannot make the turn, impacts on a louvre plate, and is returned to the main flow towards the capture slot. This liquid impacts louvres (with impact dissipation) and also (for a short distance) flows along the louvres; hence it would be expected to suffer a considerable loss of momentum. These momentum losses are believed to account for the relatively high value of z for the louvre separator (see Fig. 41b).

A crude estimate of the fractional velocity loss of the liquid returned to the main flow by the louvres is made as follows. For the same θ, R_F and R_A values and nearly the same x-position of the "capture slot," the liquid momentum entering the louvre "capture slot" is assumed to be equal to that entering the knife-edge capture slot, plus that of the liquid returned to the main flow by the louvres. The mass flow of the latter is approximated by $R_{BK} - R_{BL}$, with the total liquid mass flow at the nozzle exits taken as unity. (The subscripts K and L refer to the knife-edge and louvre data, respectively.) An approximation in this calculation is the neglect of any interference between the relatively concentrated flow travelling down the inside edge of the louvre panels (as noted in mass flow probe profiles taken across the "capture slot" in louvre tests) and the flow which would be reaching the outermost parts of the capture slot in the corresponding knife-edge case. It is assumed that these flows just add together in the louvre test case. On the basis of these assumptions, the following equation can be written.

$$(1 - R_{BL})(1 - z_L) = (1-R_{BK})(1 - z_K) + (R_{BK}-R_{BL})(1-z_R) \qquad (30)$$

where subscripts K and L refer to the corresponding knife-edge and louvre cases, and z_R is the average fractional velocity loss fraction of the liquid velocity at the nozzle exit of the liquid returned to the main flow by the louvres, the quantity sought. For $\theta = 10$ deg, z_R is calculated as 0.4 to 0.5, with no obvious dependence on R_F or R_A. For $\theta = 15$ deg, z_R shows no obvious dependence on R_F, but does show some dependence on R_A; z_R ranges from 0.25 to 0.37 for the smallest value of R_A for which the calculation was made ($R_A = 1.95$), but ranges from 0.40 to 0.57 for R_A values of 2.7 and 3.6. The author has no explanation for the above-mentioned

magnitude and variations of z_R and reminds the reader that these values are subject to considerable error because of the crudeness of the method employed for their calculation. Nevertheless, it is believed that these calculations do give evidence (of significant weight) that with the above-discussed louvre separators the liquid returned to the main flow by the louvres is returned in general with a loss of 0.35 to 0.55 of its original momentum parallel to the channel centerline.

The following paragraphs deal with the comparison of Li-Cs cycle efficiencies, using the R_A, R_B and z data for the knife-edge and louvre separators discussed earlier in this section (e.g., see Fig. 41). The method of calculation is that presented in Sec. II.H. An R_F value of 26.3 was chosen for the comparison, since following the analyses of Sec. I.E., this R_F value for the H_2O-N_2 separator tests gives the best simulation of the Li-Cs system separator. Note that Fig. 42 is the same as Fig. 32, Sec. II.H.4, with the addition of the curves for the louvre separator. From the curves of Fig. 42 it is noted that if the liquid bypassing the main capture slot must be returned with a total loss of its kinetic energy to the main jet, curves (1), the louvre separator is substantially superior to the knife-edge separator. From the shape of the "louvre (1)" curve, it appears that zero efficiency might just be reached at $R_A \simeq 5$. If a louvre separator operating at this R_A value was used with a center plate ~5 in. long (see lower curves, Fig. 37, Sec. IV.A), the combined advantage of the use of louvres and a center plate might allow estimated cycle efficiencies of ~0.02 to be obtained without returning the bypass liquid (without pumping) to the nozzle inlet. As can be seen in Fig. 42 (not considering the use of the center plate), if the bypass liquid can be returned to the nozzle inlet (without pumping), the knife-edge separator will give better performance than the louvre separator—comparing curves "knife-edge (2)" and "louvre (2)." The author believes that return of the bypass flow of the louvre separator to the nozzle inlet (without pumping) is considerably more difficult than similar return for the knife-edge separator. This is on account of the very large velocity losses likely to be suffered by the bypass liquid in the louvre separator (due to impact against louvres, turning ~150 deg, and friction along the louvres). Hence, it is believed that curve "louvre (2)" is unlikely to be obtained, but that the curve "knife-edge (2)" has a considerably greater possibility of being attained. Summing up the discussion of Fig. 42 it appears from said

figure that the relative efficiencies of the two systems being considered depend strongly on the extent to which the condition of returning the bypass flow to the nozzle inlet without pumping can be approached. If said process turns out to be almost completely unrealizable, the louvre separator clearly provides higher efficiencies (see Fig. 42) - though for these calculations, still negative. On the other hand, if the return process turns out to be achievable to some degree, especially if it can more closely be approached by the knife-edge separator (as is thought likely), then the latter separator may turn out to provide higher efficiencies.

The gas flow pattern believed to exist near the inside edge of the louvre panel is sketched in Fig. 43. The author believes that a great many of the droplets which would completely escape the capture slot without louvres have paths similar to that shown as line F and are partially returned to the main flow as sketched. If α is the angle of impact at point E, the fraction of the flow starting off, at least, back towards the main flow is $(1 + \cos \alpha)/2$. If $\alpha = 45$, this fraction is 0.853. Some of the variables in louvre design are:

(1) Angle of louvres (with respect to louvre panel).

(2) Spacing between louvres W.

(3) Length of louvres L.

(4) Shape of the louvre plate (the plates discussed up to this point were flat; curved plates may prove better).

A very brief discussion of some ideas with respect to these variables is given below.

With respect to variable (1) it must be remembered that there is in fact a wide spectrum of droplet sizes moving along the inside edge of the louvre panel. "Large" droplets (with respect to the droplet for which the path is shown in Fig. 43 as line F) starting at point G would tend to travel in a straight line parallel to the channel centerline until they struck louvre plate 2. "Small" droplets (by a similar criterion) would tend to follow the gas flow and escape up the channel between louvre plates 1 and 2. Decreasing β to, say, 15 deg, might improve or worsen the louvre separator performance, depending on the relative amounts of the liquid flow at the edge of the louvre panel made up of "large" and "small" (and "other-sized")

droplets. If the "large" droplets predominated, the louvre separator performance would increase with a decrease in β since the fraction of the droplet flow returned to the main flow on impact $[(1 + \cos \alpha)/2]$ would increase, as well as the component of velocity of that portion of the flow (neglecting friction effects). If "small" droplets predominated, it can be shown that the higher velocity upwards between the louvre plates (due to the decrease of β) would tend to sweep away more of the droplets, thus increasing R_B. Further, with a limit on how thin the louvre plates can be made (with respect to consideration of strength) as β becomes smaller, more of the gas discharge area is taken up by the plates, thus further increasing the gas velocity between the plates. This same effect will increase the pressure drop across the plates, which, for a given pressure on the downstream side of the louvres will raise P_{NE}; as P_{NE} is raised, the jet velocity at the nozzle exit will start to fall off, thus reducing separator performance (see Sec. II.F.2.b). With the present state of the theory, especially with an unknown droplet size distribution near the inside edge of the separator panel, the optimum β can essentially be determined only by cut and try.

With respect to variable (2) it is believed that there are good reasons for making this variable (W) as small as practical. With a given size distribution of droplets flowing along the inside edge of the louvre panel, the smaller W is, the less likely droplets are to follow the gas, and for larger droplets, α will tend to be smaller. This follows since, while moving between the edges of any two successive louvres, the droplets will be subject to gas velocities tending to shift their paths away from a direction parallel to the channel centerline for a shorter time. Two limitations on the decrease in W are given below. First, if for reasons of strength or other reasons, the thickness of the louvre plates cannot be decreased beyond a certain limit, as W is decreased, the plates will occupy a larger and larger fraction of the channels for gas escape, thereby increasing the gas velocity in the escape channels and tending to increase the fraction of droplets escaping with the gas. This would also tend to increase the pressure drop across the louvre panel.

Second, even if the louvres were infinitely thin, there might be an increase in louvre panel pressure drop. As W is decreased, one should be able to decrease the length, L, of the louvres, thereby presenting the same

total area for friction pressure drop. However, for smaller L values the skin friction coefficient should increase (since Re_L would decrease); hence the pressure drop would be expected to increase, though by a small amount, for any reasonable change in W and L.

With respect to variable (3), this is largely determined by β and W. For a given β and W (other conditions being the same), the larger L is, the greater would be the expected louvre panel pressure drop. It would appear that the best value of L would be the smallest that could be used without a detrimental increase on R_B. For the panel shown in Fig. 39, W = 0.25 in. and L = 0.87 in. It appears possible that a somewhat smaller value might be permissible, perhaps 0.5 to 0.6 in.

Turning now to variable (4), it is first noted that most of the liquid lost through the louvre panels in the tests described earlier in this section was observed to occur in the downstream one-third to one-quarter of the panel. It seems possible that lower R_B values could be obtained if the panels were curved so that they ran roughly as sketched in Fig. 39 for the first, say, two-thirds of their length and then curved outwards somewhat for the last one-third of their length, thereby decreasing the velocity necessary for the gas to escape through the louvre slots in this region. This might well lead to a reduction of the liquid carried off by gas flowing through the last third of the panel. Since for the same R_A value approximately the same total amount of gas must escape through the louvres, this proposal to reduce the gas escape velocities for the last third of the louvre panel, assuming the same β, L and W values throughout the panel, must either be accompanied by an increase in the gas escape velocity for the upstream two-thirds of the panel or a lengthening of the panel. For the last third of the panel, where most of the liquid is observed to escape in the geometry of Fig. 39, it might also be advisable to change β, L and W (discussed above). Recommendations for these latter changes cannot be made here with any degree of confidence at this time.

A very brief discussion is now presented on the question of which pair of surfaces of the separator channel should be louvred (in some cases, the best results may be obtained if both pairs are louvred). In the configuration of Fig. 39, the side walls (defined as those fairly close to being parallel to the plane of impact of the nozzle jets) are louvred, whereas the top and

bottom walls (defined as those fairly close to being perpendicular to the plane of impact of the nozzle jets) are unlouvred, i.e., solid. The top and bottom walls for the case of Fig. 39 are parallel to the plane of the paper. If the louvred walls were made unlouvred (i.e., solid) and vice versa for the configuration of Fig. 39, the effects discussed below would occur.

Since the nozzle exit has a height (perpendicular to the paper) of 5.56 in. and a width of 1.586 in., the aspect ratio of the nozzle exit is 5.56/1.586 = 3.51, and the louvre panel area would be decreased by a factor of 2 to 3 if the above-mentioned change were made. Two important effects are:

(1) The necessarily higher mean velocity of the gas escaping between louvres would lead to a substantial increase in the mean liquid flow per unit area of louvre panel (assuming that louvres with the same β, W and L were used in both cases). Whether or not this would be offset sufficiently by the decreased louvre panel area to lower R_B is not known. This would depend on the droplet size distribution near the inside edge of the louvre panels (among other things); the author believes the droplet flow paths of importance to be very difficult to calculate. (The gas flow pattern must be known with some degree of accuracy – not just as roughly sketched in Fig. 43.)

(2) The same increased velocity will increase the pressure drop through the louvre panel, and the resulting increase in P_{NE} will reduce the jet velocity at the nozzle exit.

Effect (2) is definitely detrimental to separator performance, but the magnitude of this effect may be so small compared to that of effect (1) that it can be discounted. A third possible placing of louvre panels is to make both pairs of walls louvred.

The questions raised above cannot, in the main, be answered here; the main point of these two paragraphs is to emphasize that, for nozzles with rectangular nozzle exits, there are at least three fundamentally different possible placings of louvers:

(1) In the pair of channel walls nearly parallel to the impact plane of the two jets.

(2) In the pair of channel walls nearly perpendicular to the impact plane of the two jets.

(3) On both pairs of walls mentioned in (1) and (2).

Depending on the details of the particular nozzle and separator under consideration, any of the three placings listed above might prove to yield the best separator performance. Other configurations such as louvring a pair of walls through only part of their length might also be considered.

C. Attempts to Improve Separator Performance by Reducing the Velocity Difference Between the Liquid and the Gas Either in the Last 5 to 6 Inches of the Nozzle or in the First Few Inches of the Separator Channel

All discussion in Sec. IV.C is with respect to separator operation with the nozzle jets impinging in a rectangular channel 27 in. long. There are no capture slots, angles in the channel wall, etc., as sketched in Fig. 24, Sec. II.F.2.b. At the downstream end of the channel, the flow discharges to the atmosphere. Separator performance is estimated with the aid of mass flow probe profiles across the channel and thrust data.

The flow pattern is roughly sketched in Fig. 44; the bulk of the liquid flow in the separator channel lies within zone B. First, it is noted from the calculations made by the method of Ref. 9, if the nozzle exit pressure is at the nominal value (14.2 psig), the ratio between the gas and liquid velocities at that point ranges from 1.4 to 1.55. Side wall pressure profiles were taken at $R_F \simeq 54.8$, $\theta = 10$ deg, a ratio of channel area to nozzle exit area of 1.238 (A_R') (the smallest readily attainable), and a calculated ratio between gas and liquid velocities at the nozzle exit (based on $P_{NE} = 14.2$ psia) of 1.45. In this case, the static pressure curves were found to follow the nozzle-only curves up to 2 in. upstream from the nozzle exit, decrease to a minimum value of 0.7 psig at the exit, and then increase to a maximum value of 1.2 psig 4.5 in. downstream from the nozzle exit. Downstream from this point the pressure decreased nearly linearly to 0 psig at the channel exit. By contrast, similar profiles taken at the same θ and R_F values for A_R' equal to 1.458 and 1.672, showed the pressure to be 0 psig (14.2 psia) at the nozzle exit and to maintain this pressure within ±0.3 psi throughout the length of the channel. The above-mentioned changes in A_R' were achieved by moving the side walls of the separator channel (those walls parallel to

the plane of impact of the jets). Based on this data, if A_R' were equal to unity, for the same θ and R_F values discussed above, a nozzle exit pressure of ~1.4 psig and a maximum channel pressure of ~ 2.4 psig can roughly be estimated.

It is noted that even for the pressures estimated in the channel for $A_R = 1$, the pressure gradients in the channel are very small: of the order of one-tenth of typical pressure gradients near the nozzle exit (but within the nozzle). Hence the following estimate for the distances down the channel over which the gas is slowed towards the liquid velocity should be a fair approximation to the true values. It is based on conditions at the nozzle exit as calculated by the methods of Ref. 9 (for $R_F \simeq 54.8$) and for zero pressure gradient in the channel. The difference between the gas and liquid velocities is calculated to be reduced to half its nozzle exit value in approximately 0.65 in. and to 0.2 of this value in approximately 2.3 in. Based on this calculation and the aforementioned pressure profiles, the phenomena taking place in the nozzle and channel (for $A_R' = 1$) would probably be as follows. First, since the nozzle exit pressure is somewhat higher than nominal, the ratio between the gas and liquid velocities out the exit (R_v') will be somewhat lower than calculated by the methods of Ref. 9. If the nozzle exit pressure were, in fact, 1.4 psig, as estimated above, R_v' should be reduced to approximately $14.2/(1.4+14.2) \times 1.45 = 1.32$. Secondly, as the flow enters the low-pressure-gradient environment of the channel, the gas in region B (Fig. 44) should rapidly slow down towards the liquid velocity. As mentioned earlier, the velocity difference is estimated to be reduced to half its nozzle exit value in approximately 0.65 in. However, from our (estimated) pressure profile for $A_R' = 1$, the pressure in the channel does not rise sufficiently to accommodate this slowdown by compressing the gas in region B. Hence, it appears likely that a substantial fraction of the gas flow moves from region B to region C in the first few inches of the channel flow. To satisfy the gas continuity equation, this gas must travel at a higher velocity than the gas at the nozzle exit (as long as the gas in region B is travelling at speed lower than at the channel exit, which is likely, based on previous arguments). As one moves further downstream and region C takes up more of the width of the channel, the gas velocity there will lower itself towards the value at the nozzle exit. The pressures at the nozzle exit and the maximum pressure in the channel (our estimates) are believed to be

primarily necessitated to drive the (relatively) high-velocity gas in region C (Fig. 44) towards the channel exit. Much of the preceding argument depends upon our (estimated) values for the nozzle exit and maximum channel pressure for the case with $A_R' = 1$. If these pressures are considerably higher than the estimates (say, of the order of 6 psig), then R_v' may approach unity, and the necessity for the substantial difference between the gas velocities in regions B and C, say 1 to 2 in. downstream from the nozzle exit, vanishes. The author believes that these pressures may be somewhat higher than the rough estimates given above but not as high as 6 psig because of the relatively easy avenue of escape for the gas from nozzle exit to channel exit provided by region C (Fig. 44). Hence, the above-discussed difference between the gas velocities in regions B and C is believed to occur to a substantial extent for the case with $A_R' = 1$. (Experiment would, of course, confirm or disprove this contention).

1. Shear effect. If the above-discussed phenomena do, in fact, take place in a nozzle-separator system with $A_R' = 1$, then large gas velocity shears would be expected to exist in the region of the boundary between regions B and C (Fig. 44), especially on the upstream part of the channel. Two cases are considered: one in which the gas velocity is essentially identical in regions B and C (as might occur if $R_v' = 1$) and a second in which the large shears mentioned above occur. (The two cases are considered to be essentially identical in all other ways.) In the case with the high shear, one would expect many more violent droplet collisions (with shattering) to occur in the region of the B-C boundary (Fig. 44), and hence the mean droplet size in this region would be smaller than for the other case. The smaller the mean droplet size, the more readily the droplets will turn to follow the gas flow (see Sec. III.A.1) and never reach the central zone of concentrated liquid. For the cases considered above, for which the calculated value of R_v' is 1.45 (at $P_{NE} = 14.2$ psia), one might conclude that the effect discussed would worsen the separation process (measured by, say, R_B values at a given R_A) as A_R' decreased from 1.45 to unity. This effect will be discussed in more detail in Sec. IV.C.4.

2. Slip effect. A second argument for poorer performance of separators with $A_R' = 1$ compared to those in which A_R' is essentially equal to the calculated value of R_v' (other things being equal) follows. There is

(according to the model presented above) a considerable difference between the components of the gas and liquid velocities parallel to the channel centerline in 2 regions:

(1) The upstream 1 to 2 inches of region B (Fig. 44).

(2) The region of the B-C boundary.

In these regions, assuming the gas to be moving parallel to the channel centerline (see Sec. III.A.1), the velocity diagram for the gas and a liquid droplet can be drawn as shown in Fig. 45. The following approximate form of the drag coefficient for a sphere is used to estimate the effect of aerodynamic forces on a droplet (as was done in Sec. III.A.1).

$$C_D = 0.5 + \frac{24\mu_g}{\rho_g v_{\ell g} D} , \tag{31}$$

where $v_{\ell g}$ is the magnitude of the vector difference between the gas and liquid velocities.

Calculating the component of the force on a droplet perpendicular to the channel centerline shows that, for given values of u_ℓ, ρ_g, μ_g and D, the term corresponding to the first term in Eq. (31) is proportional to $\alpha\beta$ (see Fig. 45), whereas the term corresponding to the second term in said equation is proportional to α. Further, for a second case with equal components of the gas and liquid velocities parallel to the channel centerline and u_ℓ, θ, ρ_g, etc., as for the first case, the first term (in the force expression) is proportional to α^2 and the second term to α.

The first term would be greater by a factor of

$$\beta/\alpha = \left[u_\ell^2 \sin^2\theta + (u_g - u_\ell \cos\theta)^2\right]^{1/2} \Big/ u_\ell \sin\theta$$

for the case of Fig. 45, while the second terms would be equal for the two cases. For $\theta = 10$ deg and $u_g/u_\ell = 1.5$, $\beta/\alpha = 3.12$, a substantial increase. The first term in Eq. (33) tends to predominate for $(\rho_g v_{\ell g} D)/\mu_g > 50$ and the second term for $(\rho_g v_{\ell g} D)/\mu_g < 50$. For the largest-size droplets expected at the nozzle exit, $(\rho_g v_{\ell g} D)/\mu_g$ ranges from 200 to 500; hence the above effect should be significant for them.

3. The three types of experiment. All of these experiments were done with $\theta = 10$ deg, and for $R_F \simeq 14.9$ and/or 54.8 as stated in the context.

(1) Moving back the side walls of the separator channel (walls parallel to the plane of impingement of the jets) to yield A'_R values of 1.238, 1.458 and 1.672.

(2) Moving back the top and bottom walls of the separator channel (walls perpendicular to the plane of impingement of the jets) to yield A'_R values of 1.238, and 1.645.

(3) Changing the nozzle inlet pressure from 150 psia to 110 psia (keeping the same R_F value); this makes the last 3-4 in. of the nozzle have very low pressure gradients; A'_R remains at 1.238, but R'_v is reduced to~110/150 × 1.45 = 1.065.

A typical profile for case (2) is shown in Fig. 46, which illustrates terms using in the following discussion. The maximum (of the profile) is obvious. The author refers to the "wings" (of the profile) as the region outside of the rapid falloff of liquid flux as one moves away from the centerline. Discussion of the results for the three cases listed above follows.

(1) The profiles for the three values of R_A had nearly identical maxima and shapes out to and including the inner portion of the wings. The outer portions of the wings were essentially flat for $R'_A = 1.238$, gradually changing to a sloped curve as R'_A increased, but keeping the total mass flow on the outer portion of the wings constant. As far as capture by a capture slot of any reasonable width is concerned, the R_B versus R_A plots for these three cases would be nearly identical.

(2) For both $R_F \simeq 14.9$ and $R_F \simeq 54.8$, the shapes of the curves (one measure of which is maximum height divided by mean wing height) were slightly better for ratios of channel area to nozzle exit area (R'_A) of 1.645 than for 1.238. However, the capture slot height would have to be 6.06 in. for $R'_A = 1.238$ (the outside dimension of the flat walls of the nozzle) and 8.06 in. for $R'_A = 1.645$. Hence the mean liquid flux passing through capture slots allowing similar R_B values (i.e., capture slots of almost identical width) would be substantially lower for $R'_A = 1.645$ than

for $R'_A = 1.238$; i.e., the factor $8.06/6.06 = 1.33$ overcomes (by a large margin) the slightly superior profile for $R'_A = 1.645$.

(3) Based on the ratio of maximum liquid flux to mean wing liquid flux the separation process is significantly superior at $P_{NI} \simeq 150$ psia, both for $R_F \simeq 14.9$ and $R_F \simeq 54.8$. However, even if the corresponding profiles (profiles with the same R_F value) were of exactly the same shape (on semilogarithmic coordinates, as Fig. 46 is drawn), the separation performance could be judged inferior for the $P_{NI} \simeq 110$ psia case for the following reason. What one is trying to simulate (with the $P_{NI} \simeq 110$ psia tests) is the operation of the standard nozzles extended so that the final nozzle exit area is near that required for $R'_v = 1$, with $P_{NI} \simeq 150$ psia and $P_{NE} \simeq 14.2$ psia. From the $P_{NI} \simeq 110$ psia, $P_{NE} \simeq 14.2$ psia tests, this simulation appears to be reasonable. Since nozzle wall pressure taps show that, under these conditions, the last 3 to 4 in. of the nozzle is at nearly constant pressure, as the nozzle area continues to expand towards the exit, the gas can readily slow down to a velocity quite close to that of the liquid. However, for the extended nozzle, $P_{NI} \simeq 150$ psia, $P_{NE} \simeq 14.2$ case, the liquid flux at the nozzle exit will be reduced (compared to that obtained with standard-length nozzles) by the area ratio of the extension. From Sec. II.D, it is noted that the maximum flux on the channel centerline tends to bear a fixed ratio to that at the nozzle exit. Further, in Sec. III.B, data is presented which shows that this ratio appears to be almost independent of the nozzle width over a width range of 4:1. Thus, unless the reduced R'_v value occurring, for example, in the $P_{NI} \simeq 110$ psia and $P_{NE} \simeq 14.2$ psia cases can produce a separation process (e.g., as measured by the shape of the mass flow probe profile) markedly superior to that for $P_{NI} \simeq 150$ psia, $P_{NE} \simeq 14.2$ psia, the performance of the latter separator would very likely be superior to that of a $P_{NI} \simeq 150$ psia, $P_{NE} \simeq 14.2$ psia extended nozzle separator. Let us suppose that the mass flow probe profiles of the standard nozzles operating at $P_{NI} \simeq 110$ psia, $P_{NE} \simeq 14.2$ psia and at $P_{NI} \simeq 150$ pisa, $P_{NE} \simeq 14.2$ psia have the same shape (on a semilogarithmic

plot). Then, from the above discussion, the extended $P_{NI} \simeq$ 150 psia, $P_{NE} \simeq 14.2$ psia nozzle would be expected to produce a probe mass flux profile (at the optimum y-position) which is broader and has a lower maximum than that for the standard nozzles operating at $P_{NI} \simeq 150$ psia and $P_{NE} \simeq 14.2$ psia. A separator exploying the extended nozzles would therefore be expected to perform worse than the standard configuration. The $P_{NE} \simeq 110$ psia, $P_{NE} \simeq 14.2$ psia cases showed no evidence of producing a separation process superior to that of the $P_{NI} \simeq 150$ psia, $P_{NE} \simeq 14.2$ psia case (based on the shape of the mass flow probe profile on a semilogarithmic plot); rather, as mentioned above, the reverse was true.

Summing up the above discussion, it appears very likely that extending the standard nozzles so that R'_v is reduced to near unity at the nozzle exit (with $P_{NI} \simeq 150$ psia, $P_{NE} \simeq 14.2$ psia) would produce a markedly poorer separation process.

4. Discussion of the results of Section 3. Two points should be brought out immediately. First, all three methods described above involve increasing the area of the channel (either by stepping back one pair of channel walls or by effectively "extending" the nozzle) above that which would be predicted by the methods of Ref. 9 for that at the nozzle exit (for operation at $P_{NI} \simeq 150$ psia and $P_{NE} \simeq 14.2$ psia). Any increase in channel area is going to tend to be filled by the gas flow (up to such large A'_R values that outside air is sucked into the channel), unfortunately tending to carry some liquid with it. This obvious effect is believed to account, to a substantial degree, for the poor performance of the modified separators mentioned in the pairs of paragraphs (2) and (3) above. For any reasonable capture slot size, it does not have any effect on the R_B values obtained with the modified separator of the pair of paragraphs (1).

It is to be noted that for the apparatus discussed in the pairs of paragraphs (2), A'_R values of only 1.24 and 1.66 were tested. Further, for the tests of the pair of paragraphs (3) A'_R was kept at 1.238 and (estimated) R'_v values of ~1.45 and ~1.065 were tested. For both cases, the tested conditions bracket the "ideal conditions" of $A'_R = R'_v$. It is possible that operating the separator modifications of the pairs of paragraphs (2) and (3) with

$A'_R \simeq R'_v$ may produce substantial improvement in the separator performance. From a detailed examination of the existing data, the author does not consider this very likely. This remark does not apply to the separation modification described in the pair of paragraphs (1), for which data is available of $A'_R = 1.458$ (and two other values).

It should be pointed out that the mechanisms for degradation in performance described in Sec. IV.C.1 and 2 were essentially compared for nozzle-channel combinations for which the A'_R was unity; the difference was that in one condition the gas was assumed to be moving substantially faster than the liquid at the nozzle exit, while in the other case, these two velocities were the same. These cases might approximately apply to the cases discussed in the pair of paragraphs (3), if tests had been made of $A'_R \simeq R'_v$, but do not apply very well to the cases of the pairs of paragraphs (1) and (2). With respect to the latter, the two phenomena will be reviewed, with the aid of Fig. 47, drawn for the cases of the pairs of paragraphs (1) and (2) above, for $A'_R = 1.45$, equal to the estimated value of R'_v). First, the shear effect (Sec. IV.C.1) is reviewed.

In the configuration sketched in Fig. 47, the very rapid deceleration of the gas in the upstream part of region B (See Sec. IV.C) will probably force high gas velocities to occur in the upstream inch or so of the boundary region B-C, since the gas cannot instantly take advantage of the available increase in area. The most upstream part of the regions would probably be occupied by a vortex, as sketched in Figs. 47a and 47b. However, by the time the flow has moved approximately 2 in. downstream from the nozzle exits, the gas velocity in regions C will probably be not very different from that in regions B. The point is that high gas velocity shear will probably not continue to exist well downstream of the nozzle exit, say by the time the flow has reached points F and G in Figs. 47a and 47b respectively, as was predicted for the case presented in Sec. IV.C.1 for which $A'_R = 1$ but R'_v was substantially greater than unity. However, high gas velocity shear will exist for the first inch or so of the flow in the channel, in the regions of points D and E in Figs. 47a and 47b respectively. The gas velocity shear in the latter regions might turn out to be quite important and one of the reasons that stepping back the side walls or top and bottom walls so that $A'_R \simeq R'_v$ does not appear to lead to much improvement in separator

performance. This was observed experimentally for the cases of the pair of paragraphs (1), Sec. IV.C.3.

The following point applies to both the shear effect (Sec. IV.C.1) and the slip effect (Sec. IV.C.2) with respect to measurements in the configuration change discussed in the pair of paragraphs (2), Sec. IV.C.3. The measurements were made in the channel centerplane (parallel to the top and bottom walls) 9 in. downstream from the nozzle exit, and the nozzle half-height (H/2, Fig. 47b) is 3 in. Hence it is possible that these measurements essentially do not feel the effects of the variation of the separator geometry, i.e., the change of position of the channel top and bottom walls. Measurements closer to the top and/or bottom wall(s) might well be necessary to accurately assess the effects of said changes.

The slip effect is reviewed below. In the first presentation (Sec. IV.C.2) the slip effect was presented as occurring in 2 locations:

(1) In the first inch or two of region B.

(2) In the region of the boundary between regions B and C.

From the review of the shear effect presented above and the sketches of Fig. 47, it appears that, for these separator geometries, the slip effect will still occur in the first inch or two of region B. However, in the region of the boundary between regions B and C, the effect should be restricted to the first 1 or 2 in. from the nozzle exit. Hence, the slip effect for the case of $A'_R \simeq 1.45$ (with $R'_v \simeq 1.45$) may reduce the effectiveness of the separation process to a degree comparable to that which it would for a case with $A'_R = 1$ (and $R'_v = 1.45$), for the separator configuration shown in Fig. 47. If this is so, it may also aid in explaining why the separator performances discussed in the pairs of paragraphs (1) and (2) were not improved as A'_R was increased from 1.238 to 1.458 (for the first case) and from 1.238 to 1.645 (for the second case).

5. Summing up of Section IV.C. The changes in the separator configurations discussed in Sec. IV.C.3, pairs of paragraphs (1) and (2), were unsuccessful in producing better separator performance by increasing A'_R from 1.238 to 1.458 to 1.672 for the first case and from 1.238 to 1.645 for the second case. Likewise, separator performance was not improved by the change in operating conditions described in the pair of paragraphs (3),

which involved keeping $A'_R = 1.238$, but changing the estimated value of R'_v from ~1.45 to ~1.06; R'_v was estimated to be 1.45 for all these cases except for the case of the pair of paragraphs (3) mentioned immediately above.

Three phenomena were discussed with respect to possible effects which they might have on separators of different configurations and with different A'_R and R'_v values.

(1) The shear effect (Secs. IV.C.1 and 4).

(2) The slip effect (Secs. IV.C.2 and 4).

(3) Effect of gas flow tending to expand to fill the channel area (carrying liquid with it) for reasonable increase in A'_R or nozzle exit area (Sec. IV.C.4).

Other phenomena will undoubtedly occur.

It appears that an A'_R value of 1.238 is satisfactory for the calculated value of R'_v (at $P_{NE} \simeq 14.2$ psia), and with respect to increases in A'_R produced by the separator geometry changes discussed in the pairs of paragraphs (2) probably produces the best separator performance. The operation of the nozzles at $P_{NI} \simeq 110$ psia, $P_{NE} \simeq 14.2$ psia [pairs of paragraphs (3)], reducing R'_v from ~1.45 to ~1.06 with $A'_R = 1.238$ produced a definite worsening of separator performance.

It may be, however, that reducing A'_R from 1.238 to unity (for the estimated value of R'_v at $P_{NE} \simeq 14.2$ psia) would produce poorer separator performance; this has not been checked. Under these conditions, the shear and slip effects mentioned above might degrade the separator performance considerably below that for $A'_R = 1.238$.

D. The Converging Nozzle

Figure 48 shows a sketch of the internal surfaces of the so-called converging nozzle and the separator channel used with it. The flow converges in one direction at the nozzle exit, while diverging at right angles to this direction. The length of the nozzle and variation of flow area along the nozzle are identical to those of the nozzles used in the experiments described in Secs. II.A-F and IV.A-C. There is no impingement of jets in the converging nozzle geometry; rather, the flow in the nozzle is designed so that it gradually converges in the separator channel (see Fig. 48a).

Two configurations are possible for the separator channel. In the first, walls A are used (Fig. 48a), making a channel for which the area increases rapidly as one moves downstream from the nozzle exit. In the second, separator channel filler blocks are used, making the internal walls of the separator channel walls B (Fig. 48b); for this case the channel area is constant at the nozzle exit value to within ±5%.

The nozzle-separator configuration with walls B, Fig. 48a, was constructed for the following theoretical reasons.

(1) Collisions between droplets should occur at very much lower relative velocities in the converging nozzle than in the impact zone of the conventional nozzle separator configurations (e.g., Fig. 24, Sec. II.F.2.b). For operation at $R_F = 37.5$, the liquid velocity at the channel exit is calculated by the methods of Ref. 9 to be 302.7 ft./s. If $\theta = 10$ deg in the configuration of Fig. 24, the relative velocity between a droplet moving at this angle to the channel centerline and one moving parallel to the centerline is $\sim 302.7 \sin 10 \text{ deg} = 52.6$ ft/s.

In the configuration of Fig. 48, for $R_F = 37.5$, it is assumed, for the moment, that the random velocities of droplets at the nozzle exit are zero. With this assumption, the relative velocity, in the converging direction, of two droplets at the nozzle exit one mean free path apart (based on the largest droplets expected to exist at the nozzle exit as calculated by the methods of Ref. 9) is 0.365 ft/s. This value is so low that random droplet velocities will probably be important in determining the typical collision velocity of two droplets.

For the configuration of Fig. 24, using the relative velocity of 52.6 ft/s calculated above and the diameter of the largest droplets expected to exist at the nozzle exit, the parameter $\sigma_\ell / (D\rho_\ell u_r^2)$ is equal to 1.545×10^{-3} (u_r is the relative velocity between the two colliding droplets).

For the same-diameter droplets, same R_F, etc., using the relative velocity estimated for the converging nozzle case (0.365 ft/s), $\sigma_\ell / D\rho_\ell u_r^2$) is equal to 32.3.

The random droplet velocities at the nozzle exit may well cause the effective mean value of $\sigma_\ell / (D\rho_\ell u_r^2)$ to be considerably smaller than 32.3, though probably not nearly as small as the value given above for the configuration of Fig. 24. From the criterion of Ref. 12, one can roughly estimate that, if $\sigma_\ell / (D\rho_\ell u_r^2) < 0.042$, the droplets will disrupt on impact, if $0.042 < \sigma_\ell / (D\rho_\ell u_r^2) < 0.125$, the droplets have a significant chance of coalescence on impact, and, if $0.125 < \sigma_\ell / (D\rho_\ell u_r^2)$, the droplets will rebound (without disruption or coalescence) on impact. These criteria are taken from those given in Ref. 12, modified for the case of droplets of equal size. From the above discussion, it appears that for the case of the geometry of Fig. 24 (Sec. II.F.2.b) the droplets will be reduced in size considerably in the central zone of concentrated liquid because of the violence of the collisions. For the case of the converging nozzle, it appears that the droplets will not be reduced in size by collision (unless the random droplet velocity at the nozzle exit is greater than 10 ft/s), and even in this latter case, the reduction in droplet size should not approach that taking place in the impinging-jet separator geometry of Fig. 24. On the assumption that the mean droplet size for the converging nozzle separator does remain relatively large (i.e., does not decrease substantially below its nozzle exit value), as the liquid flow tends to concentrate in the separator channel, the gas should be able to escape relatively easily from the converging liquid flow without carrying much of the liquid with it. (The force exerted by the gas on a droplet per unit droplet mass varies with droplet diameter as D^{-1} to D^{-2}, depending on the Reynolds number of the gas flow around the droplet.)

(2) The "second centrifugal force effect" (see Sec. II.6.G.b) should aid in the separation process for droplets near the walls B (Fig. 47(a)). This is less effective for droplets closer to the channel centerline (going to zero for droplets on the centerline), but at least it is present to some extent, whereas it is totally absent in the separators discussed in Sec. II.A-F and IV.A-C.

(3) The converging nozzle separator has, because of the divergence of the channel shown in Fig. 48(b), an effectively larger area for the gas to escape from the liquid flow in the nozzle jet. The converging nozzle separator has an average effective gas escape area of approximately 1.33 times that of configurations similar to that of Fig. 24. However, it is perhaps more important that the local value of this ratio approaches 2 near the point where the liquid flow is most concentrated. This difference should tend to make R_B for a given R_A less for the converging nozzle than for configurations similar to that of Fig. 24.

Owing to program limitations, data was taken only without the filler blocks in place (Fig. 48a). Under these conditions, the best mass flow probe profile obtained indicated very poor separator performance. The maximum liquid mass flux observed in the profiles was only approximately 1.5 times that at the nozzle exit. Configurations similar to those of Fig. 24 routinely gave maximum liquid mass fluxes (at the optimum x-position) of 4.6 to 5.7 times those at the nozzle exits (see Sec. II.D).

The reason for this very poor performance is almost certainly due to the fact that the two-phase jet in the region where one is trying to concentrate the liquid flow is flowing in a channel of rapidly increasing area. First, there is the tendency of the gas flow to expand to fill the available area (carrying some of the liquid with it); see Sec. IV.C.4. However, the author believes the most important cause of said poor separator performance is as follows. The edges of the liquid jet (with so much area available) tend to pump (by entrainment) so much gas and air out of the separator channel that for some regions of the channel the pressure falls below atmospheric. (There is a parallel with the jet flowing between the knife-edge blocks; see Sec. II.F.2.b and Fig. 24.) Hence, air is sucked into the separator channel near walls A (this has been experimentally observed). A strong gas velocity shear thus exists in some regions of the channel from the centerline (Fig. 48a) to the regions near the walls. Over this distance the gas velocity changes from approximately +300 ft/s (velocities in the direction from the channel inlet to the channel exit being taken as positive) to some negative value. This high gas velocity shear is believed by the author to produce many violent collisions of water droplets, thus reducing the mean droplet

size in these regions. The smaller droplets are much more likely to follow the gas flow and not reach the zone of concentrated liquid (see Sec. III.A.1).

Tests with the separator channel filler blocks in place are believed to be very important, and should be given high priority if H_2O-N_2 separator tests are resumed.

V. SOME POSSIBLE HIGH-PERFORMANCE SEPARATOR CONFIGURATIONS

A. Four-Nozzle Impinging-Jet Separator

This configuration (Fig. 49) was mentioned briefly in Section II.H and uses four nozzles of the type used in the experiments discussed in Sections II.A-F and IV.A-C. In Fig. 49, the separator structure is simplified and the flow patterns idealized after the fashion of Figs. 5 and 8, Section II.C, for clarity. View (a) is drawn as if the top wall were removed and view (b) as if the right side wall were removed. In Section D-D, nothing behind the section plane is shown.

In the four-nozzle separator, the liquid-gas flow passes through two shock waves in succession, thereby allowing the possibility for a greater concentration of liquid flux than with a two-nozzle separator, in which the flow passes through only one shock wave. A water flow streamline is followed through an idealized flow pattern in Fig. 49. The steamline leaves the nozzle exit at point A and passes through the first shock wave at B and the second shock wave at C, downstream of which it is parallel to the channel centerline.

B. Annular Nozzle Separator

A possible annular separator configuration is sketched in section in Fig. 50. The separator is axisymmetric. The flow pattern is idealized after the fashion of Figs. 5 and 8, Section II.C, to simplify the drawing. For the same reason, only the surfaces immediately adjacent to the flow are shown in Fig. 50.

A "channel centerpiece" is shown in Fig. 50. Experimental work would be necessary to show whether best separator performance is achieved with or without this piece.

The idealized separation process of this nozzle is as follows. The "flow element" (Fig. 50b), part of which moves along the liquid flow streamline AB, is considered. This element is ring-shaped, but with a nearly rectangular cross section, as sketched. As the element moves from A to B, dimension "a" will increase somewhat because of the divergence of the nozzle walls upstream of the exit, but this is far overshadowed by a decrease in dimension "b." Hence, a large increase in liquid flux would occur as the flow element moves from A to B. A second increase of the liquid flux occurs as the flow element passes through the shock wave at point B. Since there are two successive processes, each increasing the liquid flux, such a separator offers the potential for higher performance than a two-nozzle separator, where only one such process takes place.

A further possible advantage of the annular nozzle separator is that there are no regions where jets from two nozzles impinge. In both the two-nozzle and four-nozzle separators, the flow in such regions has shown a strong tendency to spread in the direction parallel to the plane of impact. This spreading results in the concentrated liquid flux in these regions impacting with considerable force on the walls of the separator channel, thereby probably increasing friction losses. This type of friction loss should not occur in the annular nozzle separator.

VI. RECOMMENDATIONS FOR FURTHER WORK

The following recommendations are made for future work:

(1) Tests with the converging nozzle with the filler blocks in place and possibly with P_{NI} = 105-125 psia (see Section IV.B).

(2) Tests of a two-nozzle separator using the standard nozzles with the 1.586-in. edges of the nozzle exits adjacent (see Section III.B).

(3) Further tests of the four-nozzle separator (see Section V.A).

(4) Tests of the feasibility of returning the liquid flow bypassing the main capture slot to the nozzle inlet (see Sections II.H.4 and IV.A).

(5) Construction and testing of the annular nozzle separator (see Section V.B).

(6) Study of the two-phase shock wave process occurring in impinging-jet separators. This would involve both experimental and theoretical work. Some suggested experiments are:

(a) The taking of high-resolution water mass flux and static pressure profiles closer to the nozzle exits than has previously been done (in particular, upstream of the shock wave zone).

(b) The taking of gas velocity profiles at various locations in separators.

(c) The measurement of droplet size distributions at various locations in separators; the variation across the "shock wave" would be of major interest.

(d) The measurement of droplet random velocity distributions at various locations in separators; again, the variation across the "shock wave" would be of major interest.

Tentative theoretical results from which further investigation might proceed are given briefly below.

(a) From a fairly detailed consideration of the shock wave process (allowing for dissipative processes in the shock wave), no fundamental reason can be seen why the concentration of liquid flux across a single shock wave cannot be considerably greater than 4. This is in contradiction to the simple theory predicting a flux ratio of 4 (see Section II.D). The theory leading to the latter result did not consider any dissipative processes in the shock wave.

(b) From simplified calculations, it appears that a typical two-phase shock wave may require a substantial thickness (0.2 in. or more) to achieve the maximum possible increase in liquid flux. The ratio of this thickness to the separator channel dimensions perpendicular to the shock wave may be of substantial importance in determining the performance of the separator.

(c) There are indications that the maximum ratio of liquid flux across the shock wave (if the wave is allowed to attain the full thickness of 0.2 in. or more mentioned above) is controlled, to a substantial degree, by the ratio of the components of the gas and liquid velocities perpendicular to the shock zone and just upstream of it.

(7) Additional investigation of the variation of V_{jn} with P_{NE} (see Sections II.F.2.b and c).

(8) Additional research should be done on the design of the capture slot (see discussion of Section II.F.2.b).

VII. CONCLUSIONS

The estimated efficiency of a Li-Cs cycle employing an impinging-jet separator similar to the best tested to date (April 15, 1972) is just barely positive: well under 1% (see Fig. 37, Sec. IV.A, and related discussion). Let us assume that the advantages produced by the use of a centerplate (Sec. IV.A) and louvres (Sec. IV.B, particularly Fig. 42) in a separator produce increases in the estimated Li-Cs cycle efficiency which are additive. If this is so, a Li-Cs cycle employing a separator using both a centerplate and louvres, can be roughly estimated from Fig. 37, Sec. IV.A, and related discussion and Fig. 42, Sec. IV.B, to have an efficiency of approximately 2.5%. A surface separator cycle operating under similar conditions has been estimated to yield a cycle efficiency of approximately 7.5% (see Sec. II.H.5). Summing up, the estimated efficiencies of Li-Cs cycles using impinging-jet separators similar to the best tested to date (April 15, 1972) are much inferior to those of similar cycles using surface separators.

Despite the poor relative showing of (a very limited series of) impinging-jet separators discussed in the above paragraph, the possibility of greatly reducing the separator velocity loss by the use of a well-designed impinging-jet separator in place of a surface separator is believed by the author to be very likely (see graphs of the z-values of the two types of separators given in Figs. 27 and 28, and discussion of Sec. II.G.1-5.

Large improvements in estimated Li-Cs cycle efficiency using impinging-jet separators could be obtained if the liquid bypassing the main capture slot could be returned to the nozzle inlet (without pumping); see Fig. 32, Sec. II.H.4-5, Fig. 37, and Sec. IV.A.

Further, the author believes that large improvements in impinging-jet separator performance (over those separators which have been tested) could be obtained with possible advanced separators such as a four-nozzle separator (Sec. V.A), perhaps the converging nozzle separator (Sec. IV.D), or an annular-nozzle separator (Sec. V.B). Also, many other lines of attack for the improvement of impinging-jet separator performance outlined in this paper may give smaller gains in separator performance.

Lastly, it may turn out that performance better than either an all-surface separator system or an all impinging-jet separator system may be achieved by combining the two systems. In particular, an impinging-jet separator followed by a relatively small surface separator (with correspondingly small surface friction losses) might prove to be the best system.

Summing up, it is believed that the use of a well-designed impinging-jet (or combination) separator system offers a definite possibility of increasing the efficiency of, for example, a Li-Cs space power system from approximately 7% (with a surface-separator system) to as high as 10% (see Sec I.E). In the same section, it is pointed out that if high-performance impinging-jet separators can be developed, considerable increases can be made in the efficiencies of ground-based liquid-metal MHD power plants. Such increases are well worth working toward.

NOMENCLATURE

A_1	internal dimension between the diverging walls at the rectangular exit of a nozzle; see Sec. III.B and Fig. 33
A_R	defined by Eq. (27), Sec. III.B.
A'_R	ratio between separator channel area and nozzle exit area
a	(1) see Sec. V.B, Fig. 50b, and associated discussion (2) see Sec. II.G.3
B_1	internal dimension between the parallel walls at the rectangular exit of a nozzle; see Sec. III.B and Fig. 33
b	see Sec. V.B, Fig. 50b and associated discussion
C_D	drag coefficient for a sphere
C_{pg}	specific heat of gas at constant pressure
$C_{p\ell}$	specific heat of liquid at constant pressure
c	isothermal speed of sound in a liquid-gas mixture, see Eq. (1), Sec. I.E.2
D	(1) droplet diameter in general (2) maximum droplet diameter estimated to exist at nozzle exit; usually estimated by the methods of Ref. 9
D_c	see Sec. III.A.2, discussion following Eq. (22)
F_L	see Sec. III.A.2, Eqs. (19)-(22) and associated discussion
f( )	general function
f_ℓ	see Sec. III.A.2, Eq. (17) and associated discussion
G	gap between tips of knife edge blocks; see Secs. II.B and II.C.1

G_1, G_2, G_3, etc.	see Sec. III.A.1, Eq. (12) and associated discussion
g( )	general function
H	height of two nozzle separator channel (height is the dimension parallel to the plane of impact of the two jets and roughly perpendicular to the direction of flow)
h( )	general function
K_g	thermal conductivity of gas
K_ℓ	thermal conductivity of liquid
L	(1) length of louvres, see Sec. IV.B, Fig. 43 (2) length of surface separator (measured along surface) from nozzle exit to primary capture slot
M	(1) $= V_1/c$; see Sec. I.E.2 (2) Mach number in general
m_g	gas mass flow rate through separator system
m_ℓ	liquid mass flow rate through separator system
P	pressure in general
P_1	pressure
P_{NE}	pressure at nozzle exit
P_{NE1}, P_{NE2}, etc.	particular values of P_{NE} chosen to produce surfaces of the type shown in Fig. 19, Sec. II.F.2.a; see discussion associated with said figure
P_{NI}	pressure at nozzle inlet
$P_{NOZZLE\ INLET}$	$= P_{NI}$
R	can refer to any of the quantities $R_{\rho 1}$, R_{v1}, R_{m1}, $R_{\rho 2}$, R_{v2}, R_{m2}
R_1	can refer to any of the quantities $R_{\rho 1}$, R_{v1}, R_{m1}

R_2	can refer to any of the quantities $R_{\rho 2}$, R_{v2}, R_{m2}
R_A	ratio of total nozzle exit area to area of capture slot (also employed when no capture slot is used, but the performance of the separator in question, if a capture slot giving a certain R_A were to be put in place, is estimated from mass flow probe profiles)
R_B	fraction of liquid mass flow bypassing the main capture slot (the note for R_A also applies to R_B)
R_{BK}	R_B for knife-edge separator tests
R_{BL}	R_B for louvre separator tests
$R_{B,\min}$	minimum value of R_B obtainable by varying x for fixed values of R_F, G and θ
R_F	ratio of liquid mass flow rate to gas mass flow rate in separator
R_m	see discussion in Sec. III.B, just before Eq. (23)
R_{m1}	defined by Eq. (25), Sec. III.B
R_{m2}	defined by Eq. (29), Sec. III.B
R_v	see discussion in Sec. III.B just before Eq. (23)
R'_v	ratio between gas velocity and liquid velocity at nozzle exit
R_{v1}	defined by Eq. (24), Sec. III.B
R_{v2}	defined by Eq. (28), Sec. III.B
R_{x1}, R_{x2}	refer to quantities with x = ρ, v or m
R_ρ	see discussion in Sec. III.B, just before Eq. (23)
$R_{\rho 1}$	defined by Eq. (23), Sec. III.B
$R_{\rho 2}$	defined by Eq. (26), Sec. III.B
$R_{\rho n}$, R_{vn}, R_{mn}	refer to quantities with n = 1 or 2

Re_L	Reynolds number based on ρ_ℓ, μ_ℓ, length of louvre L, and mean liquid velocity through the channel between two adjacent louvres
r	radius of curvature of separator channel
r_a	ratio of volume occupied by gas to that occupied by liquid (a local quantity)
T_{NI}	temperature at nozzle inlet
u	(1) relative velocity of liquid droplet through gas (2) general velocity
u_g	scalar gas velocity
u_ℓ	scalar liquid velocity
u_r	relative velocity between two colliding droplets
$\vec{u}_{gc}$	vector velocity of gas in separator channel
$\vec{u}_{\ell c}$	vector velocity of liquid in separator channel
V_l	(1) liquid velocity at nozzle exit (2) liquid velocity
V_i	$= V_{isentropic}$
$V_{isentropic}$	calculated mean velocity of liquid-gas jet at nozzle exit for a given set of conditions at the nozzle inlet, a given nozzle exit pressure and with isentropic flow in the nozzle; often compared with V_{jet} values measured for the same nozzle inlet conditions and with the same or different nozzle exit pressure
V_j	$= V_{jet}$
V_{jet}	measured mean velocity of liquid-gas jet at nozzle exit or at capture slot
V_{jn}	see Sec. II. F. 2. a
V_{jn1}, V_{jn2}, etc.	particular constant values of V_{jn} chosen to produce surfaces of the type shown in Fig. 19, Sec. II. F. 2. a; see discussion associated with said figure

v	(1) absolute velocity of liquid droplet (2) see Sec. III.A.1, Eq. (9) and discussion immediately following
$v_{i\perp}$	component perpendicular to plane of plate of velocity of impingement of liquid droplet on plate in idealized model of Sec. II.G.6.c
$v_{\ell b}$	liquid velocity parallel to wall and outside boundary layer
$v_{\ell g}$	magnitude of vector velocity difference between a droplet and the surrounding gas
v_0	see Sec. III.A.1, Eq. (9) and discussion immediately following
$v_{r\perp}$	component perpendicular to plane of plate of velocity of rebound of liquid droplet from plate in the idealized model of Sec. II.G.6.c
W	(1) width of two-nozzle separator channel (width is the dimension perpendicular to the plane of impact of the two nozzle jets) (2) spacing between louvres, see Sec. IV.B, Fig. 43
x	distance from nozzle exits to knife-edge tips; see Fig. 6, Sec. II.C.1
x_{GI}	defined in Fig. 6, Sec. II.C.1
x_Q	see Fig. 8, Sec. II.C.1, and associated discussion
y	(1) in a two nozzle separator, the distance of a mass flow probe from the plane of impingement of the two nozzle jets (2) somewhat similar to (1); used in two-nozzle separator mass flow measurements to define the position of the probe with respect to the plane of impingement of the two-nozzle jets; y increases continuously as one moves the probe from one wall of the channel through

the plane of impingement. The origin of y is arbitrary.

(3) $= 1 - (1 - z)(1 - R_B)$

(4) see Sec. III.A.1, Eq. (9) and discussion immediately following

y_s — y (3) for surface separator operation

y_{so} — optimized value of y_s; see Sec. II.G.3

Z_m — x/x_{GI} at x-position where $R_{B,min}$ occurs

z — for a given separator configuration, and given conditions at the nozzle inlet (R_F, P_{NI} and liquid temperature), z is defined as the mean jet velocity obtained for nozzle-only operation at the same nozzle inlet conditions (corrected to operation at $\theta = 10$ deg) [1], less the mean velocity of the capture slot jet (whether or not there is a physical capture slot or probe profile data is used) in separator operation [2], with said difference divided by (1); that is,

$$z = \frac{[1] - [2]}{[1]}$$

z_K — z for knife-edge separator tests

z_L — z for louvre separator tests

z_R — average fractional velocity loss (fraction of liquid velocity at the nozzle exit) of the liquid returned to the main flow by the louvres; see Sec. IV.B, Eq. (30) and associated discussion

z_s — z for surface separator operation

z_{so} — optimized value of z_s; see Sec. II.G.3

α

(1) angle between nozzle centerline and channel centerline; see Fig. 4, Sec. I.E.2

(2) angle of impact of droplet on louvres; see Sec. IV.B, Fig. 43, and associated discussion

	(3) see Sec. IV.C, Fig. 45, and associated discussion
β	(1) see Sec. IV.C, Fig. 45, and associated discussion (2) angle of louvres with respect to louvre panel; see Sec. IV.B, Fig. 43 (3) nozzle divergence angle; see Fig. 4, Sec. I.E.2
γ	half of the nozzle divergence angle; = $\beta(3)/2$; see Sec. III.B
η	(1) see Sec. III.A.1, Eq. (9) (2) MHD power generation cycle efficiency
θ	angle between nozzle centerline and channel centerline [= $\alpha(1)$]
λ	droplet mean free path
μ_g	viscosity of gas
μ_ℓ	viscosity of liquid
ρ_1	concentration of liquid (lbm/ft^3) upstream of shock wave in the idealized model of Sec. II.G.6.c
ρ_2	concentration of liquid (lbm/ft^3) downstream of shock wave in idealized model of Sec. II.G.6.c
ρ_g	gas density
ρ_ℓ	liquid density
σ_ℓ	liquid surface tension
τ_w	fluid shear stress at wall
ϕ	mean angle of impingement of nozzle jet on surface separator surface

REFERENCES

1. Elliott, D. G., et al., "Investigation of a Liquid-Metal Magnetohydrodynamic Power System," paper presented at the 5th Intersociety Energy Conversion Engineering Conference, Las Vegas, Sept. 21-25, 1970.

2. Amend, W. E., and Petrick, M., "Performance of an Efficient 'Low Temperature' Liquid-Metal MHD Power Cycle Suitable for Large Scale Power Production," paper presented at the 5th International Conference on Magnetohydrodynamic Electrical Power Generation, Munich, April 19-23, 1971.

3. Elliott, D., et al., "Liquid MHD Power Conversion," in Supporting Research and Advanced Development, Space Programs Summary 37-32, Vol. IV, Jet Propulsion Laboratory, Pasadena, California, pp. 134-138, April 30, 1965.

4. Cerini, D. J., "Circulation of Liquids for MHD Electric Power Generation," Electricity from MHD, Vol. III, pp. 2019-2033, 1968.

5. Amend, W., et al., "Performance of a Quasi-Ericsson Two-phase Two-component Liquid Metal MHD Power Cycle," paper presented at the 11th Symposium on Engineering Aspects of Magnetohydrodynamics, California Institute of Technology, Pasadena, California, March 24-26, 1970, pp. 154-159.

6. Elliott, D., et al., "Liquid MHD Power Conversion," in Supporting Research and Advanced Development, Space Programs Summary 37-27, Vol. IV, Jet Propulsion Laboratory, Pasadena, California, pp. 75-83, June 30, 1964.

7. Elliott, D., et al., "Liquid MHD Power Conversion" in Supporting Research and Advanced Development, Space Programs Summary 37-30, Vol. IV, Jet Propulsion Laboratory, Pasadena, California, pp. 116-119, December 31, 1964.

8. Weinberg, E., and Hays, L. G., Comparison of Liquid-Metal Magnetohydrodynamic Power Conversion Cycles, Technical Report 30-946, Jet Propulsion Laboratory, Pasadena, California, August 15, 1961.

9. Elliott, D. G., and Weinberg, E., Acceleration of Liquids in Two-Phase Nozzles, Technical Report 32-987, Jet Propulsion Laboratory, Pasadena, California, July 1, 1968.

10. Investigation of Supersonic Shock Phenomena in a Two-Phase (Liquid-Gas) Tunnel, Technical Report 32-1096, Jet Propulsion Laboratory, Pasadena, California, March 15, 1967.

11. Klein, E., "Preliminary Results Obtained from Operations of Two-Phase Nozzles with Potassium, Freon-113 and Water," Proceedings, Fifth International Conference on Magnetohydynamic Electric Power Generation, Munich, Germany, pp. 383-398, April 9 - 23, 1971.

12. Gunn, R., "Collision Characteristics of Freely Falling Water Drops," Science, Vol. 150, No. 3697, pp. 695-701, November 5, 1965.

13. Elliott, D., et al., "Liquid MHD Power Conversion," in Supporting Research and Advanced Development, Space Programs Summary 37-25, Vol. IV, Jet Propulsion Laboratory, Pasadena, California, pp. 106-111, Feb. 29, 1964.

14. Jayaratne, O. W., and Mason, B. J., "The Coalescence and Bouncing of Water Drops at an Air-Water Interface," Proc. Roy. Soc. London, Series A, Vol. 280, No. 1383, pp. 545-65, 1964.

15. Elliott, D. G., "Cycle Analysis of a Cesium-Lithium MHD Power System with an Impinging-Jet Separator (Program CYCLE-B), "Jet Propulsion Laboratory, California Institute of Technology, Pasadena, California, June 16, 1969 (unpublished).

16. Weinberg, E., and Hays, L. G., Comparison of Liquid-Metal Magnetohydrodynamic Power Conversion Cycles, Technical Report 32-946, Jet Propulsion Laboratory, Pasadena, California, August 15, 1966.

17. Leva, M., Fluidization, McGraw-Hill, New York, 1959.

18. Brinkman, H. C., "A Calculation of the Viscous Force Exerted by a Flowing Fluid on a Dense Swarm of Particles," Applied Scientific Research, Vol. 1, Series A, pp. 27-34, 1947.

19. Elliott, D. G., private communication, June 1973.

Table 1. Comparison of values for the Li-Cs and H_2O-N_2 cases

Group No.		1	2	3	4	5	6	7
Group	R_F	α	β	W/D	ρ_g/ρ_l	m_g/m_l	μ_g/μ_l *	M
Units	-	deg	deg	-	-	-	-	-
Li-Cs	14	a	b	228	0.00242	0.0714	0.1717	2.08
H_2O-N_2	85.8 37.5 19.1	5-30 ↓	5.4 ↓	329 487 670	0.001141 ↓	0.01165 0.0267 0.0524	0.01545 ↓	2.39 2.24 2.16
Group No.	-	8	9	10	11	12	13	14
Group	R_F	$\frac{\sigma_l}{D\rho_g V_l^2}$	$\frac{\rho_g V_l W}{\mu_g}$	$\frac{1}{r_a + 1}$	$\frac{\rho_l V_l D}{\mu_l}$ *	$\frac{\sigma_l}{D\rho_l V_l^2}$	$\frac{\rho_g V_l D}{\mu_g}$	$\frac{W\rho_g}{D\rho_l}$
Units	-	-	-	-	-	-	-	-
Li-Cs	14	0.0264	5.30×10^5	0.0485	1.663×10^5	6.39×10^{-5}	2330	0.552
H_2O-N_2	85.8 37.5 19.1	0.0485 0.0410 0.0327	4.20×10^5 5.55 7.29	0.1293 0.0600 0.0308	1.73×10^4 1.545 1.475	5.53×10^{-5} 4.68 3.73	1277 1140 1088	0.375 0.555 0.764
Group No.	-	15						
Group	R_F	$\frac{m_l W \rho_g}{m_g D \rho_l}$						
Units	-	-						
Li-Cs	14	7.72						
H_2O-N_2	85.8 37.5 19.1	32.2 20.8 14.61						

[a] The optimum α for the Li-Cs system is undoubtedly covered in the range 5-30 deg used for H_2O-N_2 tests. This optimum α is probably in the range 10-15 deg.

[b] A β of 5.4 deg for H_2O-N_2 tests is simply geometrically similar to β = 5.4 deg for Li-Cs tests, and hence provides perfect simulation of same. The same would apply to α angles (discussed in footnote "a") of, say, 10 deg for the two cases in question. There is no knowledge available showing that 5.4 deg is the optimum angles for β; in fact, later sections of this report show that even the general form of the separator sketched in Fig. 4 is not that which produces the best performance. However, this is not the question at this point. The accuracy of the simulation of Li-Cs separators by H_2O-N_2 separators is the main point.

Table 2. Calculated values for movement of water droplets laterally across separator channel

D, in.	y ($v/v_0 = 0$), in.	y ($v/v_0 = 1/\sqrt{2}$), in.
0.01	52.9	7.20
0.003	8.88	1.655
0.001	1.428	0.337
0.0003	0.158	0.0424
0.0001	0.0188	0.00565

H_2O-N_2

$R_F = 37.5$

$\alpha = 15$ deg

$v_0 = 78.5$ ft/s

P (separator channel) = 14.2 psia

$T_{NI} = 520°$ R

Table 3. Calculations of liquid concentration, momentum flux per unit area perpendicular to channel centerline and velocity perpendicular to centerline, all calculated in separator channel and compared to corresponding values at nozzle exit

Parameter	1		2		3	
	Standard nozzle		Standard nozzle		Square nozzle	
$\theta(°)$	10		15		15	
$\gamma(°)$	2.72		2.72		5.10	
A_R	3.51		3.51		1.0	
	R_{x1}	R_{x2}	R_{x1}	R_{x2}	R_{x1}	R_{x2}
$R_{\rho n}$	0.573	0.346	0.698	0.446	0.500	0.600
R_{vn}	0.724	1.000	0.815	1.000	0.651	1.000
R_{mn}	0.300	0.346	0.461	0.446	0.212	0.600

x = ρ, v or m as noted.

n = 1 or 2 as noted.

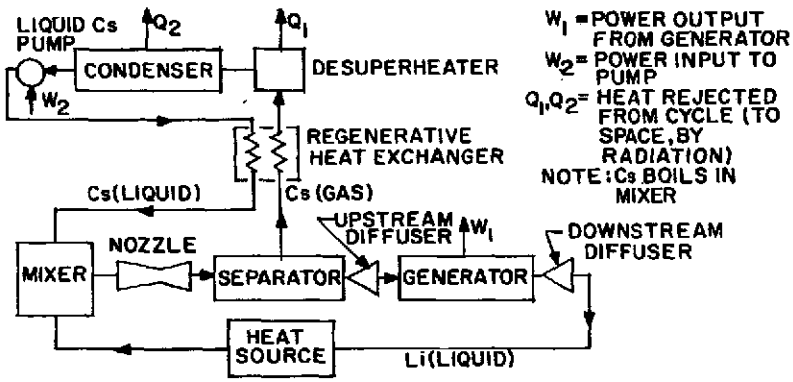

Fig. 1. Typical liquid-metal MHD power cycle for space use, using a condensible vapor to accelerate the liquid (sketch modified from Fig. 1, Ref. 1)

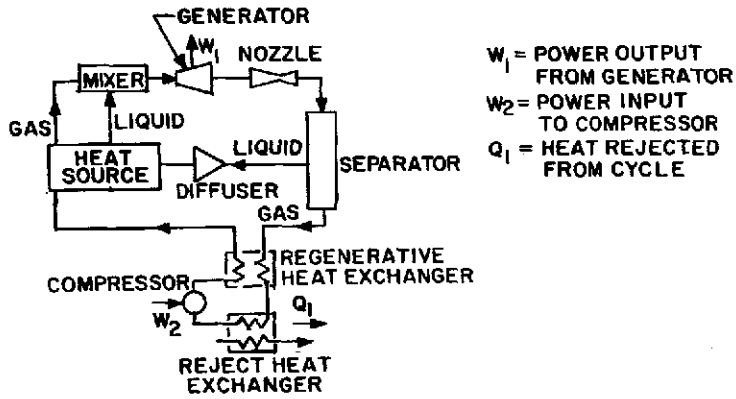

Fig. 2. Typical liquid-metal MHD power cycle for ground-based use using a non-condensible gas (typically He or Ar) to accelerate the liquid (sketch modified from Fig. 1, Ref. 2)

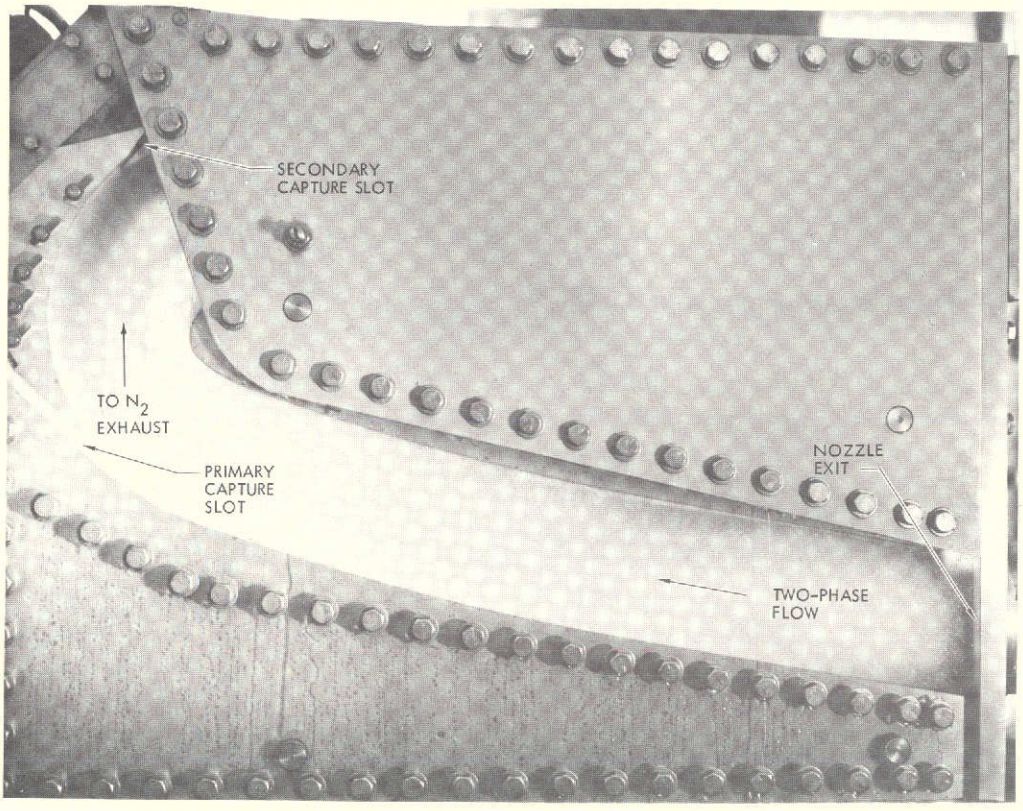

Fig. 3. Surface separator in operation (see text)

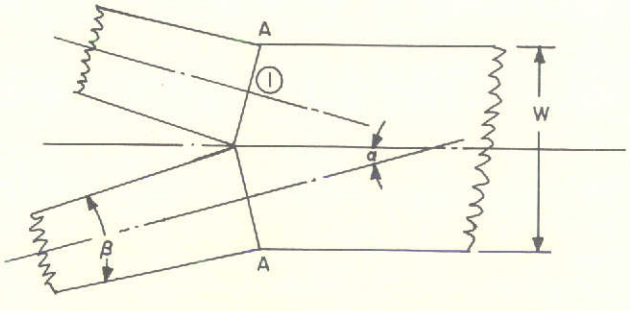

Fig. 4. Sketch for simplified dimensional analysis of impinging-jet separator

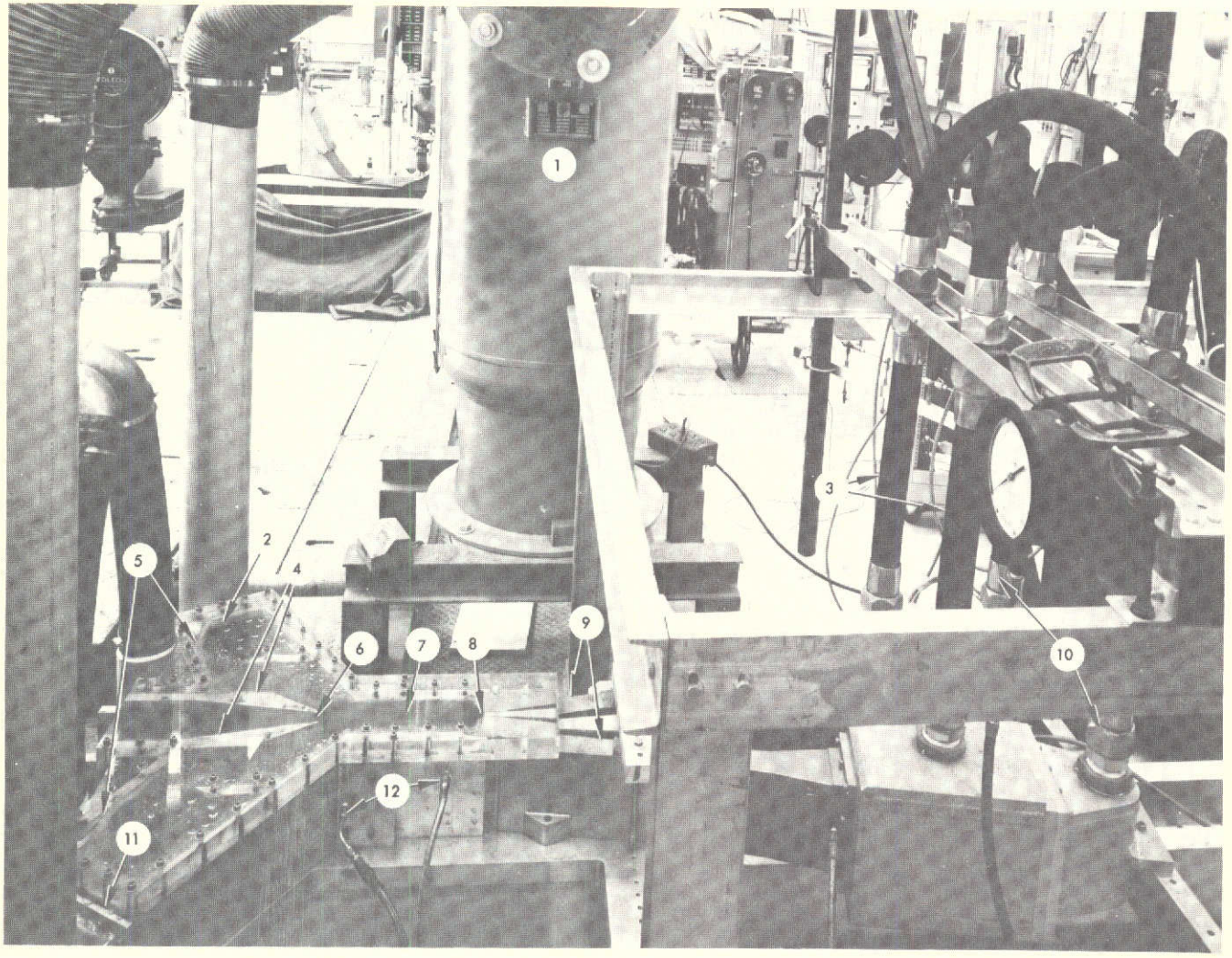

1 WATER SEPARATOR
2 GAS DISCHARGE PORT
3 NITROGEN FEED LINES
4 KNIFE EDGE BLOCKS
5 SECONDARY CAPTURE SLOTS
6 PRIMARY CAPTURE SLOTS
7 SEPARATOR CHANNEL
8 NOZZLE EXITS
9 NOZZLES
10 WATER SUPPLY LINES
11 GAS DISCHARGE PORT
12 STATIC PRESSURE TAPS

Fig. 5. Typical impinging-jet separator experimental test rig

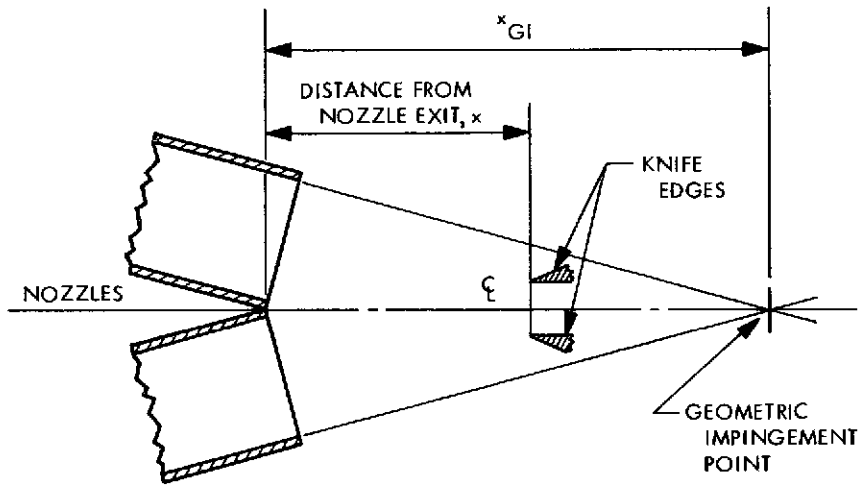

Fig. 6. Sketch defining the distances of the knife-edge tips (capture slot) and the geometric impingement point from the nozzle exit (x and x_{GI}, respectively)

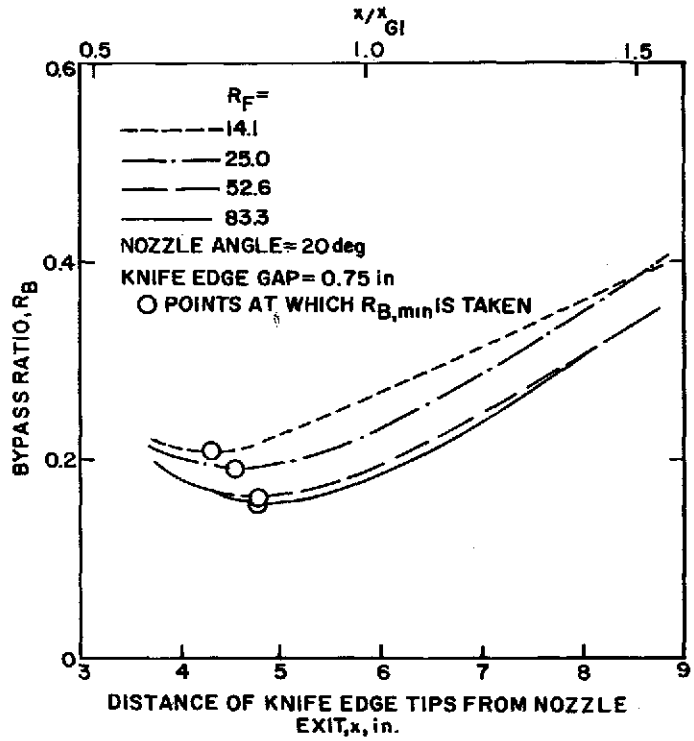

Fig. 7. Bypass ratio vs distance of knife-edge tips from nozzle exit

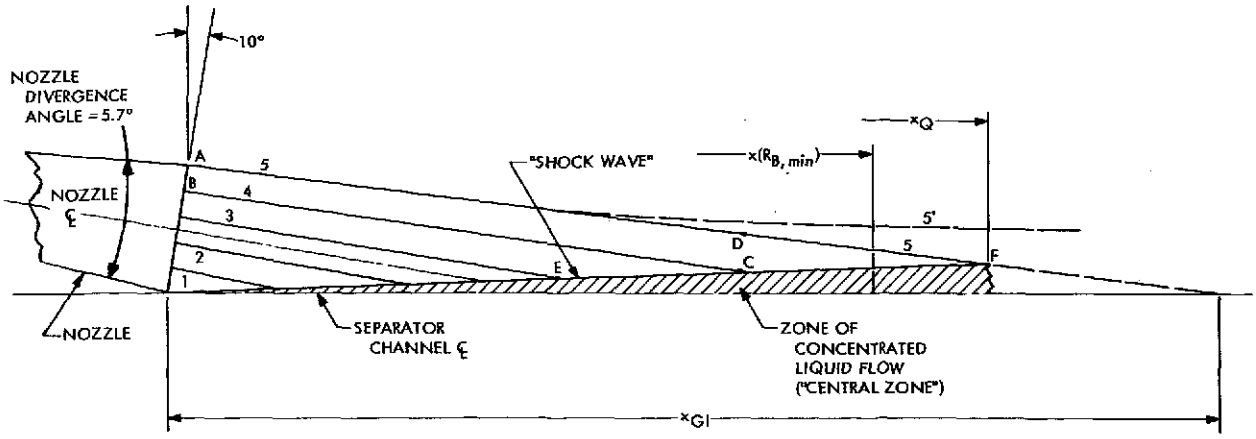

Fig. 8. Sketch used in discussion of some effects of nozzle divergence on separator performance

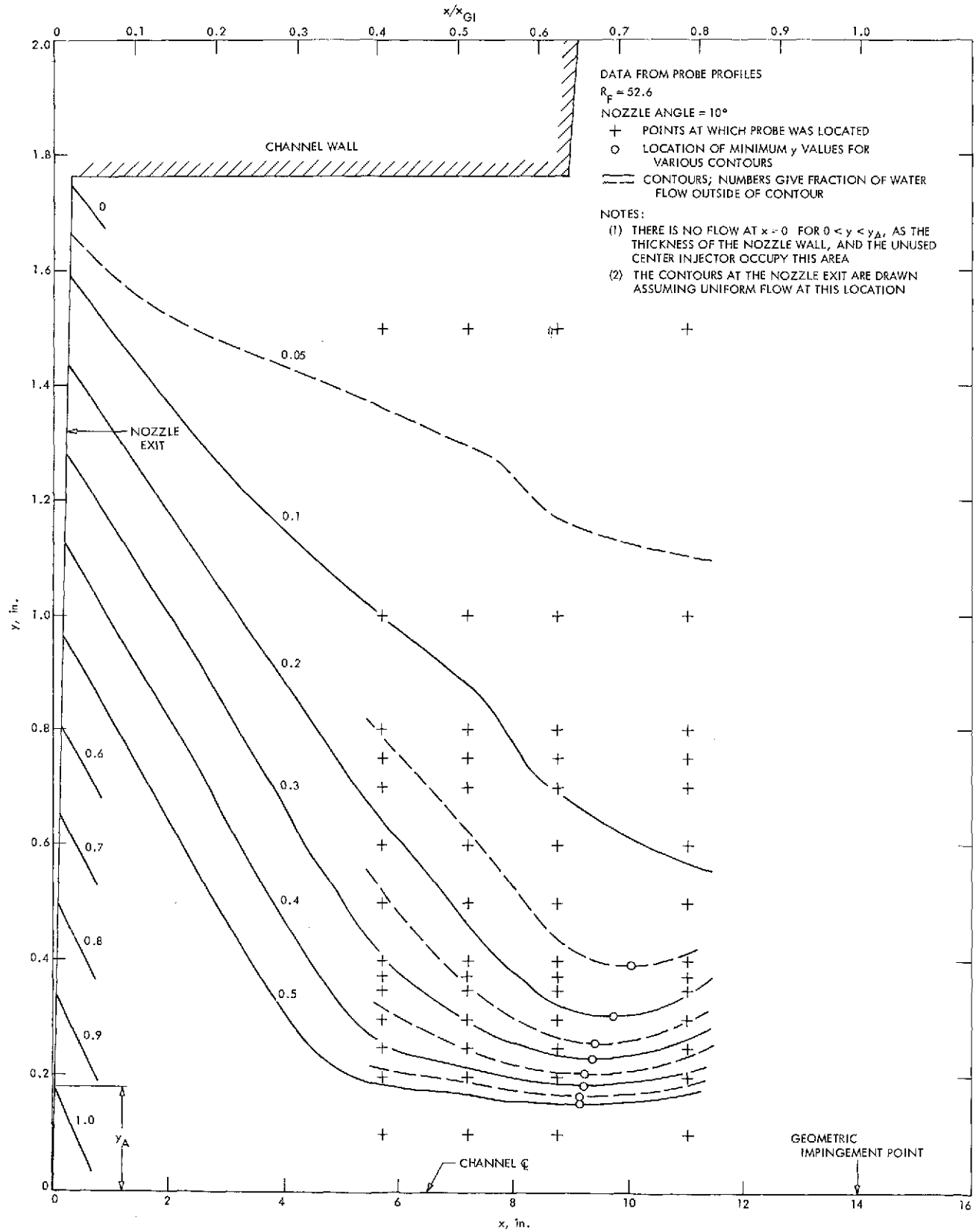

Fig. 9. Typical contours of distribution of water flow in the separator channel (from probe profiles)

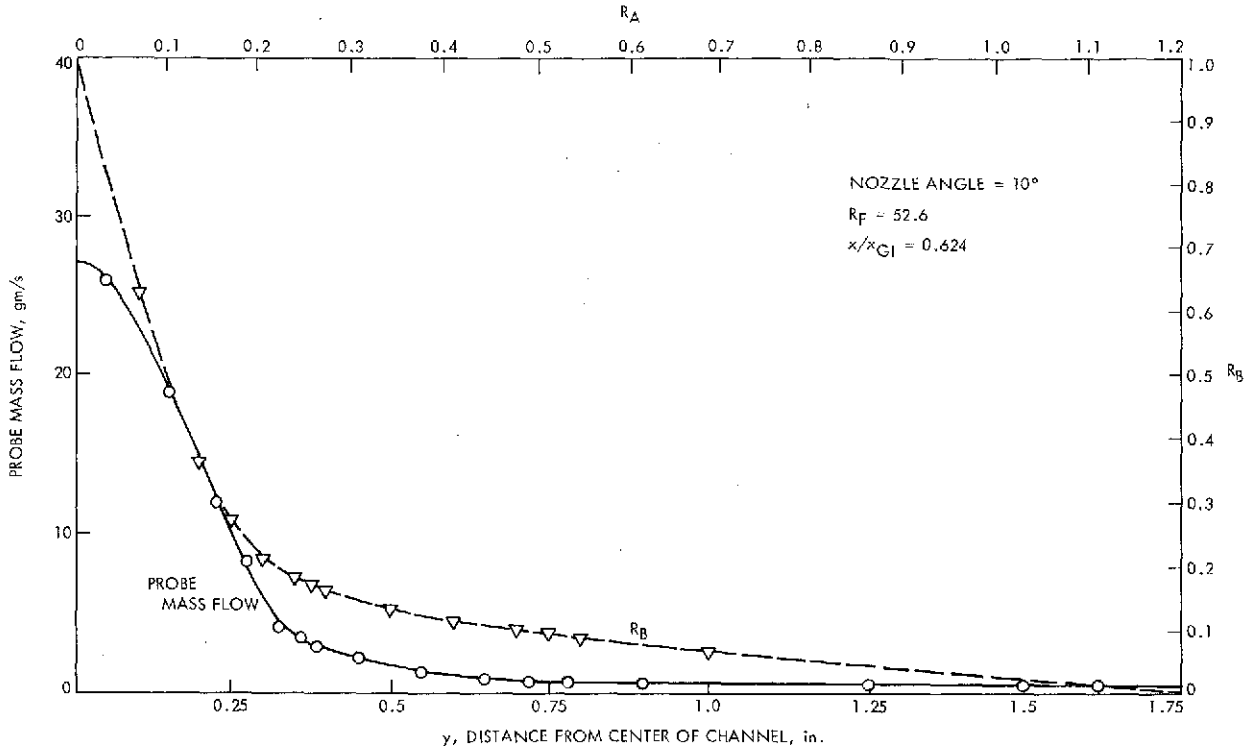

Fig. 10. Typical variation of R_B and probe mass flow with y-position in separator channel

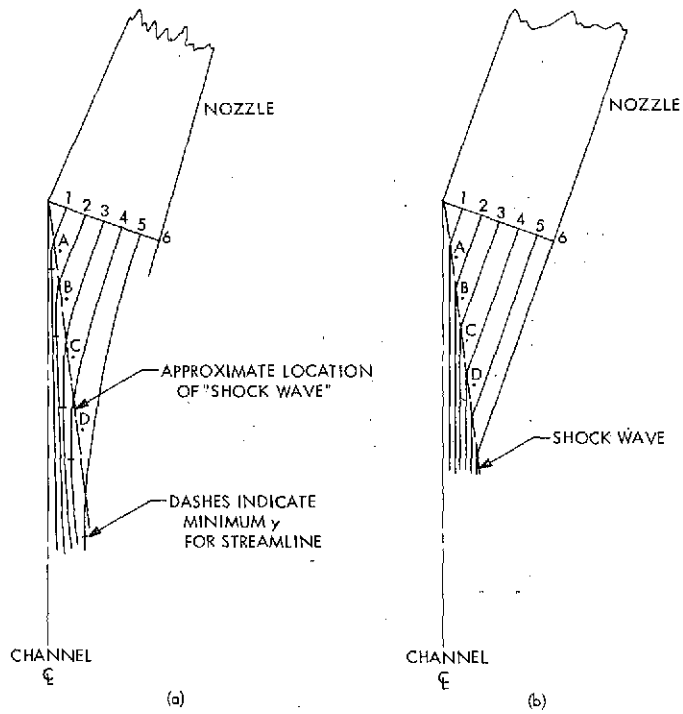

Fig. 11. Sketches of idealized and more realistic liquid droplet particle paths in the separator channel

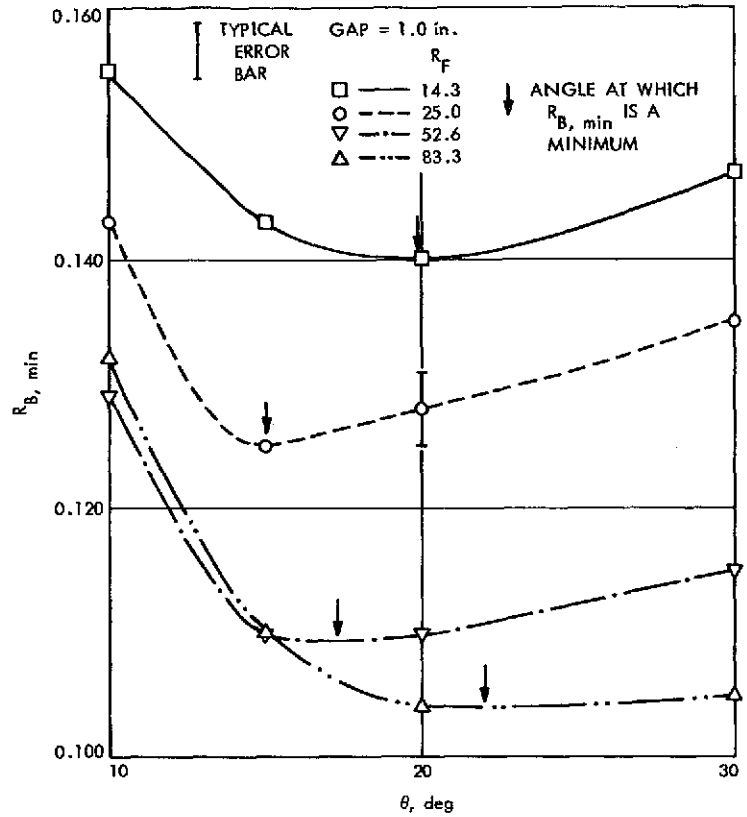

Fig. 12. Variation of $R_{B,\ min}$ with θ and R_F

CURVE A(B)–$R_{B,min}$ VALUES WHICH WOULD OCCUR IF PHENOMENA WHICH INCREASE $R_{B,min}$ WITH DECREASING(INCREASING) θ ONLY WERE PRESENT. CURVE C– ACTUAL $R_{B,min}$ CURVE INCLUDING BOTH TYPES OF PHENOMENA.

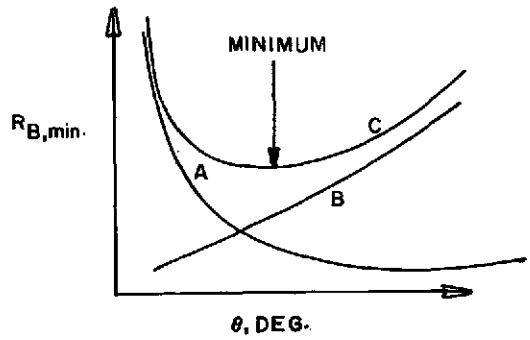

Fig. 13. General form of variation of $R_{B,\ min}$ with θ

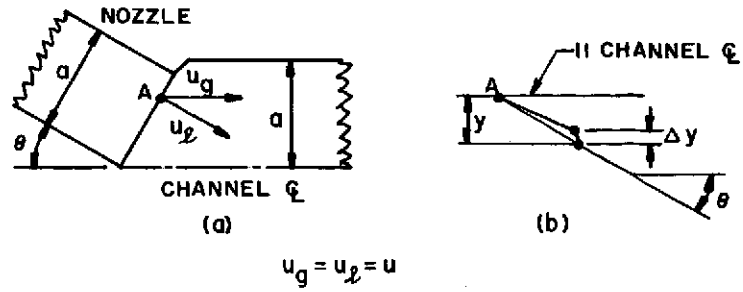

Fig. 14. Sketch for discussion of one cause of increasing $R_{B,\,min}$ with increasing θ (see text)

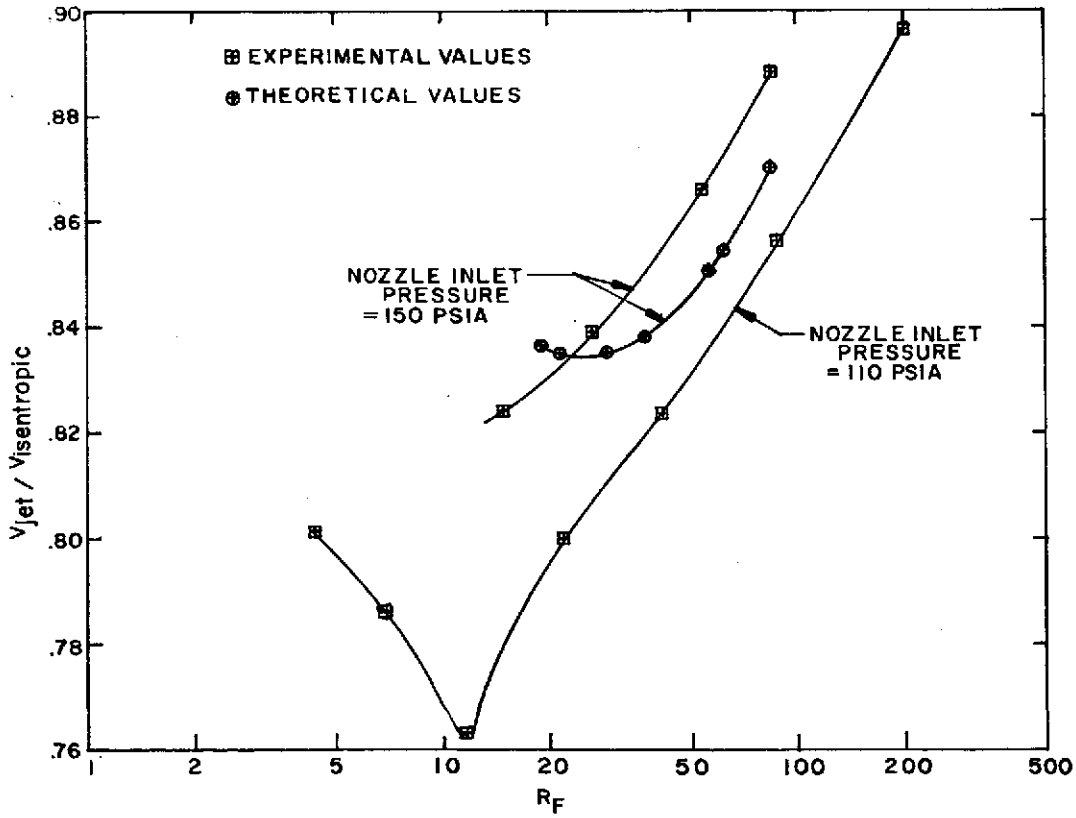

Fig. 15. Calculated and measured values of the ratio of the mean jet velocity at the nozzle exit to the calculated ideal (isentropic) velocity for the same nozzle inlet conditions and nozzle exit pressure

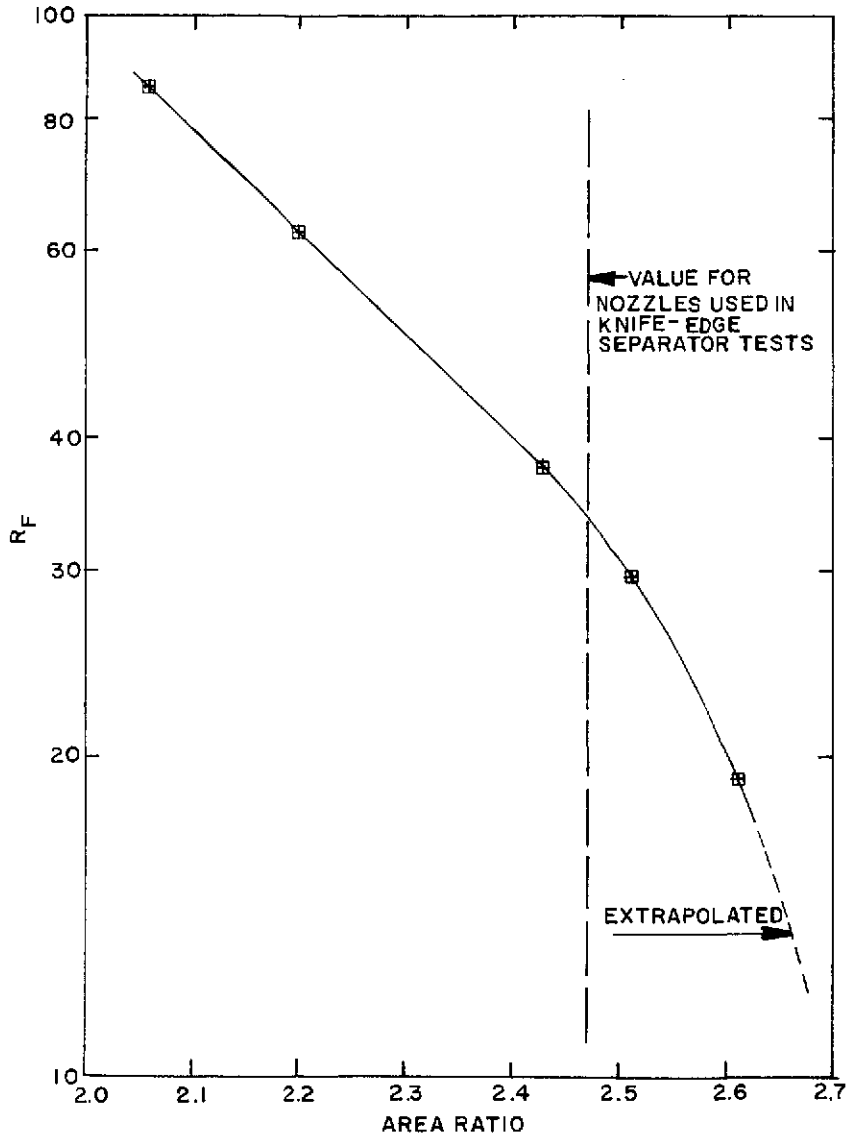

Fig. 16. Calculated values of (nozzle exit area)/(nozzle throat area) as a function of R_F for a given nozzle pressure profile (see text)

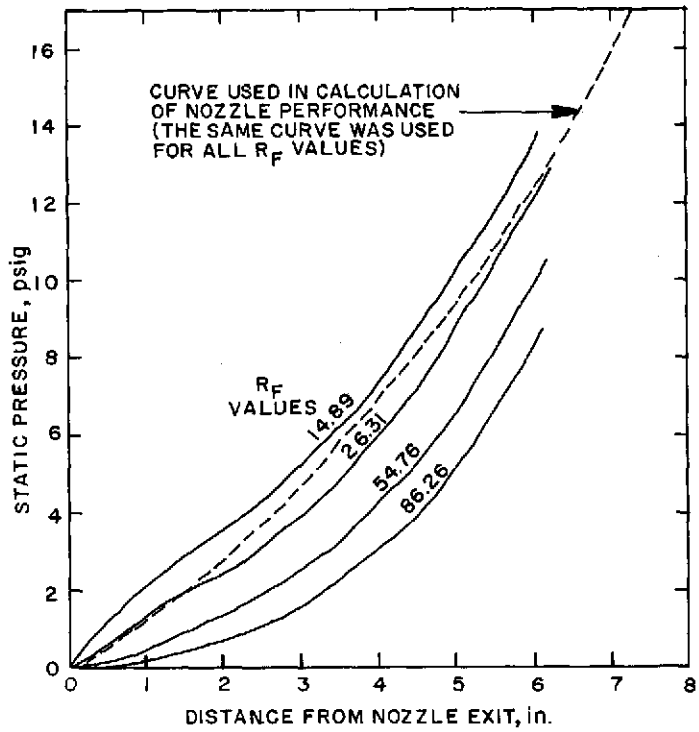

Fig. 17. Plots of experimental values of pressure inside nozzle as a function of distance from nozzle exit (with R_F as a parameter)

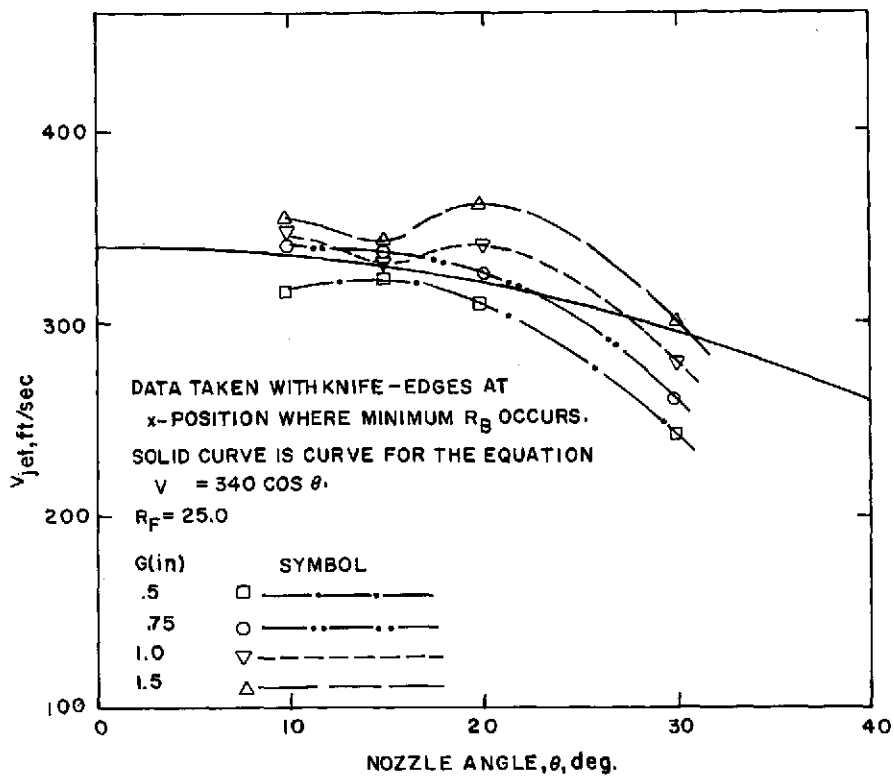

Fig. 18. Variation of V_{jet} with θ and G

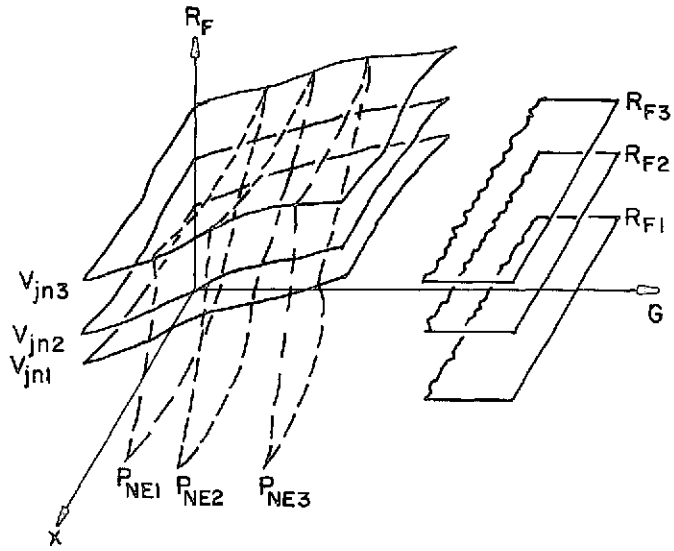

NOTE: THE TRUE SURFACES FOR CONSTANT V_{jn} VALUES AND CONSTANT P_{NE} VALUES BEAR NO RELATION TO THE SIMPLE SURFACES SHOWN IN THIS SKETCH; THE LATTER ILLUSTRATIVE SURFACES WERE SO DRAWN TO SIMPLIFY THE PRESENTATION; THE SHAPES OF THE TRUE SURFACES MAY BE ESTIMATED FROM FIG. 20.

Fig. 19. Nature (see note) of data obtained from the knife-edge separator by variation of x, G and R_F

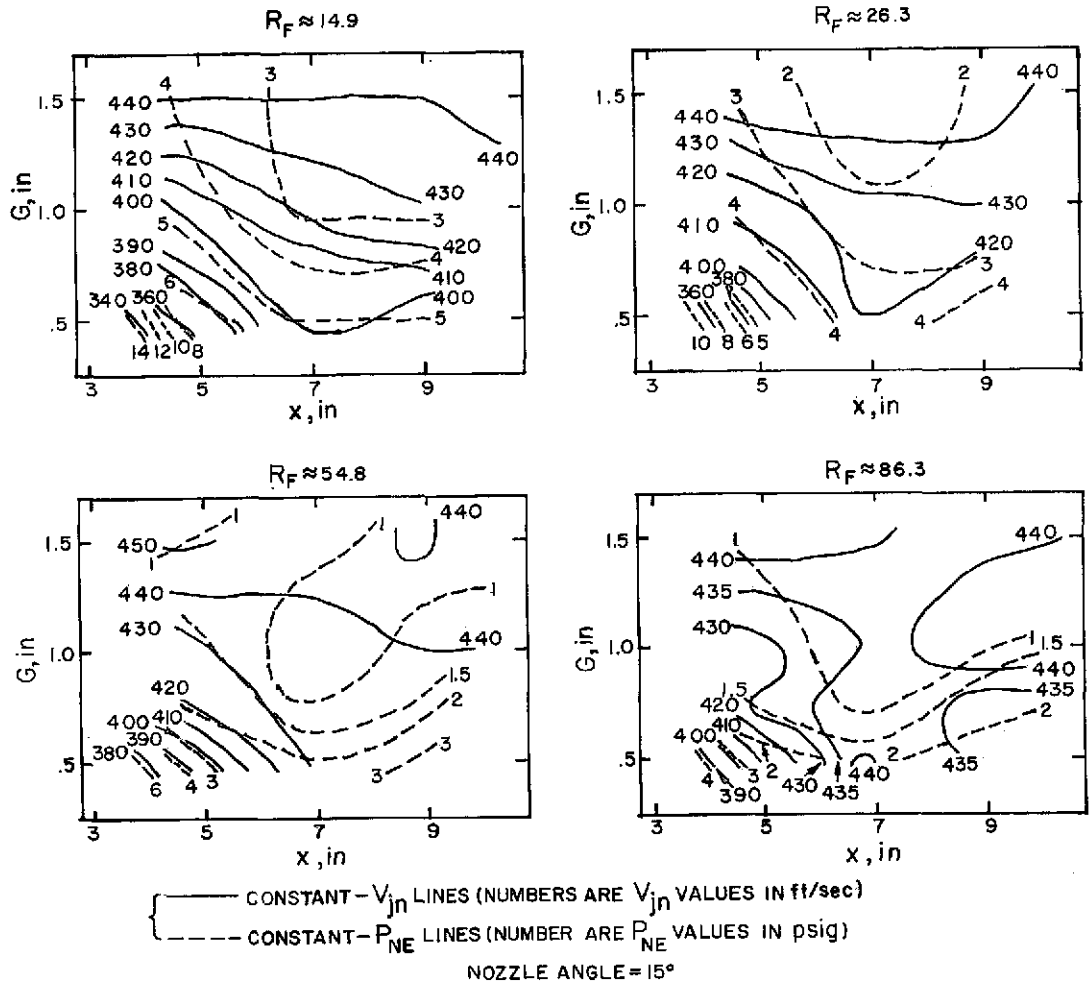

Fig. 20. Constant R_F sections through the 3-dimensional space typified by Fig. 19 for four R_F values. Very simple illustrative surfaces are used in Fig. 19 for the constant $-V_{in}$ and constant P_{NE} surfaces (see caption of Fig. 19 and text); above, sections through the true surfaces are shown

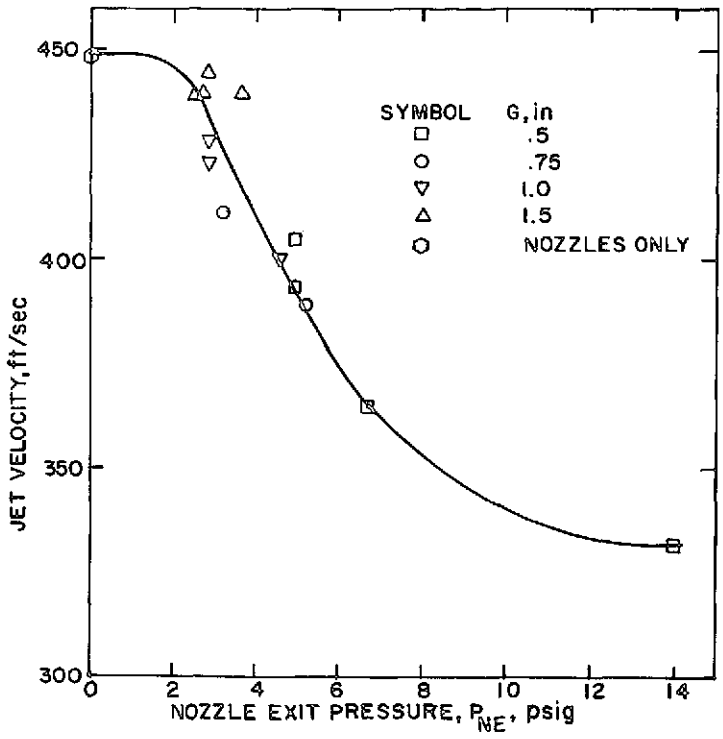

Fig. 21. Plot of jet velocity vs nozzle exit pressure for R_F = 14.9, θ = 15 deg

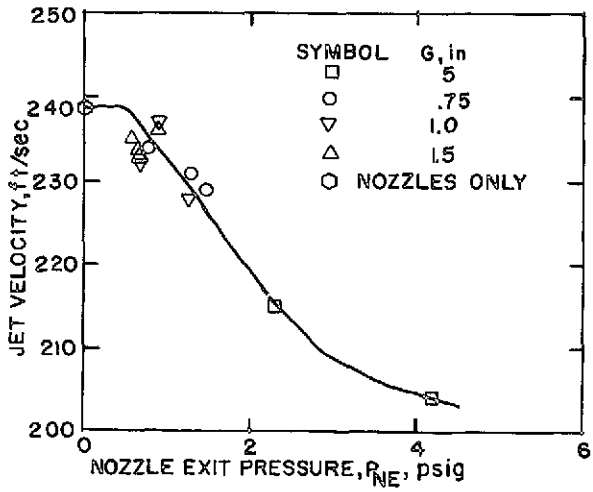

Fig. 22. Plot of jet velocity vs nozzle exit pressure for R_F = 86.3, θ = 15 deg

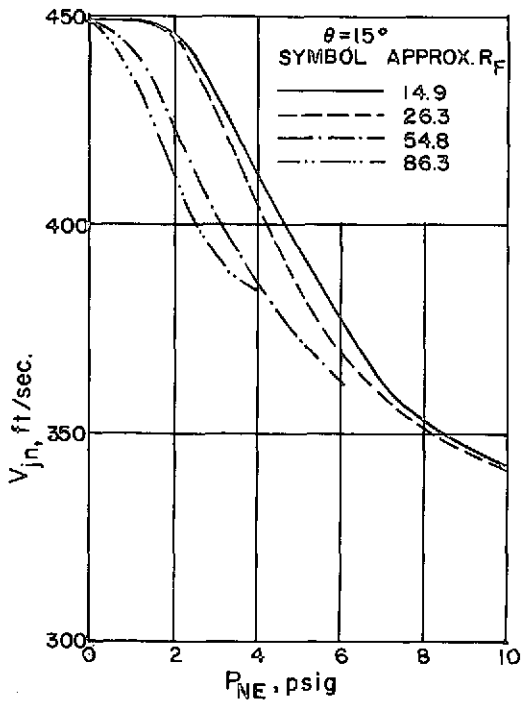

Fig. 23. Variation of V_{jn} with P_{NE} for four R_F values

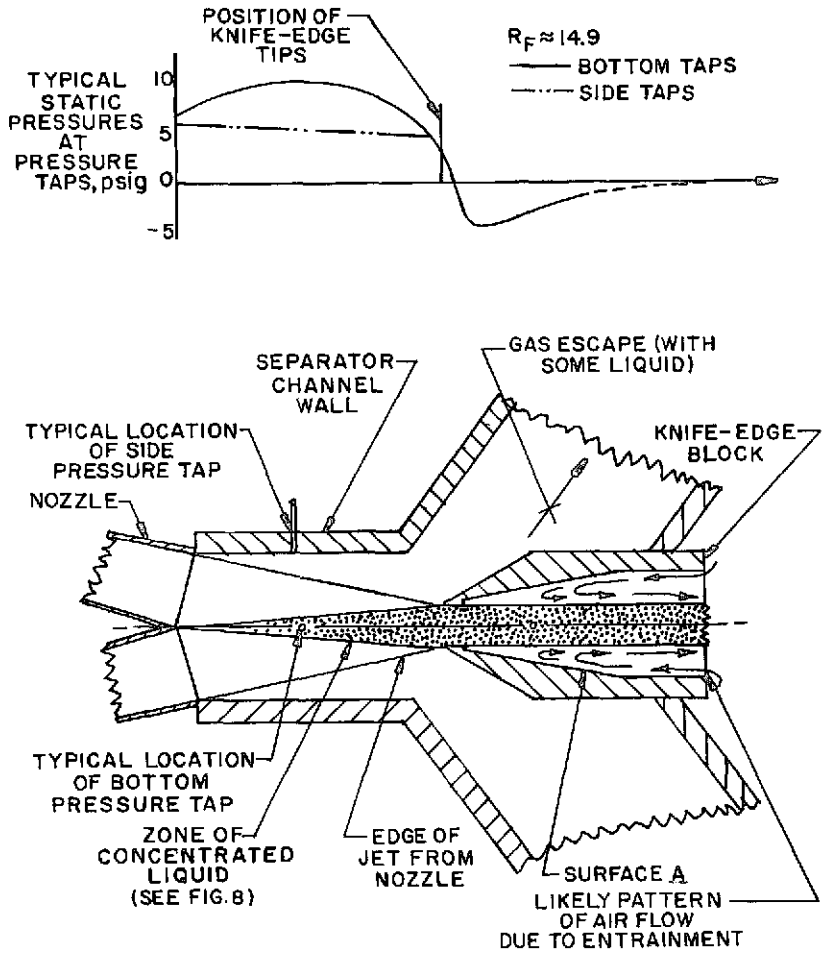

NOTE: THE FORM OF THE JETS FROM THE NOZZLE AND THE ZONE OF CONCENTRATED LIQUID HAVE BEEN IDEALIZED IN THIS SKETCH (SEE DISCUSSION IN SECTIONS II.C.1 AND II.C.3.)

Fig. 24. Simplified typical knife-edge separator geometry and pressure profiles

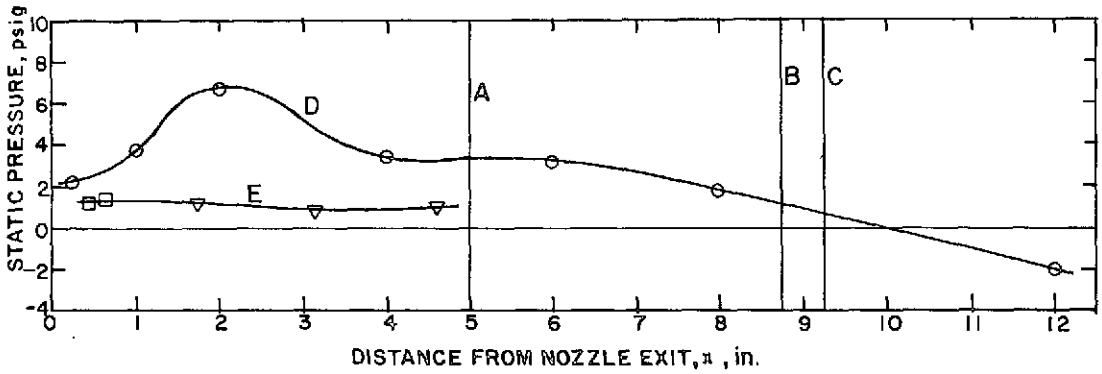

○ – DATA TAKEN ON CHANNEL ℄

□ – DATA TAKEN ON BOTTOM SURFACE OF CHANNEL BETWEEN ℄ AND SIDE WALL

▽ – DATA TAKEN ON CHANNEL SIDE WALL

A – LOCATION AT WHICH SEPARATOR CHANNEL WALL ANGLES OUTWARDS FOR GAS ESCAPE (SEE FIG. 24)

B – LOCATION OF KNIFE-EDGE TIPS

C – LOCATION AT WHICH INSIDE SURFACE OF KNIFE-EDGE TIPS STEPS BACK .062 in. (SEE FIG. 24)

$\theta = 15°$ $x = 8.75$ in.
$G = .75$ in. $R_F = 86$

Fig. 25. Typical static pressure profile data from separator channel (data continues past knife-edge tips)

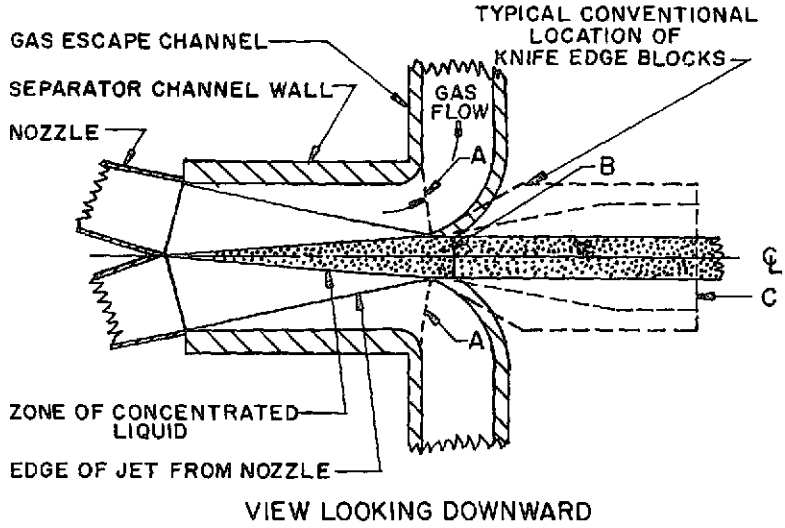

Fig. 26. Proposed separator design to avoid the presence of flow in an adverse pressure gradient between the knife-edge blocks (see text). Note: the idealized flow patterns sketched in Fig. 24 are also used here

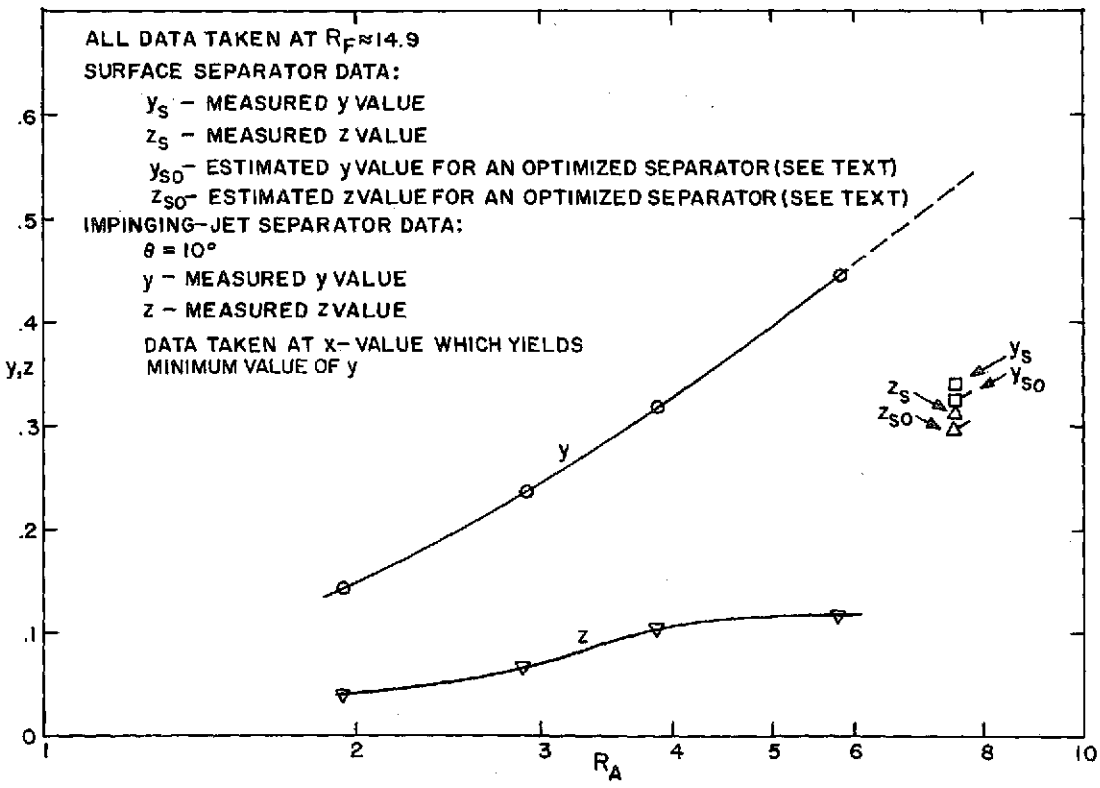

Fig. 27. Comparison of y- and z- values for surface separator and knife-edge impinging-jet separator, $R_F = 14.9$

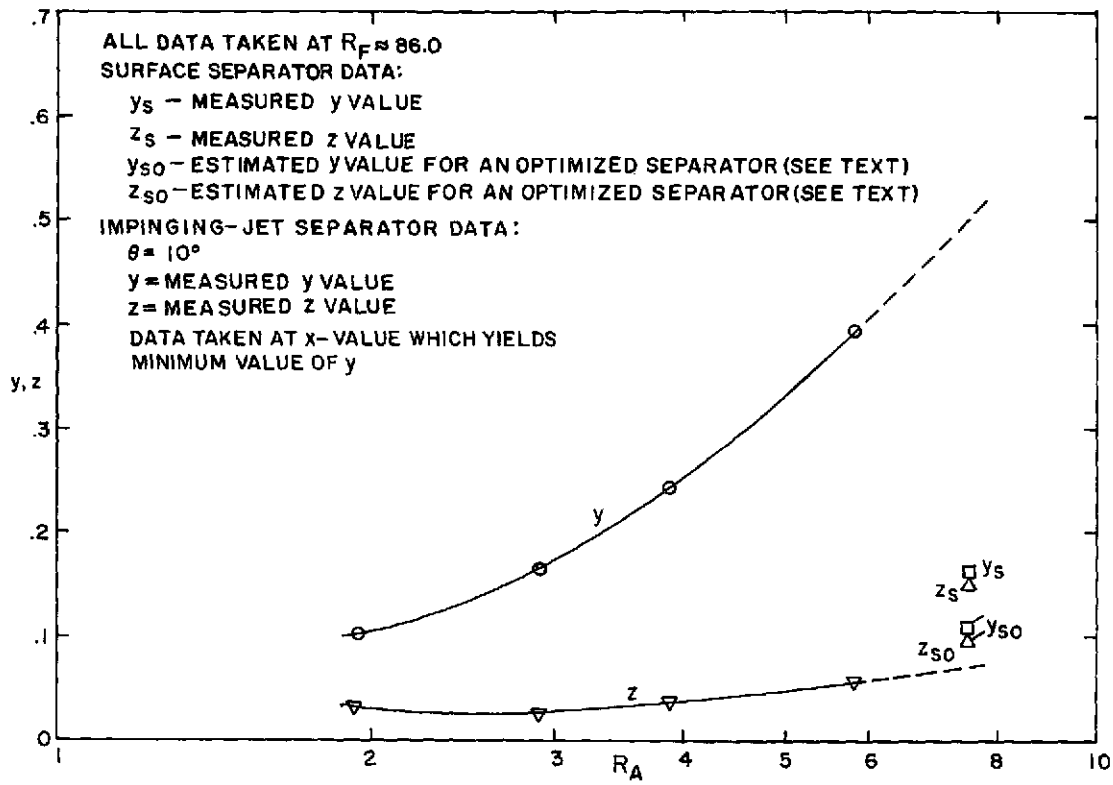

Fig. 28. Comparison of y- and z- values for surface separator and knife-edge impinging-jet separator, $R_F = 86.0$

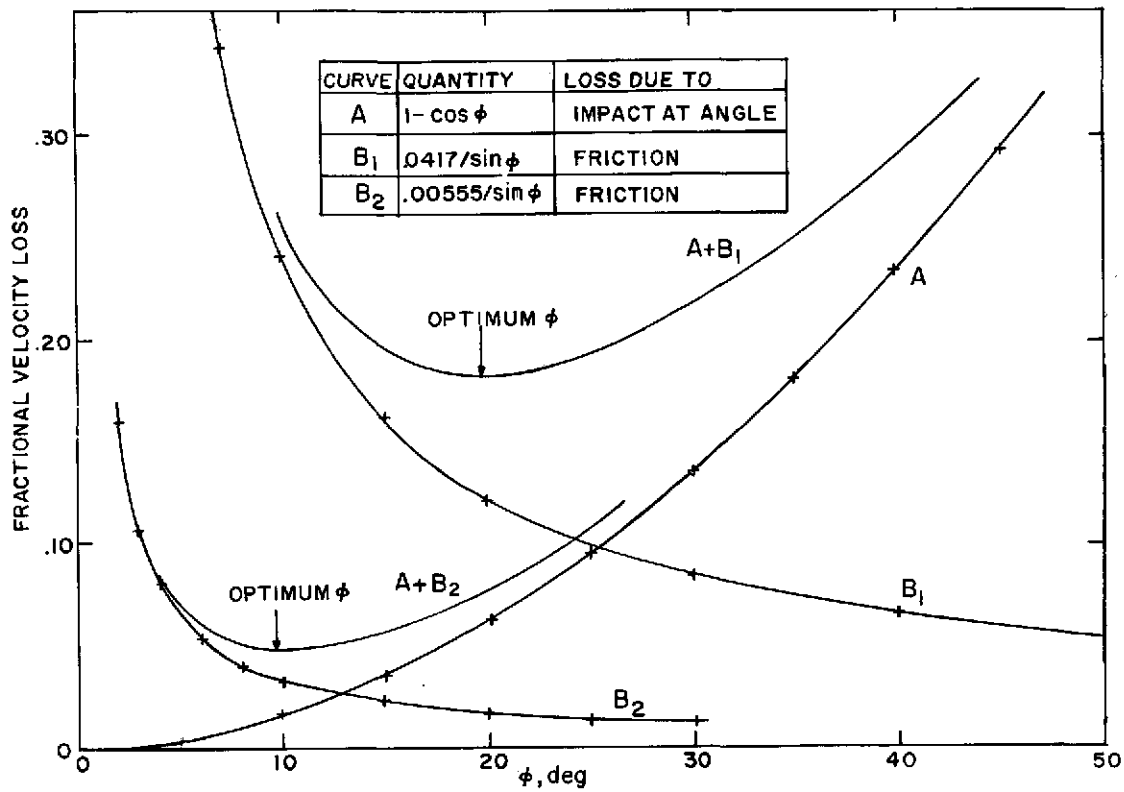

Fig. 29. Curves illustrating simplified optimization procedure for flat surface separator (see text)

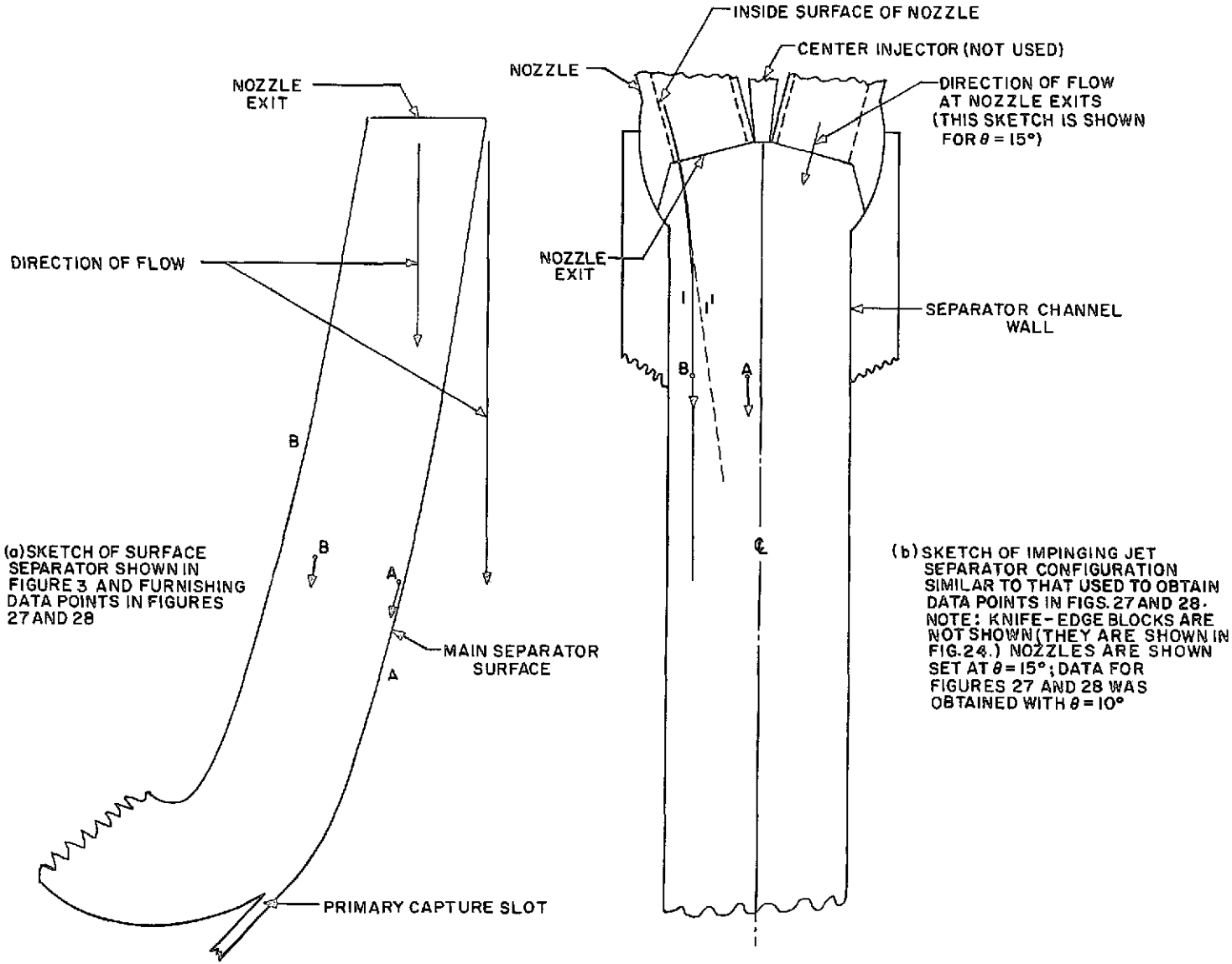

Fig. 30. Sketches illustrating the importance of centrifugal forces in partially explaining the large differences in R_B observed between the (curved) surface separator and the impinging-jet separator

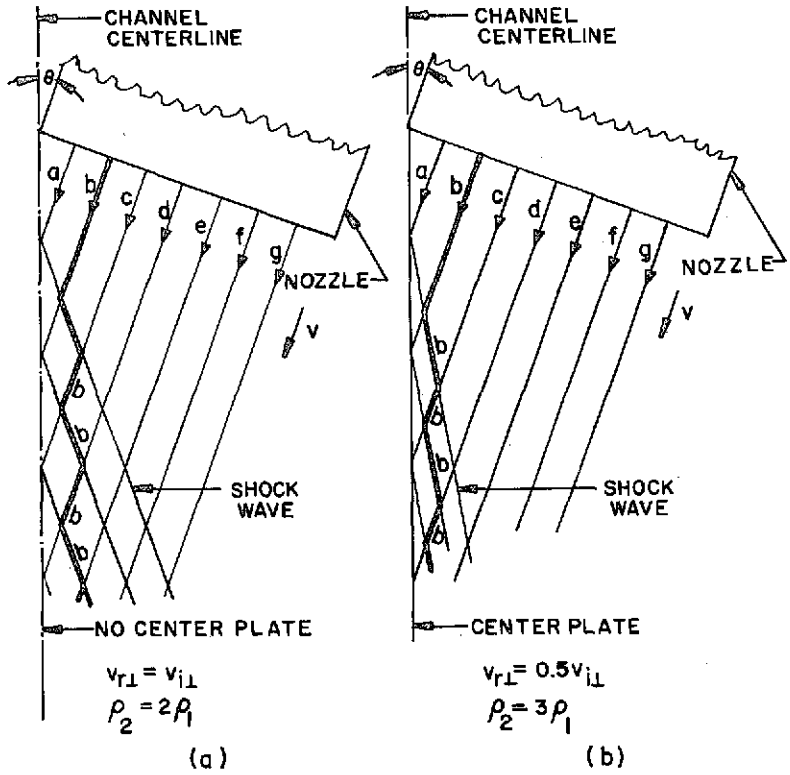

Fig. 31. Sketch used in discussion of a simplified theory explaining the better concentration of liquid flow obtained through the use of a solid center plate

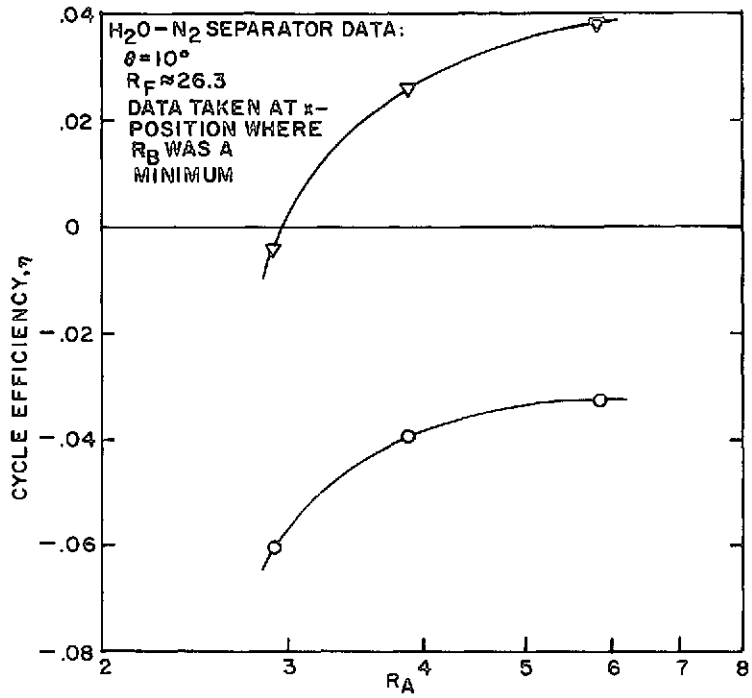

O-CALCULATIONS ASSUMING FLOW BYPASSING PRIMARY CAPTURE SLOT IS RETURNED (WITH TOTAL LOSS OF KINETIC ENERGY) TO UPSTREAM DIFFUSER INLET

▽ CALCULATIONS ASSUMING FLOW BYPASSING PRIMARY CAPTURE SLOT CAN, BY SEPARATION AND DIFFUSION, BE RAISED TO A PRESSURE SUFFICIENT TO BE INJECTED AT THE NOZZLE INLET

Fig. 32. Estimated efficiencies of impinging-jet separator Li-Cs cycles (see text)

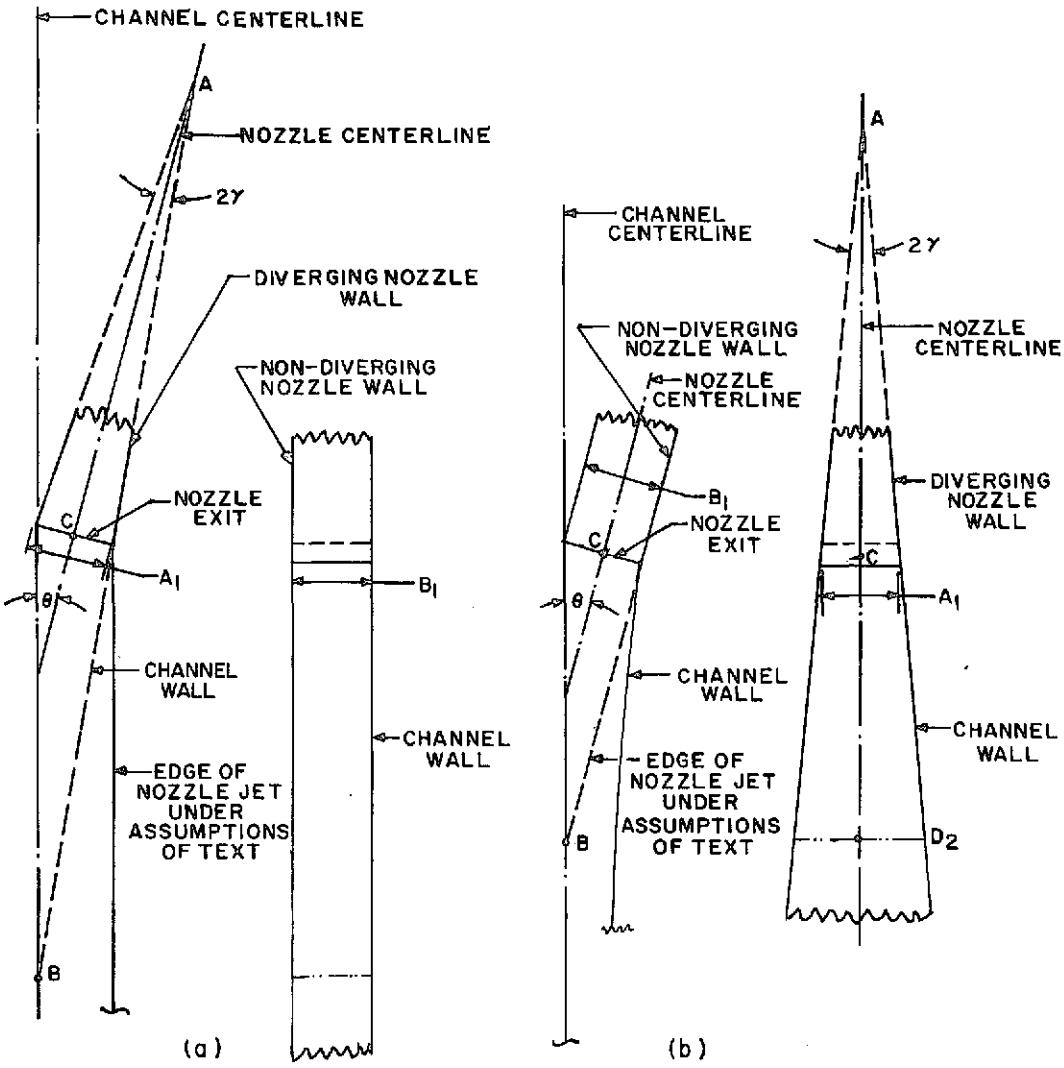

Fig. 33. Sketch used in the discussion of the effect of nozzle divergence on impinging-jet separator performance (see text)

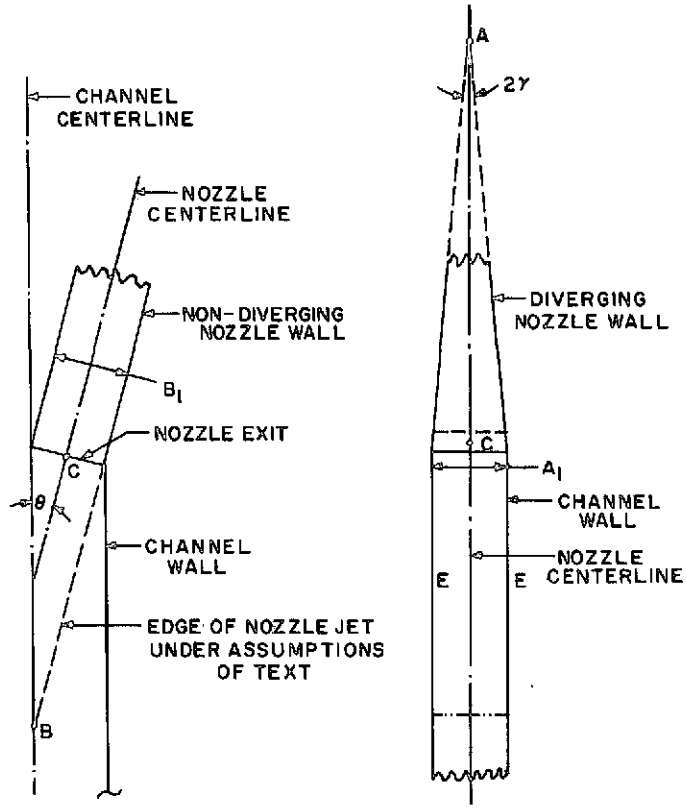

Fig. 34. A configuration which was tested and yielded some evidence possibly indicating a reduction in nozzle divergence losses (compare with Fig. 33; also see text)

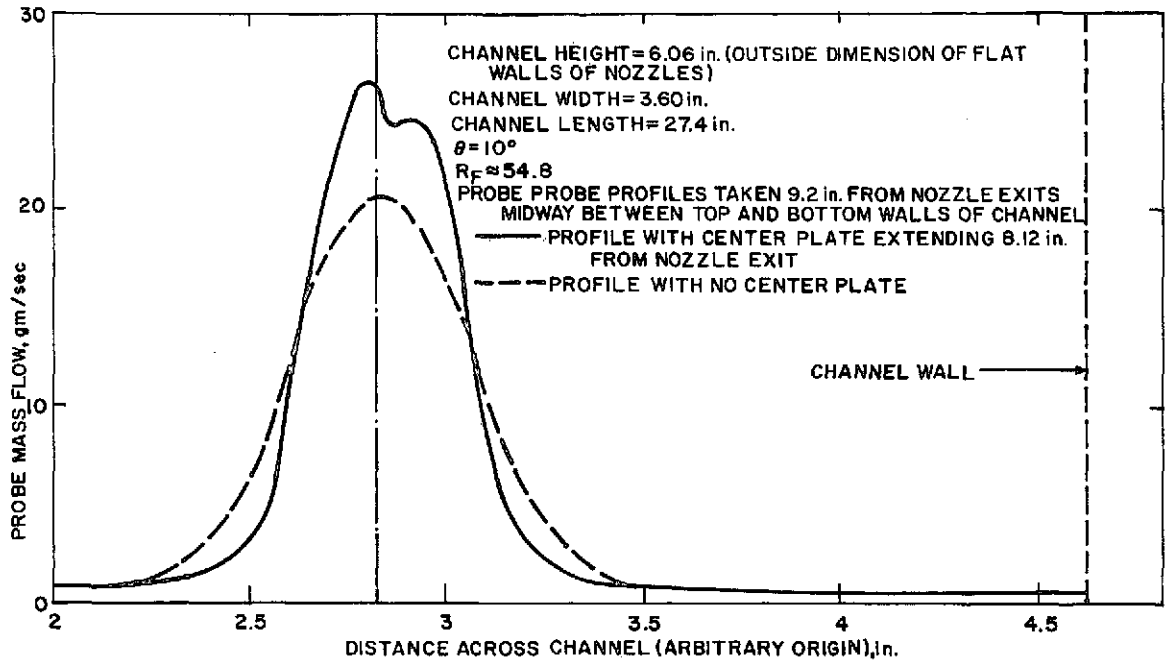

Fig. 35. Mass flow probe profiles taken across channel with and without a centerplate

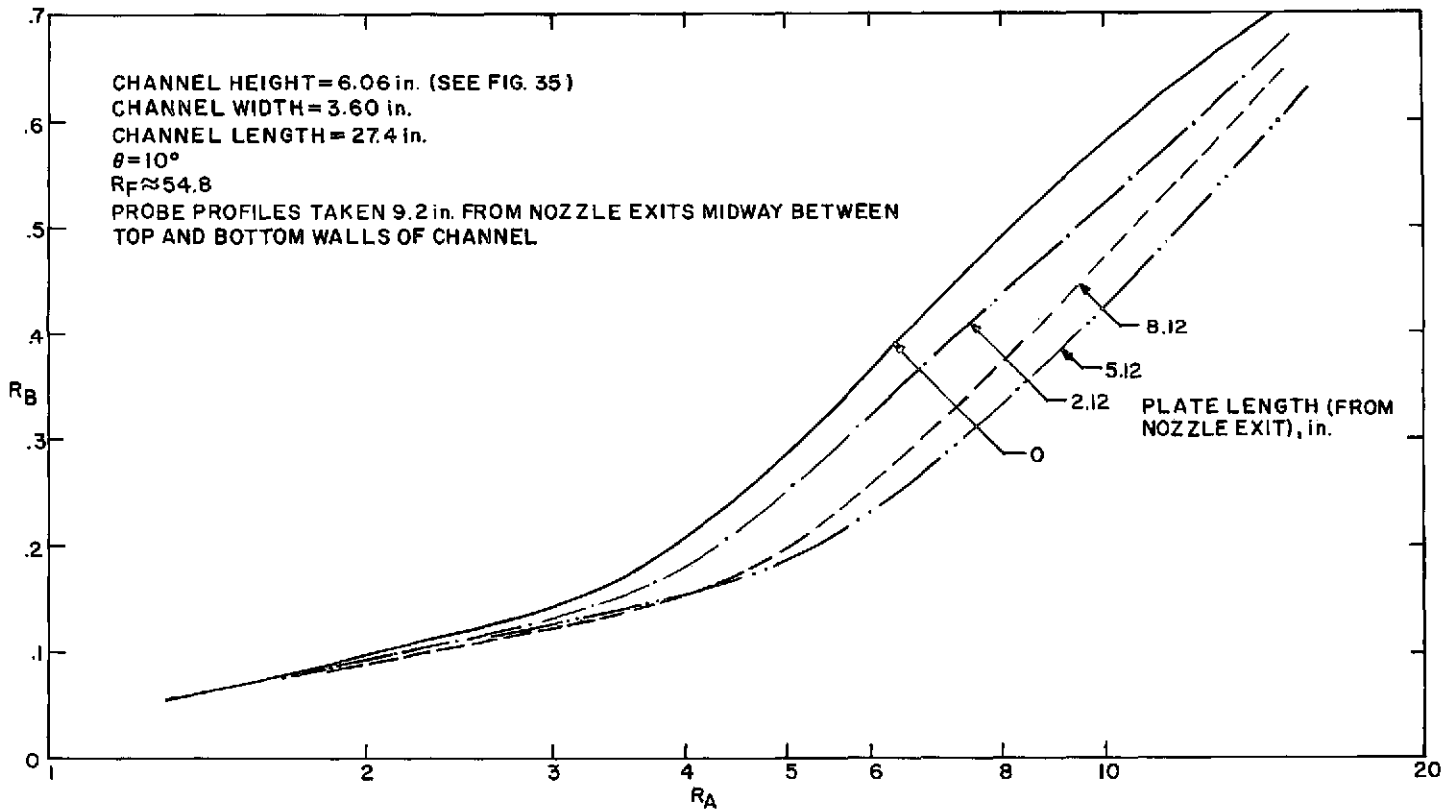

Fig. 36. R_B vs R_A calculated from probe profiles across channel with centerplates of varying length

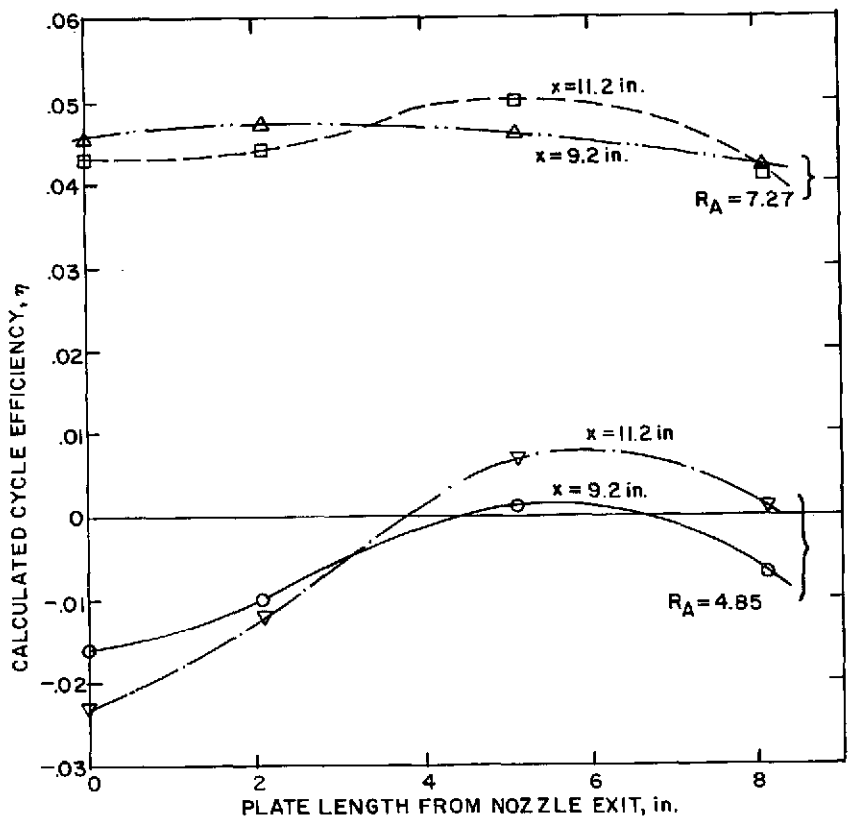

CHANNEL HEIGHT= 6.06 in. (SEE FIG.35)
CHANNEL WIDTH= 3.60 in.
CHANNEL LENGTH= 27.4 in.
θ=10°
R_F=54.8
PROBE PROFILES USED IN CALCULATING THESE VALUES OF η TAKEN MIDWAY BETWEEN TOP AND BOTTOM WALLS OF CHANNEL
HIGHER CURVES ASSUME BYPASS FLOW CAN BE RETURNED TO NOZZLE INLET WITHOUT PUMPING (SEE TEXT AND SECTION II. H)
LOWER CURVES ASSUME BYPASS FLOW MUST BE RETURNED, WITH A TOTAL LOSS OF KINETIC ENERGY, TO THE MAIN JET (SEE TEXT AND SECTION II. H)

Fig. 37. Li-Cs cycle efficiencies calculated by the method of Sec. II. H, inserting z, R_A and R_B values from channel separator tests

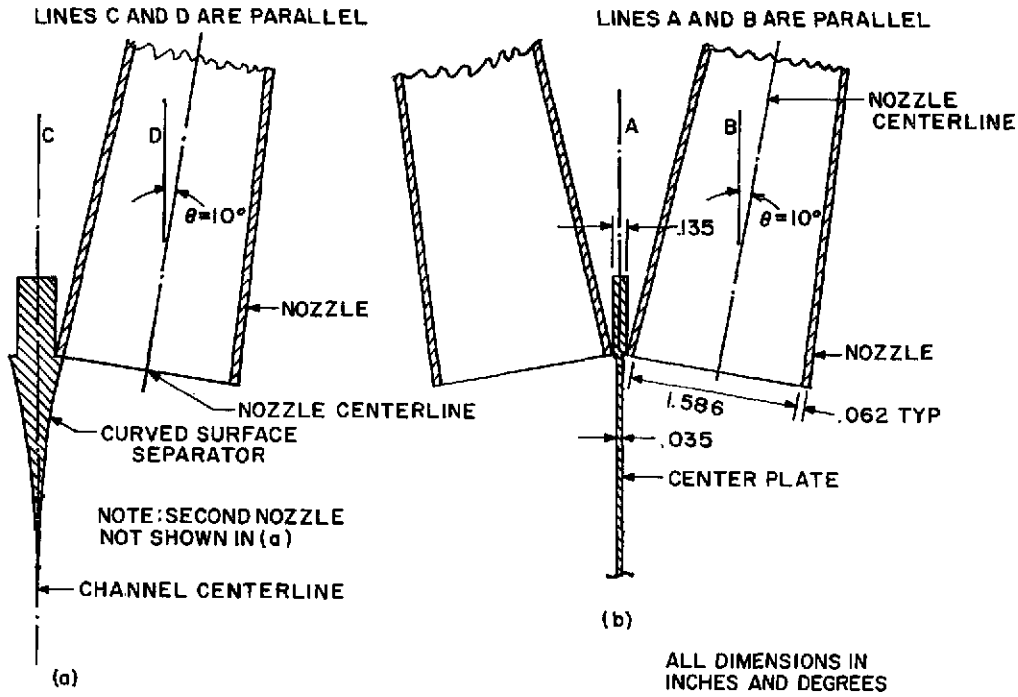

Fig. 38. Comparison of separator configuration (b) giving results discussed in Sec. IV. A, and possible improvement of this type of design (a)

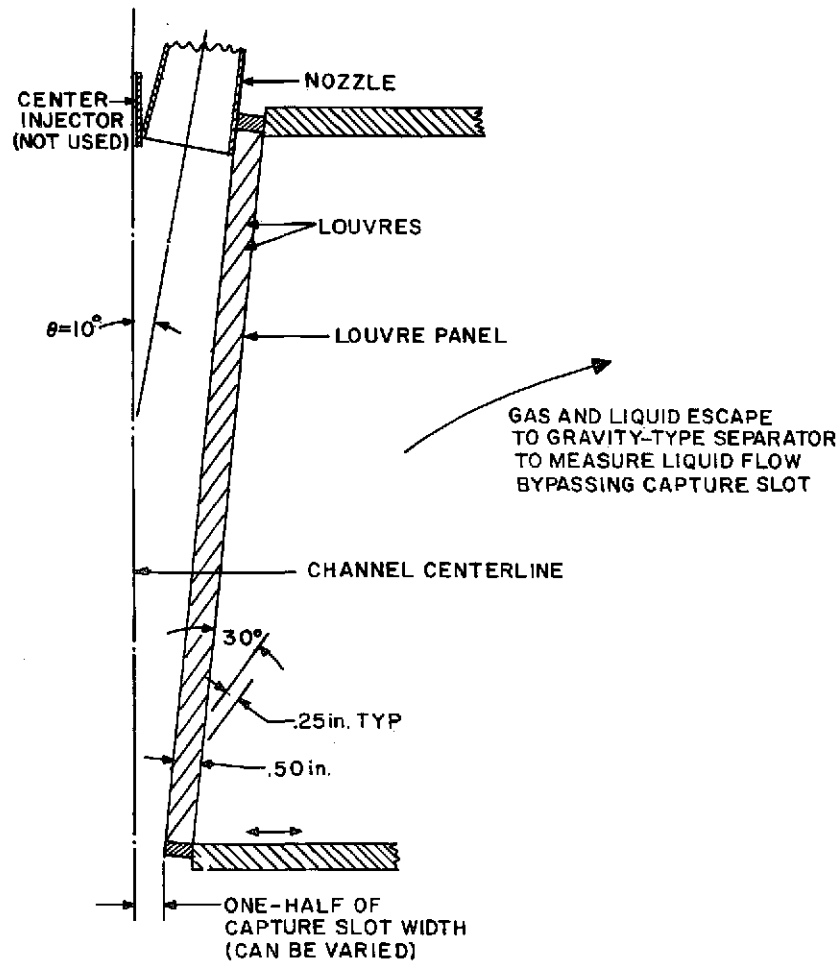

Fig. 39. Rough sketch of louvre separator geometry

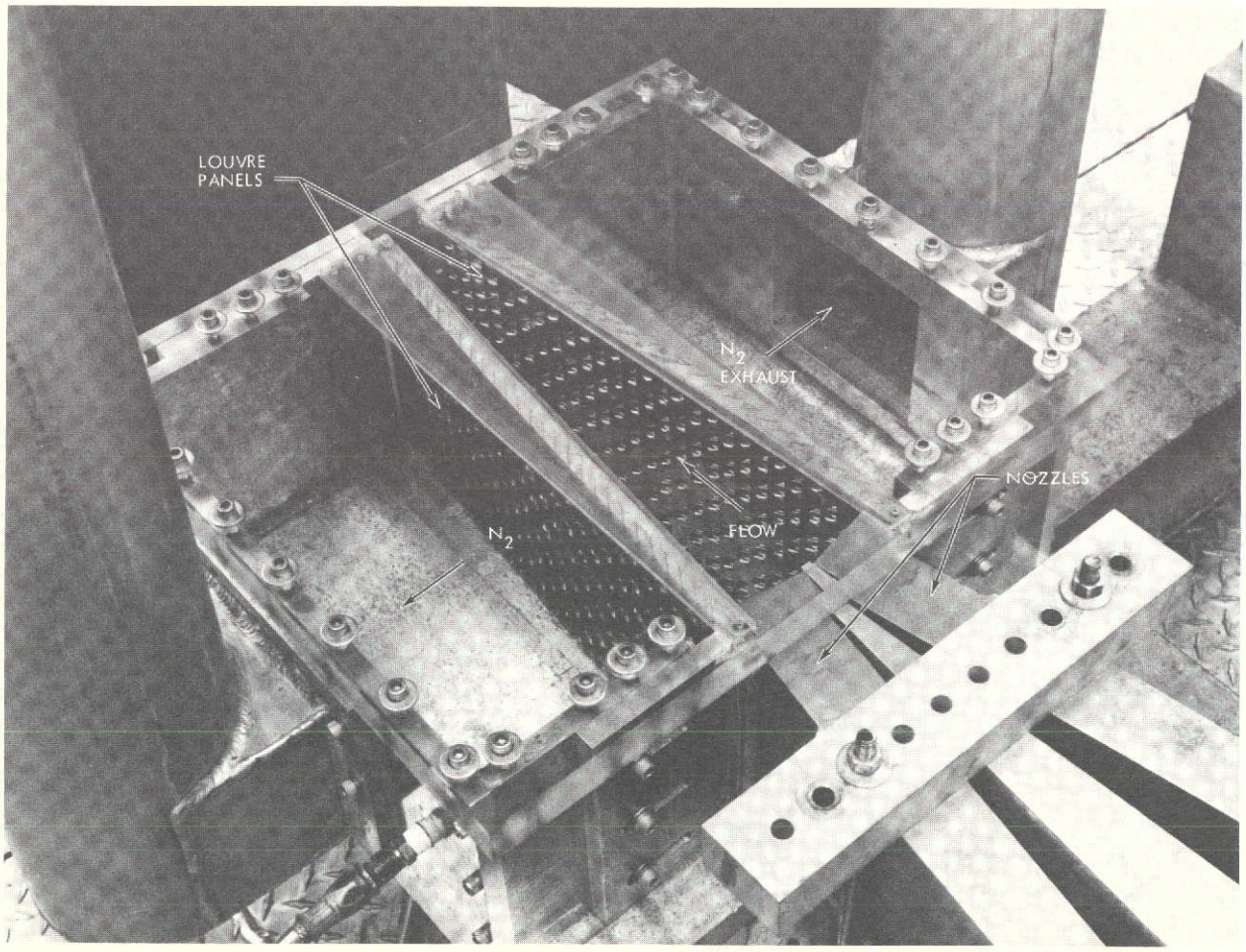

Fig. 40. Louvre separator installation

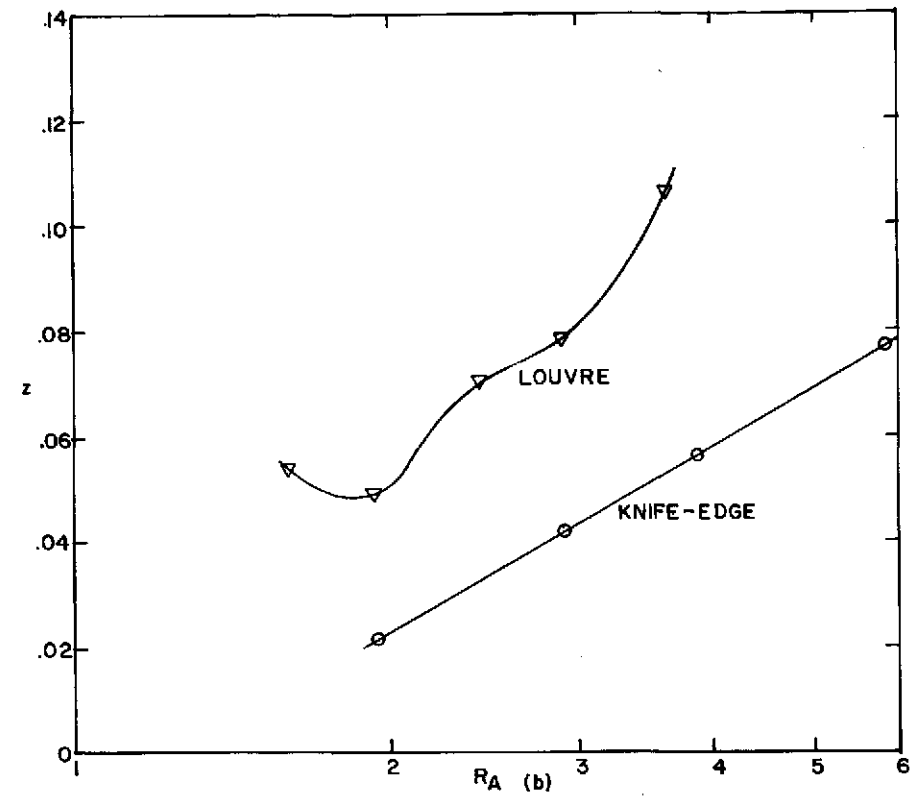

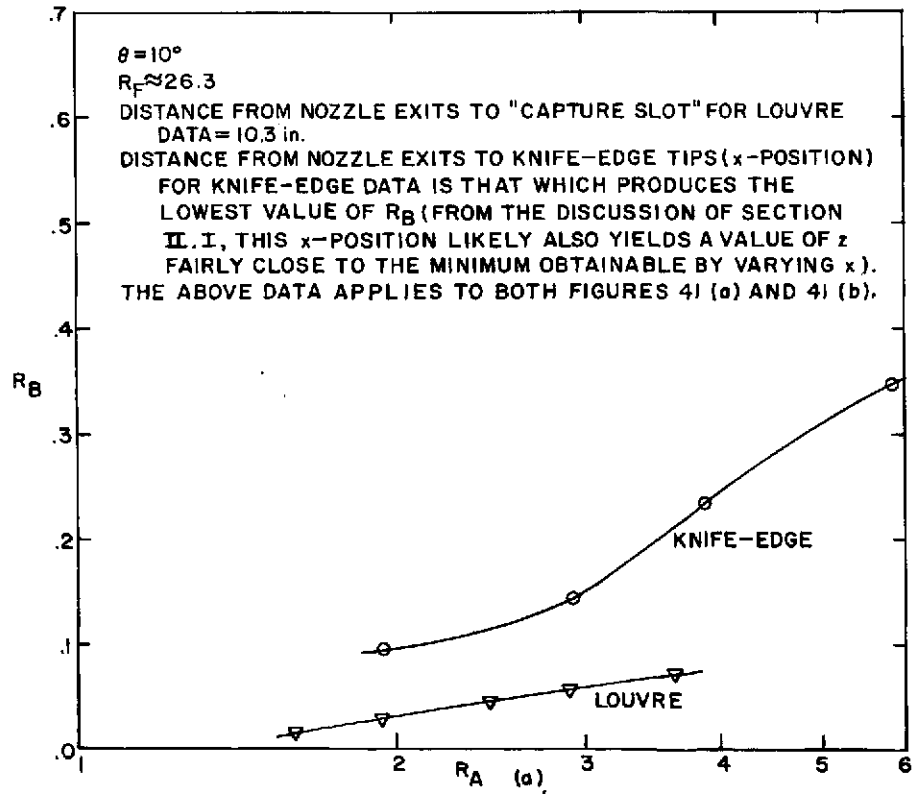

Fig. 41. Comparison of louvre and knife-edge R_B and z values as a function of R_A for $\theta = 10$ deg, $R_F \simeq 26.3$

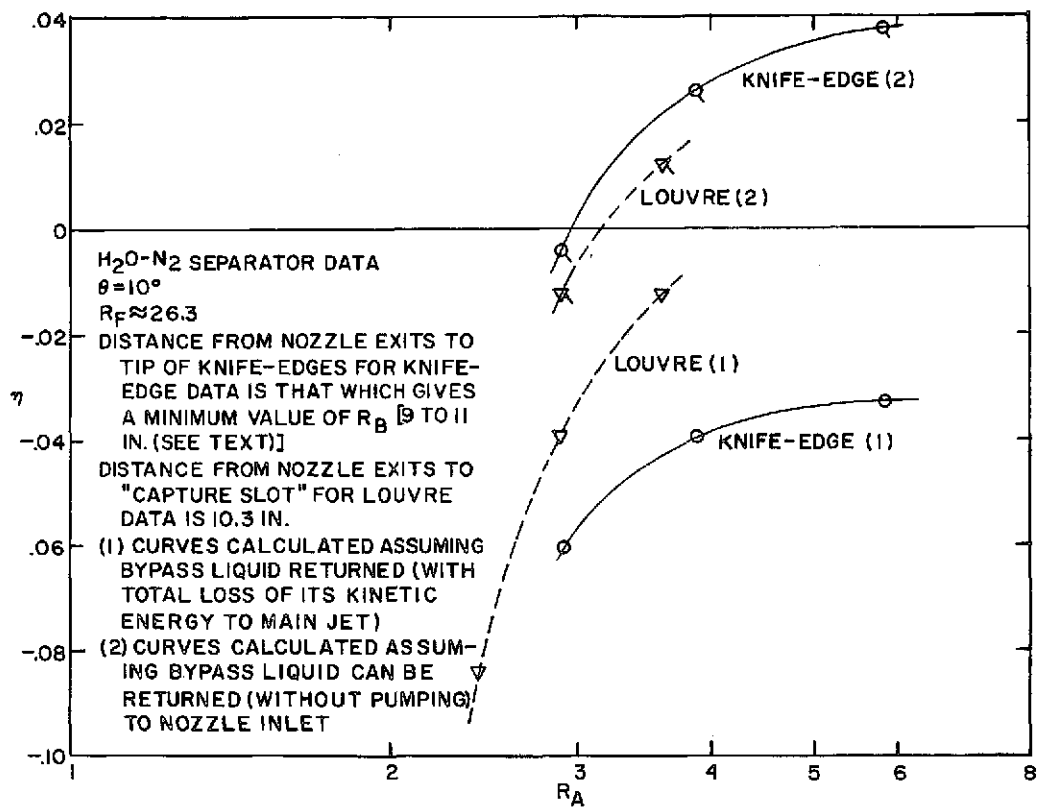

Fig. 42. Comparison of Cs-Li cycle efficiencies calculated by the methods of Sec. II. H using R_A, R_B and z data from the knife-edge and louvre separators discussed in this section

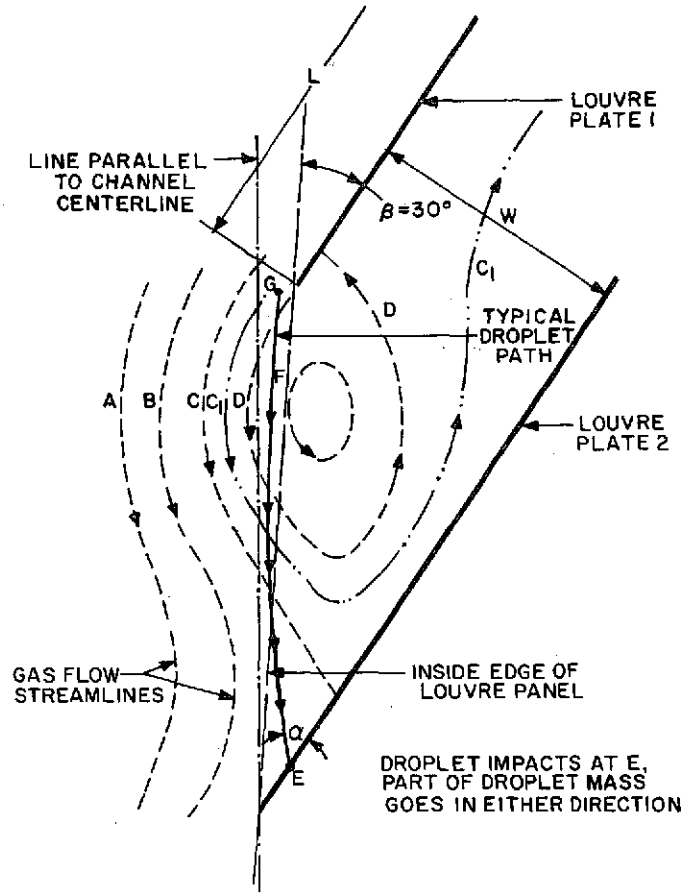

Fig. 43. Assumed flow pattern near inside edge of louvre panel

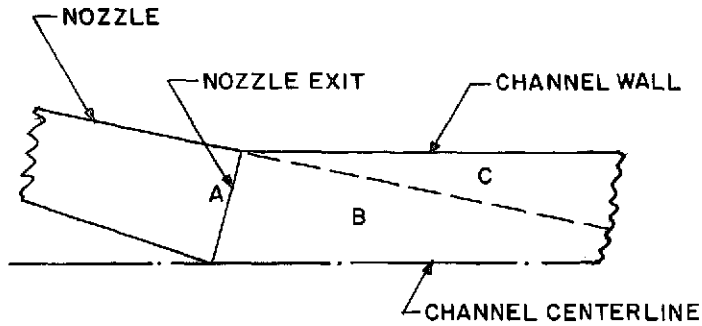

Fig. 44. Sketch used in the discussion of effects which might occur if the channel area was the same as the nozzle exit area

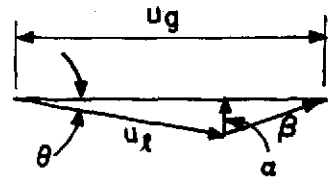

Fig. 45. Sketch used in the discussion of a possible cause for poor separator performance when the channel area equals the nozzle exit area

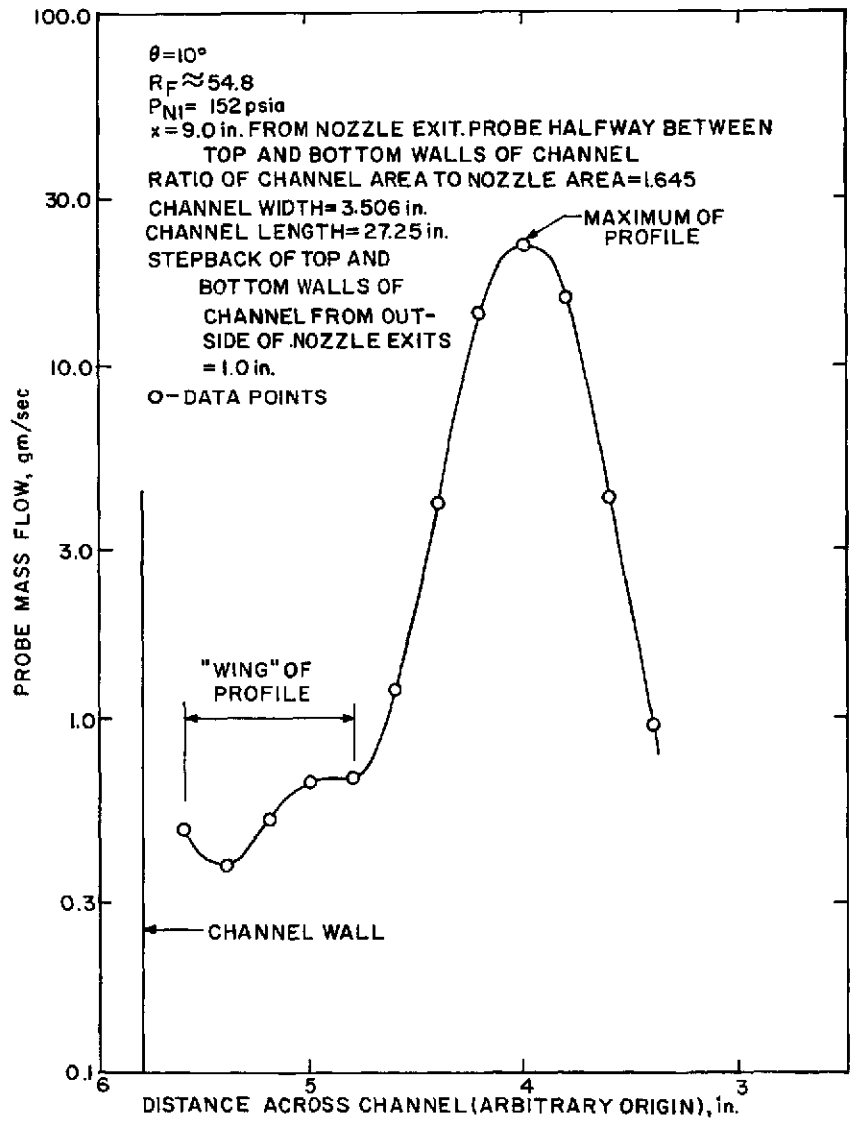

Fig. 46. Typical mass flow probe profile for channel tests

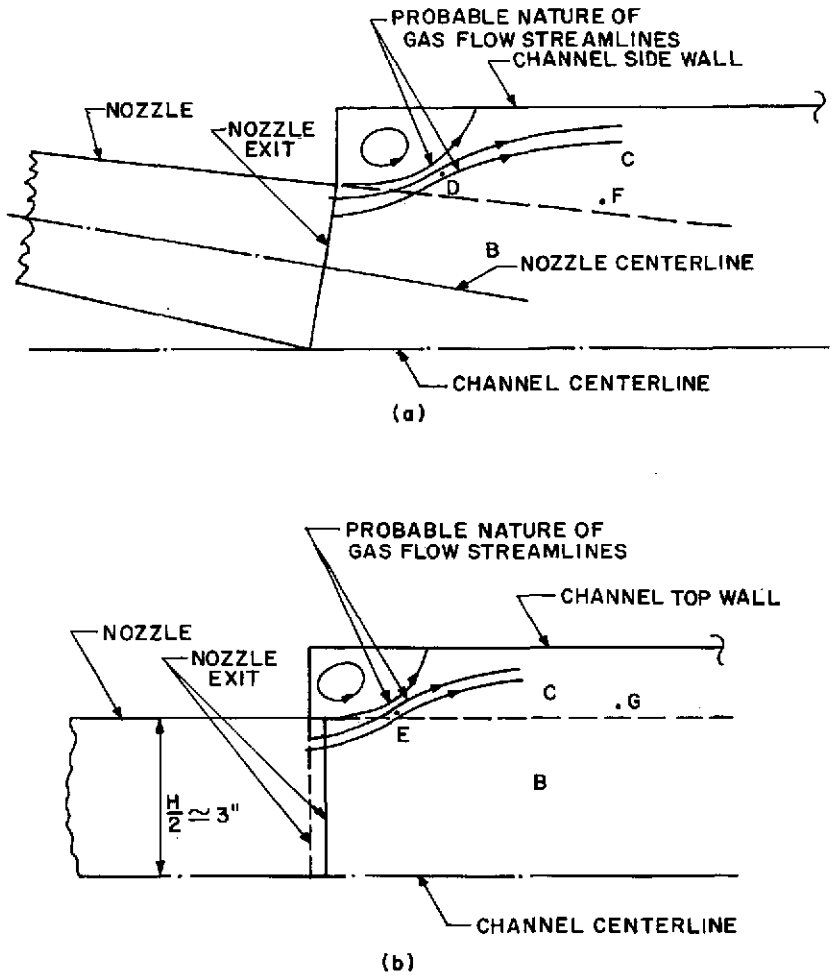

Fig. 47. Sketches used in the discussion of the effects on separator performance of stepping back the side or top and bottom walls of the channel

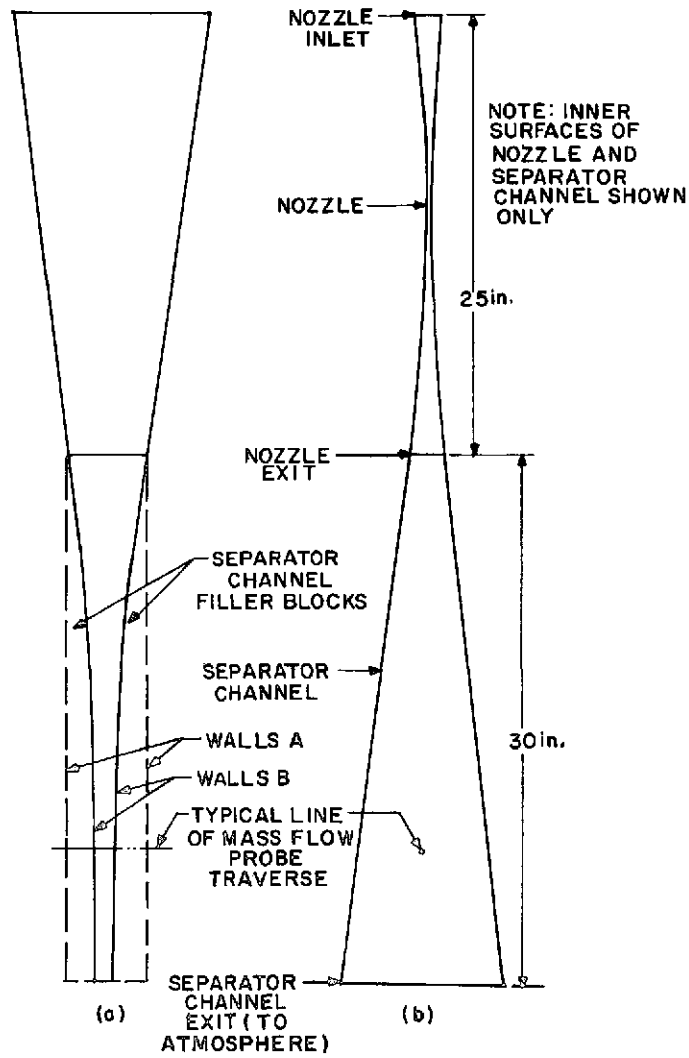

Fig. 48. Sketch of converging nozzle

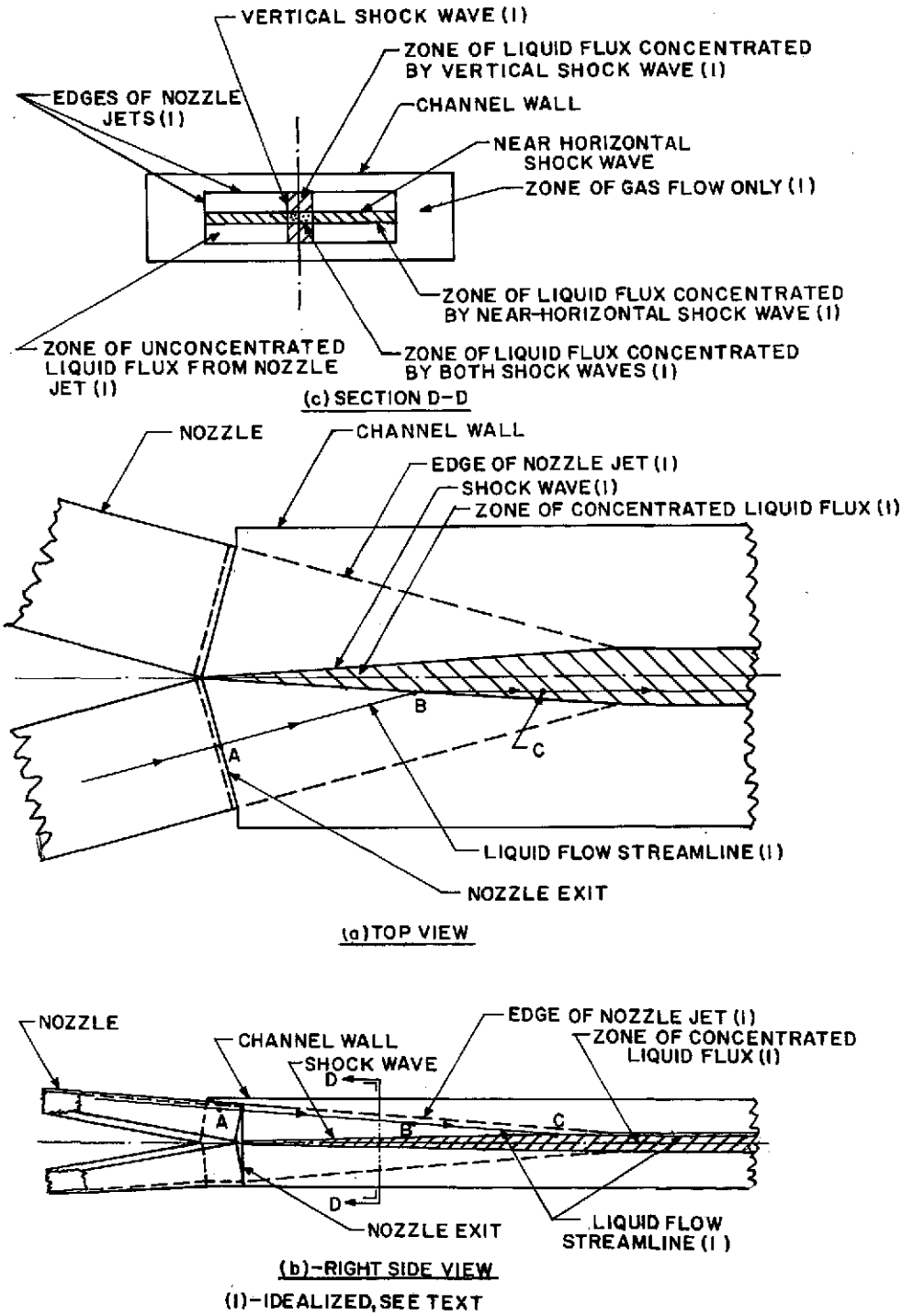

Fig. 49. Idealized flow pattern for four nozzle impinging-jet separator

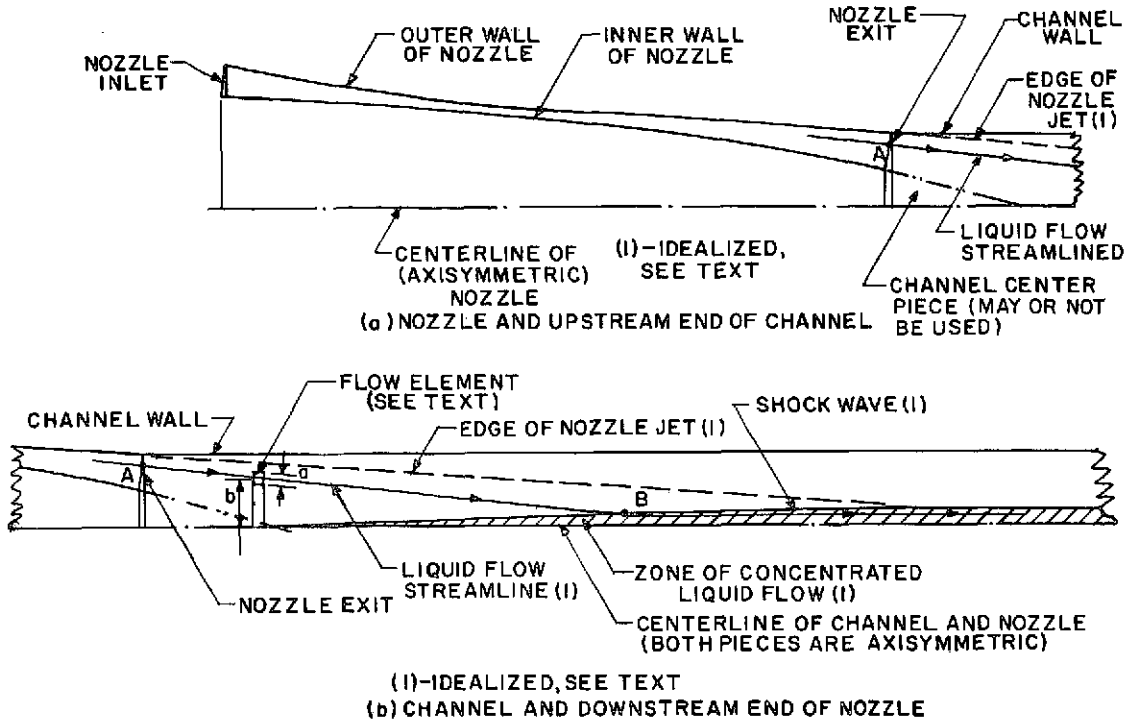

Fig. 50. Idealized flow pattern for annular nozzle and attached separator channel

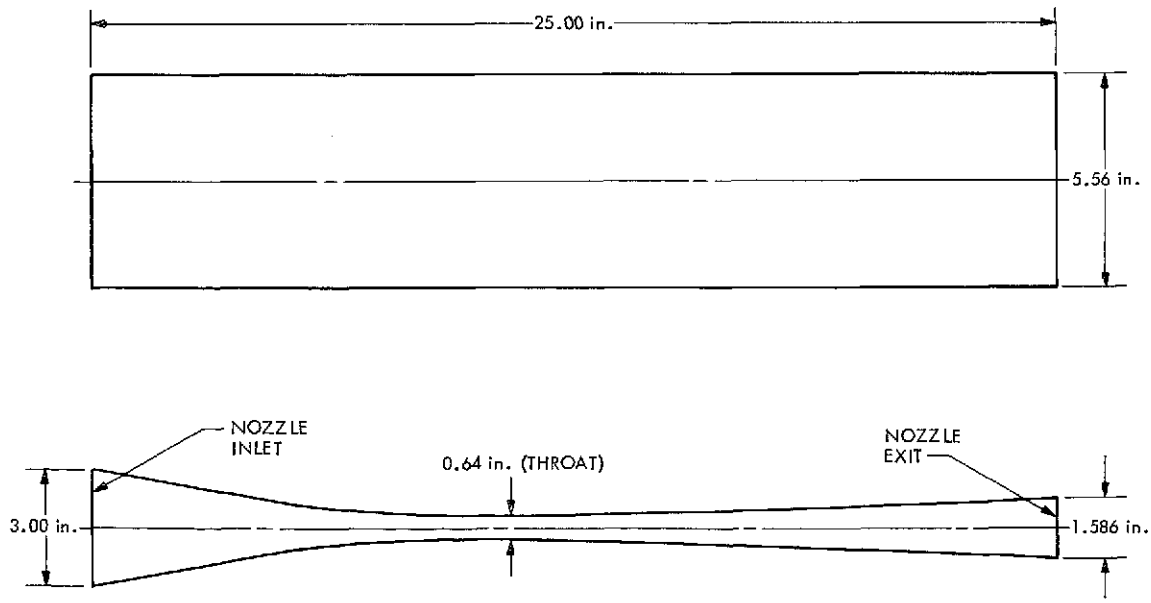

Fig. 51. Rough sketch of the internal surfaces of the standard nozzles used for most of the experiments discussed

NASA — JPL — Coml., L.A., Calif.